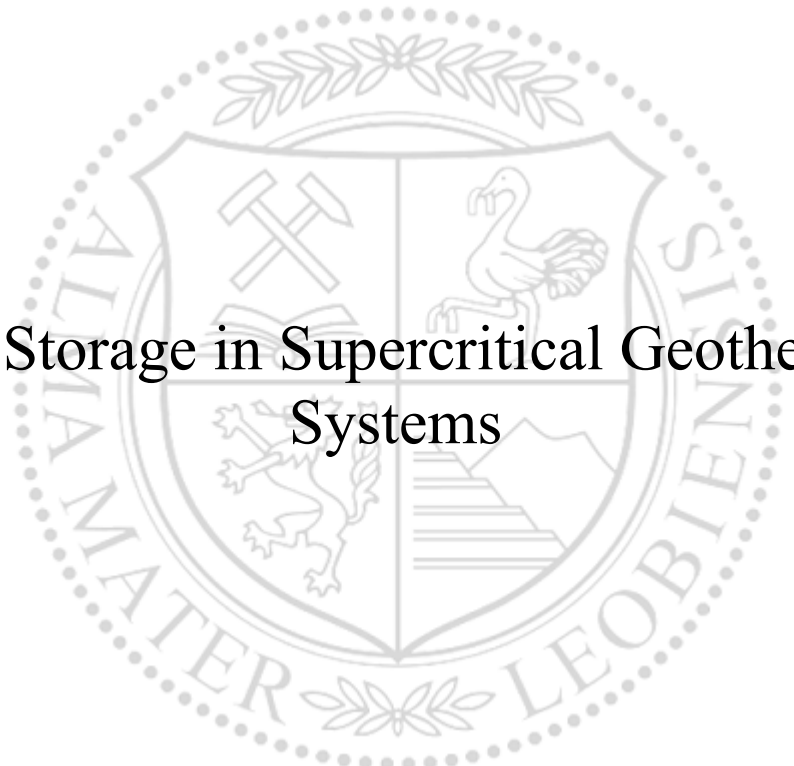




Chair of Geenergy Production Engineering

Master's Thesis



CO₂ Storage in Supercritical Geothermal
Systems

Jan Übelleitner, BSc

November 2024



MONTANUNIVERSITÄT LEOBEN

www.unileoben.ac.at

EIDESSTATTLICHE ERKLÄRUNG

Ich erkläre an Eides statt, dass ich diese Arbeit selbstständig verfasst, andere als die angegebenen Quellen und Hilfsmittel nicht benutzt, den Einsatz von generativen Methoden und Modellen der künstlichen Intelligenz vollständig und wahrheitsgetreu ausgewiesen habe, und mich auch sonst keiner unerlaubten Hilfsmittel bedient habe.

Ich erkläre, dass ich den Satzungsteil „Gute wissenschaftliche Praxis“ der Montanuniversität Leoben gelesen, verstanden und befolgt habe.

Weiters erkläre ich, dass die elektronische und gedruckte Version der eingereichten wissenschaftlichen Abschlussarbeit formal und inhaltlich identisch sind.

Datum 07.11.2024

Unterschrift Verfasser/in
Jan Übelleitner

Jan Übelleitner, BSc.
Master Thesis 2024
Industrial Management and Business
Administration

CO₂ Storage in Supercritical Geothermal Systems

Supervisor: Univ.-Prof. Keita Yoshioka, PhD
Co-supervisor: Rotman A. Criollo Manjarrez, PhD

Chair of Geoenery Production Engineering

Acknowledgments

I would like to express my sincerest gratitude to my supervisor, Univ.-Prof. Keita Yoshioka, PhD for giving me the opportunity to undertake this Master's thesis. His guidance and expertise have been of great benefit to me in expanding my understanding of simulations and geothermal energy.

I would also like to express my gratitude to Rotman Criollo Manjarrez, PhD for his mentorship during this thesis. His willingness to share his extensive knowledge during our meetings and his insightful contributions have greatly enriched this work.

Lastly, I want to thank my family for always supporting me.

Abstract

The increasing concentration of atmospheric carbon dioxide (CO₂) poses a significant threat to global climate stability, necessitating innovative solutions for effective long-term carbon sequestration. CO₂ storage in supercritical geothermal reservoirs is a promising solution for this problem, utilizing the unique density properties of CO₂ and water under supercritical conditions. Above the critical temperature and pressure of water, supercritical CO₂ has a higher density, largely mitigating concerns about leakage. This is of particular interest in volcanically active areas, where geothermal potential and carbon sequestration may be used in tandem to generate renewable energy while simultaneously reducing atmospheric CO₂ levels. Previous studies have demonstrated the potential for CO₂ to sink in these supercritical environments at constant temperatures. However, the effects of temperature gradients on CO₂ migration patterns have not been thoroughly analyzed. This leaves a gap in the research, as reservoirs encountered in real life do not exhibit a constant temperature throughout. To address this gap, this work investigates CO₂ injection behavior through a series of 2D simulations of varying permeability and a realistic temperature distribution. The temperature distribution is created by placing a heat source, representing a magmatic intrusion, in a part of the reservoir. By calculating gravity numbers and plotting saturation profiles, the study evaluates the balance between viscous and buoyant forces governing CO₂ plume patterns, revealing distinct migration behaviors, especially at high permeabilities. These in particular showed promising results in the previous studies. The results include unexpected CO₂ movement patterns due to convection and provide insights into bulk fluid flows and viscosity profiles over time. These results highlight the importance of detailed reservoir evaluation to ensure safe and effective CO₂ storage, and contribute valuable knowledge to the field of carbon sequestration in geothermal reservoirs.

Zusammenfassung

Die steigende Konzentration von Kohlendioxid (CO_2) in der Atmosphäre stellt eine ernsthafte Bedrohung für die Stabilität des Weltklimas dar und erfordert innovative Lösungen für eine effektive, langfristige Bindung von Kohlendioxid. Die Speicherung von CO_2 in überkritischen geothermischen Lagerstätten ist eine vielversprechende Lösung für dieses Problem, da sie die einzigartigen Dichteigenschaften von CO_2 und Wasser bei überkritischen Bedingungen nutzt. Oberhalb der kritischen Temperatur und des kritischen Drucks von Wasser weist überkritisches CO_2 eine höhere Dichte auf, wodurch die Bedenken hinsichtlich möglicher Leckagen weitgehend ausgeräumt werden. Dies ist besonders in vulkanisch aktiven Gebieten von Interesse, wo das geothermische Potenzial und die Kohlenstoffbindung gemeinsam genutzt werden können, um erneuerbare Energie zu erzeugen und gleichzeitig die CO_2 -Konzentration in der Atmosphäre zu senken. Frühere Studien haben gezeigt, dass CO_2 in diesen überkritischen Umgebungen bei konstanten Temperaturen absinkt. Die Auswirkungen von Temperaturverteilungen auf die CO_2 -Ausbreitungsweise sind jedoch noch nicht ausreichend erforscht. Dies stellt eine Forschungslücke dar, da Lagerstätten in der Realität keine konstanten Temperaturen aufweisen. Um diese Lücke zu schließen, wird in dieser Arbeit das CO_2 -Injektionsverhalten durch eine Reihe von 2D-Simulationen mit variierender Permeabilität und einer realistischen Temperaturverteilung untersucht. Die Temperaturverteilung wird erzielt, indem eine Wärmequelle, die einen magmatischen Einschluss darstellt, in einem Teil der Lagerstätte simuliert wird. Durch die Berechnung von „Gravity Numbers“ und die Darstellung von CO_2 -Sättigungsprofilen untersucht diese Arbeit das Verhalten zwischen viskosen und auftriebsbedingten Kräften, welche die CO_2 -Wolke beeinflussen, und zeigt ein distinktes Ausbreitungsverhalten, insbesondere bei hohen Permeabilitäten. Besonders diese haben in den früheren Studien vielversprechende Ergebnisse gezeigt. Die Ergebnisse beinhalten unerwartete, durch Konvektion verursachte CO_2 -Ausbreitungsmuster und geben einen Einblick in die Massenbewegungen und Viskositätsprofile über die Injektionsdauer. Die Resultate zeigen, wie wichtig eine detaillierte Bewertung der Lagerstätten ist, um eine sichere und effektive CO_2 -Speicherung zu gewährleisten, und liefern wertvolle Erkenntnisse auf dem Gebiet der CO_2 -Speicherung in geothermischen Lagerstätten.

Table of Contents

Acknowledgments.....	vii
Abstract	viii
Zusammenfassung.....	ix
Table of Contents	11
Chapter 1.....	13
Introduction.....	13
Chapter 2.....	19
Methodology and Model.....	19
2.1 Kernel System and Calculation Parameters	21
2.1.1 PorousFlowMassTimeDerivative.....	21
2.1.2 PorousFlowAdvectiveFlux.....	22
2.1.3 PorousFlowEnergyTimeDerivative	22
2.1.4 Heat flow and associated Kernels	23
2.2 Fluid Properties.....	24
2.3 Injection and Production.....	24
2.4 Material Properties of the Reservoir	25
2.5 Solver and Preconditioning.....	26
2.6 Mesh and Model Parameters.....	27
2.7 Boundary Conditions	27
2.8 Scenarios	29
2.8.1 Temperature and Pressure Equilibration.....	29
2.8.2 CO ₂ Injection Cases	30
2.9 Gravity Number Calculation.....	31
Chapter 3.....	35
Results.....	35
3.1 Equilibration Results.....	36
3.2 CO ₂ Injection at constant temperature	38
3.3 CO ₂ Injection on the left side at 10 mD permeability	42
3.3.1 Injection 200 m above the bottom reservoir boundary	42
3.3.2 Injection 400 m above the bottom reservoir boundary	43
3.3.3 Injection 525 m above the bottom reservoir boundary	44
3.4 CO ₂ Injection on the left side at 5 mD permeability	46
3.4.1 Injection 200 m above the bottom reservoir boundary	46
3.4.2 Injection 400 m above the bottom reservoir boundary	47
3.4.3 Injection 525 m above the bottom reservoir boundary	48

3.5	CO ₂ Injection on the left side at 1 mD permeability	50
3.5.1	Injection 200 m above the bottom reservoir boundary	50
3.5.2	Injection 400 m above the bottom reservoir boundary	51
3.5.3	Injection 525 m above the bottom reservoir boundary	52
3.6	CO ₂ Injection on the right side at 10 mD permeability	54
3.6.1	Injection 200 m above the bottom reservoir boundary	54
3.6.2	Injection 400 m above the bottom reservoir boundary	56
3.6.3	Injection 525 m above the bottom reservoir boundary	57
3.7	CO ₂ Injection on the right side at 5 mD permeability	58
3.7.1	Injection 200 m above the bottom reservoir boundary	58
3.7.2	Injection 400 m above the bottom reservoir boundary	59
3.7.3	Injection 525 m above the bottom reservoir boundary	60
3.8	CO ₂ Injection on the right side at 1 mD permeability	62
3.8.1	Injection 200 m above the bottom reservoir boundary	62
3.8.2	Injection 400 m above the bottom reservoir boundary	63
3.8.3	Injection 525 m above the bottom reservoir boundary	64
3.9	Pressure Profiles at the Injection Point	66
3.9.1	Injection Depth of 200 m	66
3.9.2	Injection Depth of 525 m	67
Chapter 4	69
Discussion	69
4.1	CO ₂ Plume Behavior	69
4.2	Pressure Profiles at the Injection Points.....	80
Chapter 5	83
Conclusion	83
5.1	Summary	83
5.2	Future Work	84
References	87
Simulation Files	92
List of Figures	93
List of Tables	95
Abbreviations	96

Chapter 1

Introduction

Climate change and its associated effects are amongst the biggest challenges faced in the 21st century. Much of the scientific consensus is focused on greenhouse gases, particularly carbon dioxide (CO₂). The annual emissions of CO₂ were around 37 gigatons in 2022 (Statista Research Department, 2022), with this number projected to grow to about 43 gigatons by 2030. Power generation at 42% and transportation at 23% account for the largest percentages of global anthropogenic CO₂ emissions, followed by industrial processes (Parekh et al., 2023). The reduction of anthropogenic CO₂ is a major focus of the Paris Climate Agreement from 2015, with net zero emission targets set between 2045 and 2060 for different countries. The two main approaches of reducing emissions are the mitigation in the first place and the latter being carbon capture and storage and/or utilization (CCS / CCU / CCUS) for hard-to-abate sectors, such as cement and steel (Rubin et al., 2015). Carbon sequestration, or carbon capture and storage, projects focus on storing the CO₂ deep underground in geological formations. Although offering huge storage potentials, with a total active gas capacity of depleted gas reservoirs, depleted oil reservoir, aquifers and salt caverns amounting to roughly $3.9 \times 10^{11} \text{ m}^3$ (Al-Shafi et al., 2023), there are two main concerns with geological CO₂ storage, namely the leakage risk and induced seismic activity. Thus, the site selection, including continuous pressure monitoring, is extremely important to ensure the integrity of the underground storage (Parisio and Vilarrasa, 2020). At this point the idea of large-scale CO₂ storage in supercritical geothermal reservoirs springs to life. Above the critical temperature and pressure of the resident brine, CO₂ has a higher density than the brine and would thus migrate to the bottom of the reservoir, largely mitigating the concerns about leakage. At the same time, these high temperature conditions present excellent opportunities to utilize the geothermal potential. Systems with these favorable properties are most often magma driven and called high-enthalpy geothermal systems. Such systems can frequently be found in Iceland and California, amongst other volcanically active areas (Scott et al., 2017).

Traditional geothermal systems are classified either as deep or shallow systems, with shallow geothermal extending to depths of around 300 meters. For the scope of this thesis, a brief description of deep geothermal is sufficient. Three categories often encountered are thermal

spring systems, with temperatures up to 80°C, hydrothermal systems with up to 130°C and petrothermal systems between 130°C to 200°C (Zarrouk and McLean, 2019). Superhot geothermal resources reach enthalpies of up to 3000 kJ/kg and typically occur below a normal high-enthalpy system, closer to the heat, or magma, source (Yapparova et al., 2023).

Magmatic intrusions usually occur at depths ranging from 2 to 5 km and the reservoir fluids can reach temperatures of up to 550°C. At these temperatures, the pore fluid is in a supercritical, single-phase state. This supercritical fluid is indicated to provide excellent opportunities for electricity production, as was demonstrated by an exploratory well in the Krafla volcanic field in Iceland. This project from 2009 – 2012 by IDDP, Icelandic Deep Drilling Project, encountered a magmatic intrusion at 2,1 km depth and a supercritical pore fluid at 450°C. At these conditions, a single well is capable of producing up to 35 MW of electricity, whereas it is around 3 – 5 MW for typical high-enthalpy geothermal wells (Scott et al., 2015).

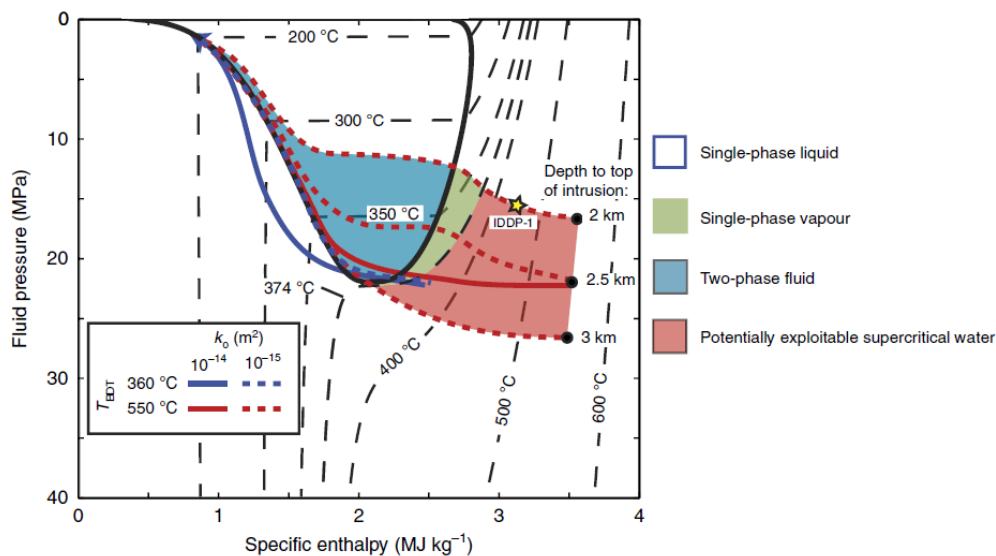


Figure 1 A Fluid pressure and specific enthalpy graph with isotherms showing the different fluid phase areas encountered during the drilling of IDDP-1, highlighting the two phase, single phase and supercritical regions, Scott et al., 2015

Figure 1 depicts the phase envelope for potentially exploitable geothermal water. Supercritical resources are characterized by two main parameters, the critical temperature and the critical pressure. If the pore fluid exceeds both parameters, it will be a supercritical phase, meaning it is neither fluid nor gas. The blue area denotes the conditions in which the water is present in its liquid and vapor phase, meaning a portion of the in-situ water has evaporated and the remaining part is in the liquid form due the pressure confinement. The green area is the single-phase vapor area, meaning all of the remaining liquid has evaporated. And the red area describes the region of interest for this paper, the supercritical stage.

One of the most important parameters influencing the formation of these superhot geothermal resources is the brittle-ductile transition in the rock surrounding the magma. It is the zone in which the rock stops deforming in a brittle manner when loaded and starts to deform in a plastic manner. The occurrence of this transition zone is primarily temperature and rock type dependent and can occur anywhere from around 360°C to 800°C for basaltic rocks. The plastic flow/deformation behavior drastically reduces the permeability, as all available pathways will be closed due to compression (Scott et al., 2015). During the formation of these superhot areas, one has to distinguish between the early stage and later stages of magmatic intrusion. In the early stages, there is a very high temperature gradient between the existing, brittle, rock and the newly developed intrusion. This results in a thin plastic layer separating the two bodies. Should there be an expulsion of magmatic fluids, either the magma body itself or the hydrostatically pressured brittle rock beyond the thin plastic layer would have to act as a receptacle for the fluid. Whereas in later stages, larger volumes of rock have become sufficiently hot to act in a plastic manner and act as a storage receptacle for expelled fluid. The magmatic fluid may then act as a mineralizing agent, leading to so called epithermal deposits. These are often rich in valuable ores such as gold, silver or copper, and therefore of interest to mining operations (Fournier, 1999). To achieve long lasting magmatic intrusions without losing mass or volume to volcanic eruptions, low intrusion rates of magma are required, as mechanical models suggest that at very high intrusion rates of roughly $1e^{-2} \text{ m}^3$ per year, the resulting overpressure would almost certainly trigger eruptions before substantial volumes can accumulate (Karakas et al., 2017).

A major determinant of the heat flow from magmatic intrusions is the permeability of the rock, due to the predominantly advective nature of the heat transfer. Typical permeabilities of volcanic rocks are in the ranges of $1e^{-14} - 1e^{-15} \text{ m}^2$, with lower values reducing the overall heat transfer, but higher enthalpy and temperature than highly permeable formations, which exhibit a higher overall heat transfer. The higher temperature and enthalpy are enabled by the reduced ability of the pore fluid to migrate away from the heat source, leading to longer exposure to a magma source. Below permeabilities of $1e^{-16} \text{ m}^2$ the nature of heat transfer changes from largely convective to conductive dominated (Scott et al., 2015).

The potential of a downward migrating CO₂ plume is enabled by a density differential between supercritical water and CO₂. Above the critical temperature of pure water at $T = 374^\circ\text{C}$ and $T = 31.04^\circ\text{C}$ for CO₂, and the respective critical pressures of 21.8 MPa for water and 7.39 MPa for CO₂, the densities of these fluids equalize, with the tendency of CO₂ to have a higher density at increasing temperatures and pressures. This phenomenon was investigated by Parisio and Vilarrasa (2020) and showed promising results that confirmed the downward movement for

conditions akin to those encountered by IDDP-2 in the Krafla field in Iceland.

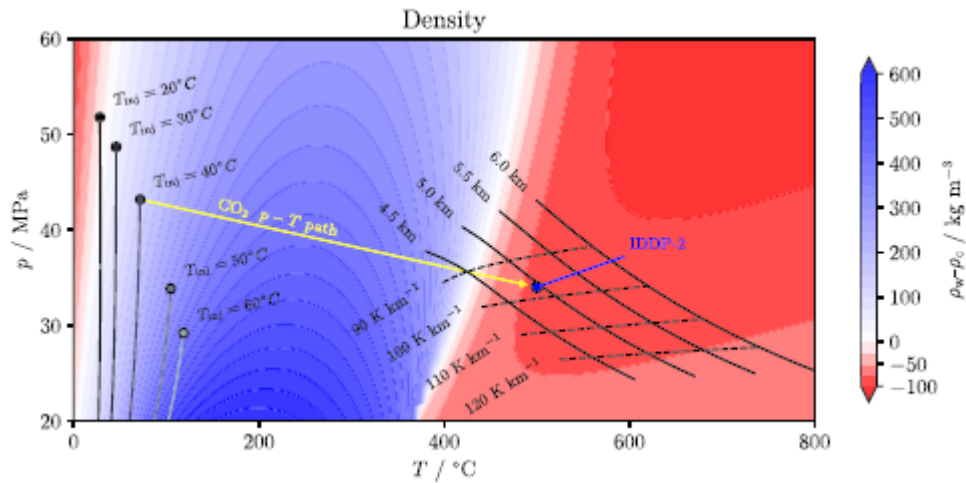


Figure 2 Graph detailing the density difference of water and CO₂ at pressures ranging from 20 MPa to 60 MPa and temperature ranging from 0°C to 800°C, Parisio and Vilarrasa, 2020

Figure 2 visualizes the density difference between water and CO₂ for temperatures ranging from 0°C to 800°C and for pressures ranging from 20 MPa to 60 MPa. The blue area denotes the regions in which water has a higher density than CO₂, the white areas denote the regions in which the densities are equal and the red area, above the critical temperature and pressure of both water and CO₂ denotes the regions in which the CO₂ density is higher. In this area of interest, the black lines represent the conditions found at the IDDP-2 project for various depths, underlining the potential applicability found in real world projects.

High-enthalpy geothermal systems may be used for electricity generation and waste heat utilization, increasing the efficiency of the system and providing clean energy. The combination of carbon sequestration and geothermal energy production may provide several benefits, such as repressurization of the reservoir, as well as a convenient location for energy and CO₂ intensive industries, such as steel or cement. In pursuing a more sustainable and environmentally friendly energy supply, supercritical geothermal resources, or enhanced geothermal systems, may play a pivotal role. Some of the characteristics of EGS, such as the longevity, low emissions and relatively widespread appearances, depending on the part of the world, make it seem like a desirable solution to contribute to the future energy supply. Estimates show that the thermal potential of all EGS in the United States is far greater than all of the country's hydrothermal resources (Tester et al., 2006).

This thesis aims to explore the temperature distribution caused by a magmatic intrusion in aforementioned high-enthalpy geothermal systems, with respect to CO₂ injection and migration behavior of the CO₂ plume. The evaluation and simulation of the system will be conducted using MOOSE (Multiphysics Object Oriented Simulation Environment), an open-source finite

element simulation program. The simulation will be in 2D and analyze the migration pattern of the CO₂ in the underground system depending on the well spacing and positioning. To achieve this goal, 21 cases at different permeabilities and injection points have been prepared and analyzed.

Chapter 2

Methodology and Model

The physical parameters used in this model, such as pressure, temperature and permeability, are based on data selected by Probst (2023) and Parisio and Vilarrasa (2020), amongst others, and meant to represent conditions resembling those encountered in real world examples, such as IDDP-2. These parameters, along with simulation parameters, like type of solver, boundary conditions and governing equations will be presented in this chapter.

The simulation is conducted in the MOOSE environment, an open-source, parallel finite element environment first developed by the Idaho National Laboratory. The Idaho National Laboratory is part of the US Department of Energy and is focused on research in nuclear and renewable energy systems and provides support and innovations in these areas. MOOSE was developed by and for scientist to be easy to use and allow users and developers to solve complex systems of partial differential equations. The framework was developed using trusted and established code, including libMesh and PETSc. LibMesh provides a framework for numerical simulation, with a special focus on mesh refinement and solving partial differential equations. PETSc stands for Portable, Extensible Toolkit for Scientific Computation and is focused on solutions for parallel PDEs in a scientific context (Giudicelli et al., 2024).

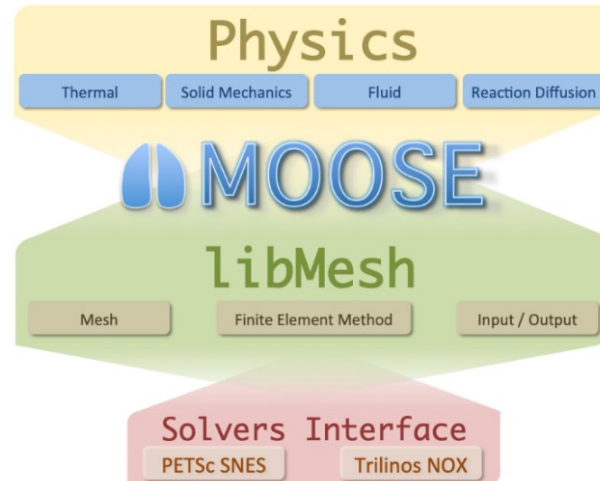


Figure 3 Architecture of the MOOSE framework illustrating the interaction between physics modules, the underlying libMesh library for finite element analysis and solver interfaces, Giudicelli et al., 2024

Figure 3 provides a high-level overview of how MOOSE operates. At the core of the framework is MOOSE, which serves as the interface connecting physics modules, such as Thermal, Solid Mechanics, Fluid, and Reaction Diffusion, with the underlying computational framework. MOOSE relies on libMesh, a C++ library for numerical simulation using the finite element method (FEM). libMesh handles key tasks such as meshing, input/output operations and the application of FEM to solve partial differential equations. At the base, MOOSE interfaces with external solver libraries like PETSc SNES and Trilinos NOX, which are used for nonlinear and linear system solving, ensuring efficient computations.

The MOOSE framework is a pluggable environment, resulting in a straightforward approach in which users are able to add objects to the code, which follows a defined structure documented in the description. The framework includes a number of components, such as the framework library which is the base system for all the other subsystems. Another would be the build system, which creates the applications for the following libraries and applications. Additionally, among other components, two frequently used ones for this thesis were the examples and tutorials, which quickly and understandably enable the user to gain an understanding of the simulation environment (Giudicelli et al., 2024).

The visualization of the results was conducted with ParaView. ParaView is an open-source tool for data visualization and analysis, commonly used in scientific research. It enables users to visualize complex datasets, explore data in 3D and perform analyses on large-scale data. The input into ParaView were the Exodus output files provided by MOOSE. In addition to the Exodus file used for these results, each case also contained a CSV file, detailing calculated parameters at various timesteps.

2.1 Kernel System and Calculation Parameters

The main part of the calculations within MOOSE is conducted by the Kernels systems. The Kernels are described as general physical equations, allowing the user to solve a large variety of problems. Each Kernel may denote one or more operators or terms in the weak formulation of a partial differential equation. Kernels may be added or removed by the user in the input file and can be selected from the long list of available Kernels or customized by the user.

The Kernels are assigned to Modules within MOOSE, which are designed to represent a certain set of combined physical equations and boundary conditions. It is recommended to only activate required Modules, as it will help in preventing errors and shorten the runtime. For this application, the “FLUID_PROPERTIES”, “HEAT_TRANSFER” and “POROUS_FLOW” Modules were used.

The PorousFlow module is a physics library designed for fluid and heat flow within porous media, such as the reservoir presented here. Its highly general formulation allows it to address problems involving any number of phases (such as gas, liquid) and fluid components (the species within each phase), using various sets of primary variables.

Heat transfer occurs through three primary mechanisms: conduction, convection, and radiation. The heat transfer module offers several implementations of the heat conduction equation. It also includes options for coupling temperature fields to fluid domains via boundary conditions. For this thesis, only the conduction and convection modes of heat transfer were considered.

FluidProperties objects provide interfaces for calculating the thermodynamic properties of fluids, including liquids and gases. This standardized procedure enables easy substitution of different fluids in an input file by simply changing the name of the Fluid Properties, allowing for greater adaptivity (Giudicelli et al., 2024).

The following descriptions of the Kernels used in the analysis will be based on the documentation of Moose, from Giudicelli et al., 2024.

2.1.1 PorousFlowMassTimeDerivative

The PorousFlowMassTimeDerivative Kernel in MOOSE is based on the mass conservation principle for fluids in porous media. It models the time-dependent change in the mass of fluid within the porous structure, accounting for variations in fluid saturation and density.

The equation it uses can be expressed as:

$$\frac{\partial}{\partial t} (\phi \sum_{\beta} S_{\beta} \rho_{\beta} \chi_{\beta}^{\kappa}) \quad (1)$$

Where:

- ϕ represents the porosity.
- S_{β} is the saturation of the phase β .
- ρ_{β} indicates the phase β density.
- χ refers to the mass fraction of phase β .

This formula essentially captures the rate of mass accumulation in porous media over time by incorporating factors like porosity, fluid density, and saturation.

2.1.2 PorousFlowAdvectiveFlux

The PorousFlowAdvectiveFlux Kernel is a fundamental component in the simulation of fluid movement through porous media, driven by pressure gradients. It is based on the principles of Darcy's law and incorporates the properties of both the fluid and the porous structure. The Kernel is implemented twice, same as PorousFlowMassTimeDerivative, to account for the flux of water and CO₂.

The flux is driven by pressure gradients and can be expressed as follows:

$$q = -k\nabla P \quad (2)$$

Where:

- q is the rate of fluid flow per area.
- k is the permeability of the porous medium.
- ∇P is the pressure gradient responsible for driving the fluid.

2.1.3 PorousFlowEnergyTimeDerivative

The PorousFlowEnergyTimeDerivative Kernel in MOOSE has been developed with the specific purpose of calculating the time-dependent evolution of energy within a porous medium. The Kernel tracks the temperature dependent evolution of energy within the porous medium, taking into account both heat storage and transport. This Kernel is of particular

importance in simulations where energy conservation is a requirement, such as in geothermal processes or heat transfer scenarios as with this model of CO₂ injection.

The following expression represents the time derivate used in the Kernel:

$$\frac{\partial}{\partial t} ((1 - \phi)\rho_R C_R T + \phi \sum_{\beta} S_{\beta} \rho_{\beta} \varepsilon_{\beta}) \quad (3)$$

Where:

- ϕ is the porosity of the porous medium.
- ρ_R is the grain density of the rock.
- C_R is the specific heat capacity of the grains.
- T is the temperature.
- S_{β} is the saturation of the phase β .
- ρ_{β} indicates the phase β density.
- ε_{β} represents the internal energy of the fluid phase β .

2.1.4 Heat flow and associated Kernels

The heat flow in the model is governed by the heat equation:

$$0 = \frac{\partial}{\partial t} ((1 - \phi)\rho_R C_R T + \phi \rho \varepsilon) + ((1 - \phi)\rho_R C_R T + \phi \rho \varepsilon) \nabla v_s - \lambda \nabla^2 T - \nabla_i (h \rho \frac{k_{ij}}{\mu} (\nabla_j P - \rho g_j)) \quad (4)$$

Where the first term is represented by the PorousFlowEnergyTimeDerivative from chapter 2.1.3 and the second term, which represents volumetric expansion is neglected, as it is more closely related to the thermo-mechanical behavior of the reservoir rock, which is not within the scope of this thesis.

The term $\lambda \nabla^2 T$ represents the heat conduction in the reservoir and is implemented by the PorousFlowHeatConduction Kernel.

The term $\nabla_i (h \rho \frac{k_{ij}}{\mu} (\nabla_j P - \rho g_j))$ represents the heat advection and is implemented by the PorousFlowHeatAdvection Kernel.

2.2 Fluid Properties

The Fluid Properties system in MOOSE has been developed to handle the thermodynamic characteristics of fluids, both liquids and gases. This system provides an interface for calculating a range of fluid properties, including density, viscosity, thermal conductivity and specific heat.

The properties of water are defined by “Water97FluidProperties”, which is in accordance with the IAPWS Industrial Formulation 1997. This formulation was designed primarily for use in the power sector and is designed to provide quick computations when compared to older models. The range of validity is up to $T = 1173.15$ K and a pressure of < 100 MPa, and up to $T = 2273.15$ K for pressures of < 50 MPa (Wagner et al., 2000). The pressures and temperatures encountered in this work are well within the IAPWS Formulation limits.

The fluid properties for carbon dioxide are primarily derived from the Span and Wagner equation of state (1996), which calculates properties like density, enthalpy and internal energy based on density and temperature. However, in the MOOSE framework's Fluid Properties module, pressure and temperature are used as the primary variables, aligning with the needs of the Porous Flow module. To determine CO₂ properties, the module first iteratively computes density for a given pressure and temperature. Once the density is found, it is used to calculate other properties, such as internal energy (Giudicelli et al., 2024).

For viscosity, the formulation from Fenghour et al. (1998) is applied, while thermal conductivity is based on the work of Scalabrin et al. (2006). Additionally, CO₂ dissolution in water follows Henry's law, according to the IAPWS guidelines (2004). The validity of the CO₂ Fluid properties ranges from 216.59 K $< T < 1100$ K for pressures below 800 MPa (Giudicelli et al., 2024). Similarly to water, the temperatures and pressures encountered in this work are within the limits, although the maximum temperature of $T = 1100$ K may limit future research with temperatures exceeding this value.

2.3 Injection and Production

The injection of CO₂ and production of water is simulated using Dirac Kernels. Dirac Kernels in MOOSE are used to apply point constraints in a simulation, often representing sources or sinks. These Kernels assist in the introduction of actions at specific points, such as boundary conditions or point loads (Giudicelli et al., 2024).

The CO₂ is injected at a rate of 6 kg/s via a pulse point source, which is defined by the point of injection, the mass flux in [kg/m³] and the variable for the flux, in this case CO₂. The temperature influence of the CO₂ injection at $T = 333.15$ K is simulated with a Dirichlet

Boundary condition at this same injection point. At this temperature the cooling effect of the injection is only in close proximity to the borehole, in accordance with the analysis conducted by Parisio and Vilarrasa (2020).

The production of water is modelled with the Dirac Kernel “PorousFlowPacemanBorehole”, which is a special case of a line sink. This special case has the benefit that it can produce more than one fluid, whereas a sink is limited to the specified variable. The usage of this particular sink was done in accordance to Probst (2023) and will not be explained in further detail, as the produced fluids and energy are not within the scope of this thesis.

2.4 Material Properties of the Reservoir

The permeability of the reservoir is assumed to be isotropic and ranges from $k = 1e^{-14} \text{ m}^2$, or 10 mD, to $k = 1e^{-15} \text{ m}^2$, or 1 mD. These values are within the range expected for a fractured basaltic crust affected by magmatic intrusions (Parisio and Vilarrasa, 2020; Hurwitz et al., 2007).

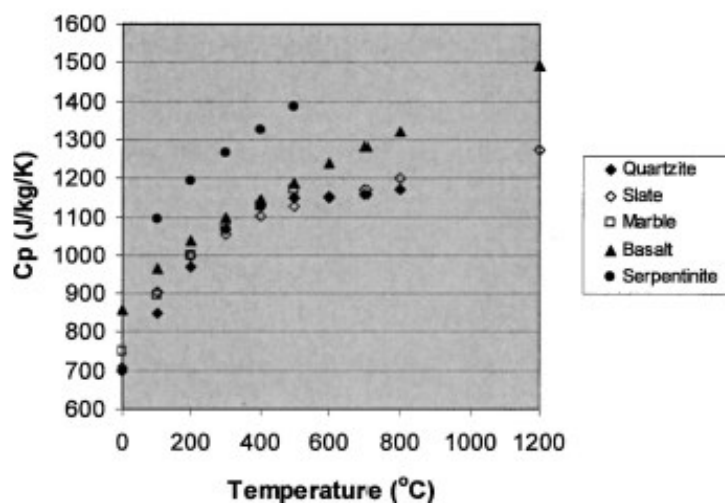


Figure 4 Specific heat of different rock types plotted against temperature ranging from 0°C to 1200°C, Waples and Waples, 2006

Figure 4 was used for the determination of the specific heat of the reservoir rock. The average reservoir temperature of the cases with distributed temperature profile at 653.9 K, the case with constant temperature at $T = 773.15 \text{ K}$, and the highest temperature of the magma source at $T = 1000 \text{ K}$, in closer proximity to the injection points in the lower half of the reservoir, led to a specific heat capacity of basalt of $c_p = 1200 \text{ J/kg/K}$ being selected, corresponding to a temperature of roughly 500°C or 773.15 K. This value is also in accordance to the previous analysis conducted by Probst (2023).

Other rock data include:

Table 1 Reservoir rock parameters selected for the simulations

Grain Density	$\rho = 2500 \text{ kg/m}^3$
Bulk Modulus	$K = 2 \text{ GPa}$

2.5 Solver and Preconditioning

Preconditioning is used in numerical models to enhance the convergence and speed of the calculations. MOOSE first attempts to use the LU factorization preconditioner with MUMPS (Multifrontal Massively Parallel Solver), which is designed for large sparse matrices and parallel computing. The LU factorization preconditioner is based on traditional iterative methods such as Gauss or Jacobi (Gogoleva, 2018). This preconditioner is powerful but might not always be available, hence the fallback options. MUMPS does not have GPU support, meaning improper memory management may lead to the unavailability (Ghysels and Synk, 2022).

Fallback Preconditioner: The second option is to use the Additive Schwarz Method (ASM) preconditioner with LU factorization on subdomains. ASM works on the principle of only solving small problems in the system in every iteration (Brenner and Scott, 2008).

The injection of CO₂ was delayed by one timestep with a control block, as that has shown an improvement in the convergence speed of the simulations. The solver chosen for the CO₂ injection cases was “Transient” with the Newton method. The maximum timestep was half a year and the minimum timestep 1000 seconds. All simulations reached the final timestep of 30 years.

2.6 Mesh and Model Parameters

The 2D mesh for this simulation was created using GMSH, an open-source software for generating meshes in 1D, 2D, and 3D simulations. The mesh dimensions are 800 meters in width and 1050 meters in height.

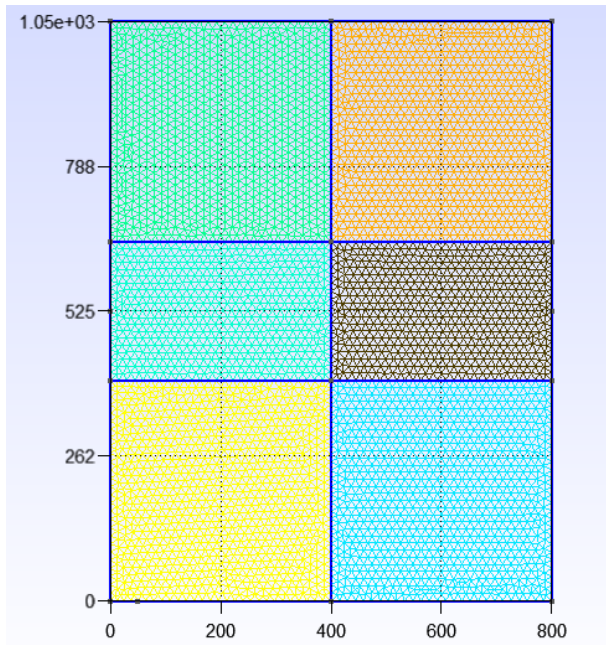


Figure 5 Illustration of the mesh used for further analysis, along with coordinates which will be referred to in analysis

In the mesh there are two distinct points, which are (0, 525) and (800, 525), these are the boreholes used for the initial, or base case, injection and production of CO₂ and water respectively. Both wells are modelled to be horizontal. The wells are added as Physical Points in the mesh and adapted to the investigated cases. This mesh was loaded into an equilibrium file for the temperature distribution, which was then the source for the CO₂ injection cases.

2.7 Boundary Conditions

In any numerical simulation, the setting of appropriate boundary conditions plays a pivotal role, as they define the artificial boundary of the system and must be selected in order to closely approximate real-world conditions. In addition to serving the simulations validity, improper boundary conditions may negatively impact the convergence of the simulation (Blazek, 2005).

The boundary conditions considered in these simulations were Dirichlet, or constant boundary, conditions. The Dirichlet conditions represent at constant physical value at the outer boundary of the system, such as temperature, pressure or concentrations of fluid phases (Hillel, 2005).

Following is a brief overview of the boundary conditions applied in the different simulations.

Table 2 Boundary conditions for the equilibrium file with the active magma source

Location of the BC	Value and parameter
Top of reservoir	Pressure $p = 31$ MPa
Top of reservoir	Temperature $T = 400$ K
Bottom left, Magma source	Temperature $T = 1000$ K

The pressure of 31 MPa corresponds to the top of the reservoir pressure and was chosen in accordance with conditions selected by Probst (2023).

Table 3 Boundary conditions of the constant temperature case, in accordance to the simulations by Probst (2023)

Location of the BC	Value and parameter
Top of reservoir	Pressure $p = 31$ MPa
Top of reservoir	Temperature $T = 773.15$ K

Table 4 Boundary conditions for the CO₂ injection cases

Location of the BC	Value and parameter
Injection point	Temperature $T = 333.15$ K

The injection temperature chosen was $T = 333.15$ K (60°C) in accordance with the supervisors, as higher injection temperatures result in increased costs for compression and heating. In addition to this, the CO₂ is in the critical state at these conditions and efficient to inject due to higher density and lower viscosity. CO₂ is also more corrosive at higher temperatures. The location of this boundary condition corresponds to the injection points detailed in chapter 2.8.2.

2.8 Scenarios

The analysis in this thesis is structured in two main stages to evaluate the behavior of the CO₂ plume in the reservoir influenced by a magmatic intrusion.

The first phase focuses on simulating the coupled hydrothermal processes within a fully water-saturated reservoir under the influence of a magmatic intrusion. This intrusion was modelled as a 400 m wide heat source located in the bottom left corner of the mesh, which created a temperature distribution within the reservoir. The simulation continued until the system reached steady state conditions. The output files from these steady state simulations provided the mesh to be used in the second phase.

In the second phase, the steady state conditions from the first phase are used as the initial conditions to simulate the CO₂ injection at different locations in the reservoir. This phase was designed to assess how the injected CO₂ plume interacts with the temperature- and pressure gradients and fluid properties created by the magmatic source. By investigating different injection points, this phase analyzed how CO₂ behaves in a reservoir with the coupled hydrothermal conditions created by a magmatic intrusion.

2.8.1 Temperature and Pressure Equilibration

Table 5 Cases for equilibrium

Heat Source	Average Temperature	Distribution	Permeability
1000 K 400 m bottom left corner	653.99 K	Distributed	1e ⁻¹⁶ m ²
773.15 K top boundary	773.15 K	Constant	1e ⁻¹⁶ m ²

Table 5 details the two cases of the pressure and temperature equilibrium files, which initialize the temperature field used for subsequent injection CO₂ detailed in Chapter 2.8.2. This initialization ensures that the conditions are stable before the CO₂ is injected. The main assumptions for these simulations were a fully water saturated reservoir at 15% porosity and a permeability of $k=1e^{-16} \text{ m}^2$. Both cases reached steady state conditions. This equilibration step is driven through the density variations of the resident water in the reservoir, thus creating a

realistic temperature distribution. Permeability values of $k= 1e^{-15} \text{ m}^2$ and $k= 1e^{-14} \text{ m}^2$ were tested in the early phases of the equilibrium simulation, but in addition to convergence issues at those higher permeabilities, the temperature distribution at the scale of the model was less discernable than that with the selected case. For these reasons the permeability of $k= 1e^{-16} \text{ m}^2$ was used for the equilibrium simulation to reach the steady state conditions and the coupled hydrothermal fluid properties. MOOSE allows the user to import the mesh used for a simulation into another simulation case. The user can specify which parameters to use for the initial conditions, and the permeability value can be specified separately. This means that the permeability of $k= 1e^{-16} \text{ m}^2$ was used exclusively for the equilibrium and the permeabilities used for the CO_2 injection cases are specified in Chapter 2.8.2.

The constant temperature of $T=773.15 \text{ K}$ was chosen, as the average temperature 653.99 K from the first case was insufficient in providing the desired downward migration pattern. The value was subsequently chosen as sinking behavior was demonstrated at this temperature by Probst (2023).

2.8.2 CO_2 Injection Cases

Table 6 Description of parameters for the 21 cases of CO_2 injection

Injection on the left side		
Depth	Permeability	Temperature
200 m	$1e^{-14} \text{ m}^2$	distributed
400 m	$1e^{-14} \text{ m}^2$	distributed
525 m	$1e^{-14} \text{ m}^2$	distributed
200 m	$1e^{-15} \text{ m}^2$	distributed
400 m	$1e^{-15} \text{ m}^2$	distributed
525 m	$1e^{-15} \text{ m}^2$	distributed
200 m	$5e^{-15} \text{ m}^2$	distributed
400 m	$5e^{-15} \text{ m}^2$	distributed
525 m	$5e^{-15} \text{ m}^2$	distributed

Injection on the right side		
Depth	Permeability	Temperature
200 m	$1e^{-14} \text{ m}^2$	distributed
400 m	$1e^{-14} \text{ m}^2$	distributed
525 m	$1e^{-14} \text{ m}^2$	distributed
200 m	$1e^{-15} \text{ m}^2$	distributed
400 m	$1e^{-15} \text{ m}^2$	distributed
525 m	$1e^{-15} \text{ m}^2$	distributed
200 m	$5e^{-15} \text{ m}^2$	distributed
400 m	$5e^{-15} \text{ m}^2$	distributed
525 m	$5e^{-15} \text{ m}^2$	distributed
Injection at a constant temperature of 773 K		
Depth	Permeability	Temperature
525 m	$1e^{-14} \text{ m}^2$	constant
525 m	$1e^{-15} \text{ m}^2$	constant
525 m	$5e^{-15} \text{ m}^2$	constant

Table 6 details the parameters of the 21 cases conducted for the analysis of the CO₂ plume behavior. While only the temperature, injection point and permeability are mentioned above, the water viscosity, density and pressure from the fully water saturated equilibrium files described in Chapter 2.8.1 are also imported as initial conditions. All of the cases were simulated to the maximum injection time of 30 years. The temperature variable “distributed” describes the injection into the reservoir initialized by the equilibrium simulation described in Chapter 2.8.1 by the 1000 K magma source.

2.9 Gravity Number Calculation

One way to quantitatively analyze the migration patterns of the CO₂ plume is to calculate the gravity number at various locations. This number describes the ratio of the viscous forces related to the gravitational forces in the CO₂-water system. When the gravity number, which is a dimensionless unit, has a large value, the gravitational forces dominate, resulting in more

vertical movement, dependent on the density of both phases. When the number is small, the viscous forces dominate, dependent on the permeability structure, and result in more horizontal movement, leading to bell shaped patterns (Ide et al., 2007).

The gravity number proposed by Zhou et al. (1994) and used by Ide et al. (2007) amongst others, for the analysis of CO₂ migration patterns is as follows:

$$N_{gv} = \frac{k_v L \Delta \rho g}{H u \mu_{brine}} \quad (5)$$

Where:

- k_v is the vertical permeability.
- L is the length of the aquifer.
- $\Delta \rho$ is the difference in density between water and CO₂.
- g is the gravity acceleration.
- H is the height of the aquifer.
- u is the average Darcy flow velocity.
- And μ_{brine} is the viscosity of the water.

For this analysis however, the same definition of the gravity number used by Probst (2023) and Parisio and Vilarrasa (2020) will be used. In this case the consensus is that a gravity number larger than 1 indicates gravity dominated behavior, increasing the buoyancy effects. Conversely, when N_{gv} is lower than 1, the gas tends to float. It is defined as:

$$N_{gv} = \frac{2\pi d r_{ch} \Delta \rho g \rho_{ch}}{Q_m \mu_{CO_2}} \quad (6)$$

Where:

- d represents the thickness of the CO₂ plume.
- r_{ch} is the horizontal distance of the point to the injection.
- k is the permeability of the reservoir in m².
- $\Delta \rho$ is the difference in density between water and CO₂.
- g is the gravitational acceleration.
- ρ_{ch} is the density of the CO₂ in kg/m³ at the investigated point.
- μ_{CO_2} is the viscosity in Pa s.
- And Q_m is the mass flow rate in kg/s.

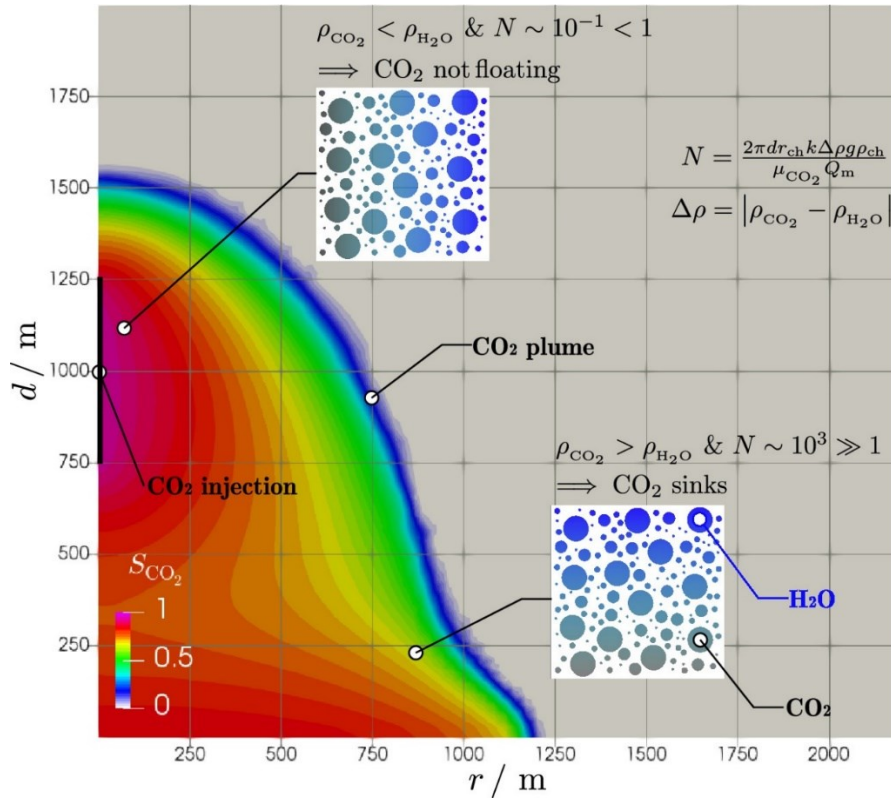


Figure 6 This illustration details the behavior of the injected CO₂ plume along with the gravity numbers, showing the viscous dominated behavior in the near wellbore region and the gravity numbers in the lower part of the plume which are greater than 1, indicating sinking behaviour due to the higher density of CO₂, Parisio and Vilarrasa, 2020

The determination of the thickness of the CO₂ plume is a difficult task, due to the migration patterns witnessed in the Results section of the thesis. For comparability between the cases, the determination of it was selected based on the permeability and kept constant throughout the different injection points. For the permeability of 10 mD ($k=1e^{-14} \text{ m}^2$) the thickness of the plume was selected at 600 m, for the 5 mD case ($k=5e^{-15} \text{ m}^2$) and 1md ($k=1e^{-15} \text{ m}^2$) an average thickness of 450 m was determined. These thicknesses are kept constant for all cases.

The densities of both phases, as well as the viscosity are cell data in the exodus files from MOOSE, so for the calculation of the gravity numbers the “Convert Cell Data to Point Data” filter in ParaView was used to obtain the data at the desired points. This resulted in three data points for every investigated cell, where the average of each was calculated to get accurate point data. The horizontal distance to the injection was calculated using the coordinates of the injection well and the coordinates of the investigated points.

For each injection case three points were selected, which is one point at the same height as the injection and 100 m to the left or right, depending on the injection side, one point 100 m below and 50 m to the left or right depending on the injection side and one point 100 m above and 50 m to the left or right, depending on the injection coordinates. This approach was kept constant

through all the cases described in Chapter 2.8.2. The calculated averages of the parameters along with the gravity numbers are presented in tabular form. All of this data presented in the tables refers to the data depicted by the Figure above it.



Figure 8 Example of the position of points for Ngv calculation for an injection depth of 200 m

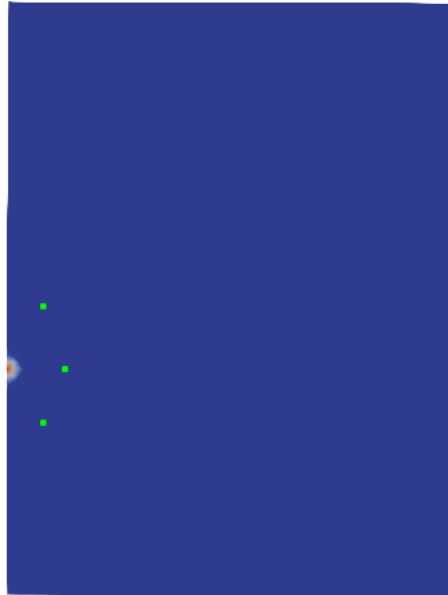


Figure 7 Example of the position of points for Ngv calculation for an injection depth of 400 m



Figure 9 Position of Ngv calculation points at 200m on the right side

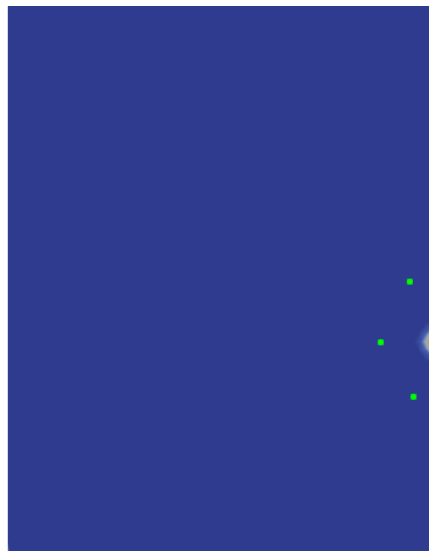


Figure 10 Position of Ngv calculation points at 400m on the right side

Chapter 3

Results

The following part of the thesis details the results obtained through the cases discussed in chapter 2.8.2. The first part includes the results from the equilibrium phase, to show the input files to be used for the CO₂ injection cases, and the second part details the injection cases. The cases are presented by graphs highlighting the saturation of the CO₂, to visualize the plume behavior and migration patterns. The results are structured by injection side and permeability. All of the figures detail the CO₂ saturation at the final timestep after 30 years. In addition to the saturation profiles, the pressure over time profiles at various injection points are also presented in this Chapter.

3.1 Equilibration Results

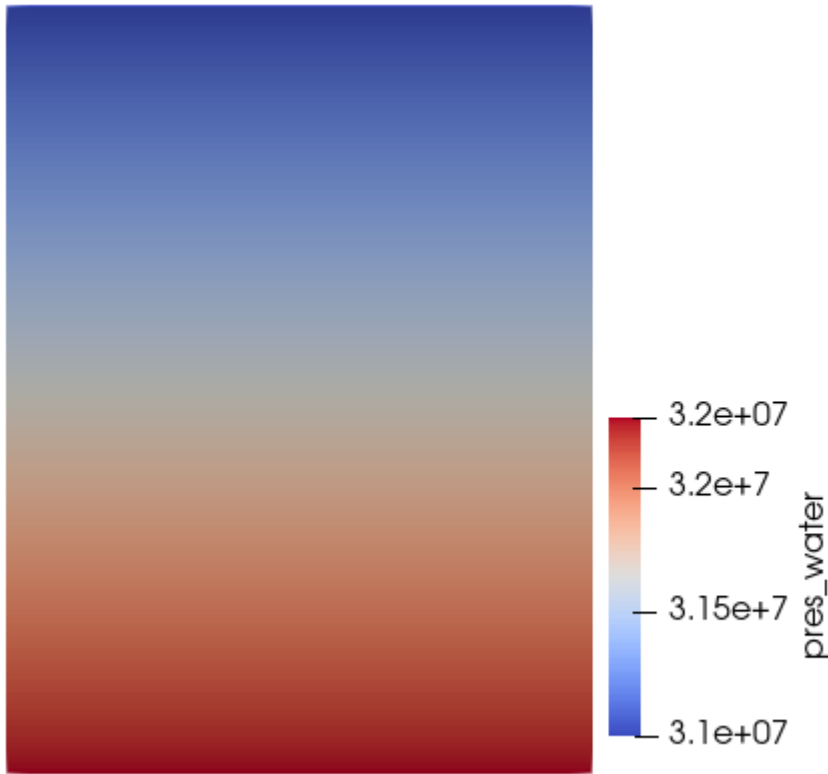


Figure 11 Pressure profile of the equilibrium file at a constant temperature of $T = 773.15$ K

Figure 11 shows the pressure profile of the constant temperature case, increasing due to gravity effects. The reservoir is fully water saturated and reached a steady state. As such, the solver type was changed from “Transient” to “Steady”. As was confirmed by Parisio and Vilarrasa (2020) and Probst (2023), this temperature profile is sufficient to witness a clear sinking tendency of a CO_2 plume. The profile and injection into this reservoir will further be used to demonstrate the consistency of the calculations and input files utilized for this thesis. This file at a constant temperature of $T = 773.15$ K is used as the input file for those cases labeled “773 K constant” in the temperature column of Chapter 2.8.2.

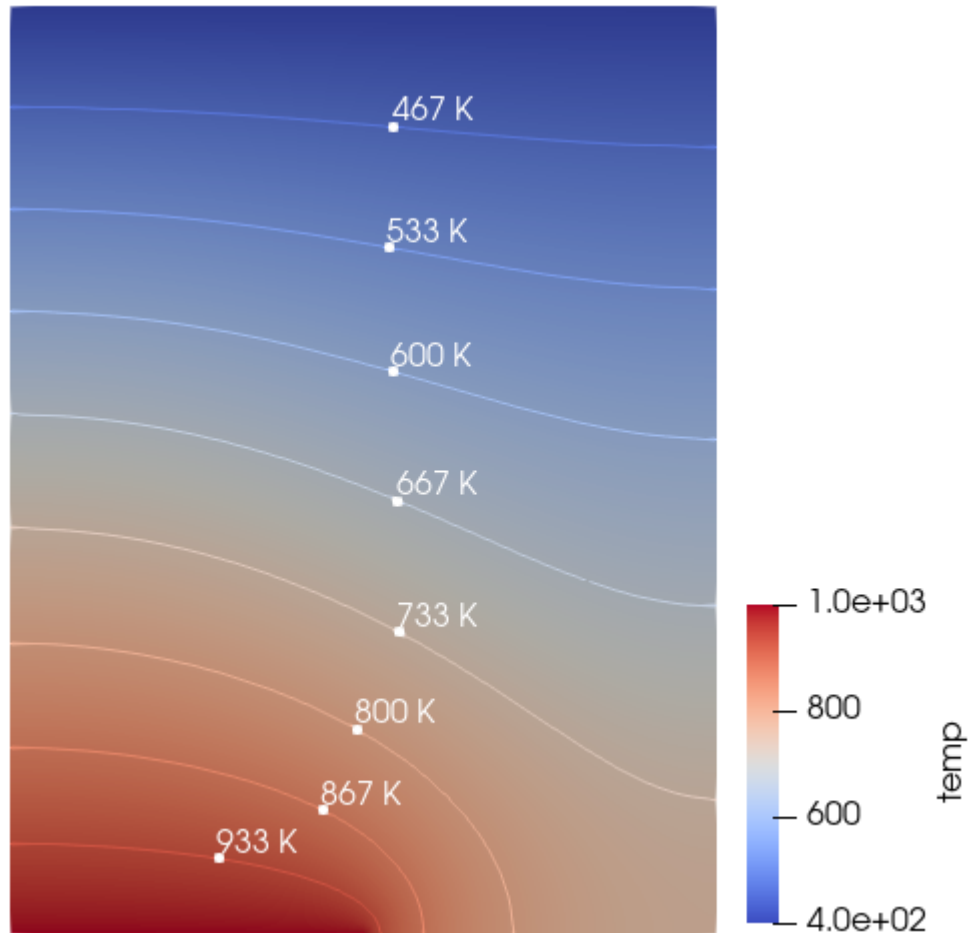


Figure 12 Temperature distribution of the equilibrium case with a 1000 K magma source

Figure 12 displays the temperature distribution achieved by having a magma source act on the bottom left half of the mesh. This magma source ranges from the coordinates $[0, 400] \times \{0\}$ and has a constant temperature defined as a Dirichlet Boundary Condition at a temperature $T = 1000$ K. As can be seen in the figure, the isotherms are sloping downward to the right, this along with the output data confirms the temperature gradient to be higher on the left side, closer to the heat source, than on the right side. The output data for the point $(0, 525)$ confirms a temperature of 700.68 K, the middle of the mesh at $(400, 525)$ to be at 658.01 K and the right side $(800, 525)$ at 613.22 K. This distribution brings forth the hypothesis that the sinking behavior of injected CO_2 should be amplified on the “hot side” and will be analyzed and examined in the following examples of CO_2 injection.

3.2 CO₂ Injection at constant temperature

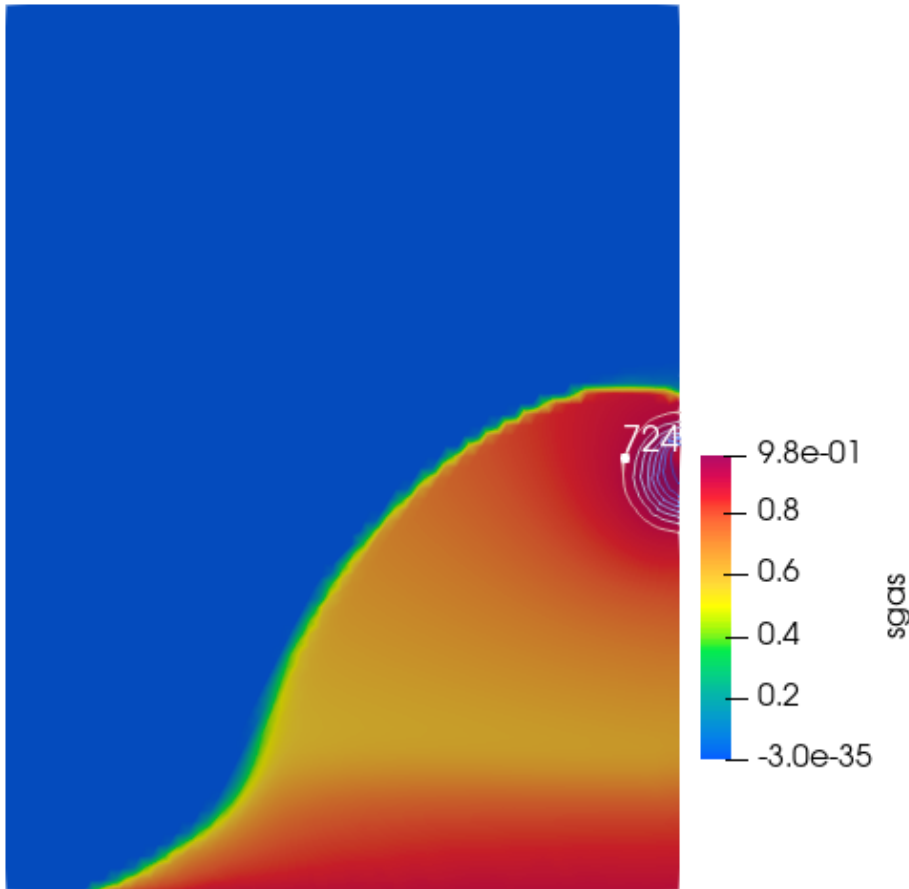


Figure 13 CO₂ injection for 30 years at $k=10$ mD and constant temperature at $T=773.15$ K

Table 7 Density of water and CO₂ [kg/m³], CO₂ viscosity [Pa·s] and gravity number for case above

x-coordinate	y-coordinate	Density CO ₂	Density Water	Viscosity CO ₂	Gravity Nr.
705.38	521.96	199.29	120.34	3.76E-05	2.44
748.27	421.23	202.34	124.86	3.75E-05	1.33
749.81	621.59	196.11	115.89	3.77E-05	1.29

Figure 13 confirms the analysis of Probst (2023) that CO₂ injected into a reservoir at a constant temperature of $T=773.15$ K would migrate to the bottom of said reservoir. This comparative result allows for a more thorough analysis of the behavior depending on temperature distribution and permeability effects. The isotherms near the injection point at (800, 525) show the cooling effect of cold CO₂ injection at 333.15 K. As mentioned in Chapter 2.3, the cooling effect at relatively short injection durations only effects the immediate wellbore surroundings and does not seem to negatively impact the downward migration pattern of the plume. The gravity numbers calculated in Table 7 confirm the witnessed tendencies, with all three numbers

being higher than 1 and thus promoting the sinking of CO₂ due to the higher densities and buoyancy dominated behavior.

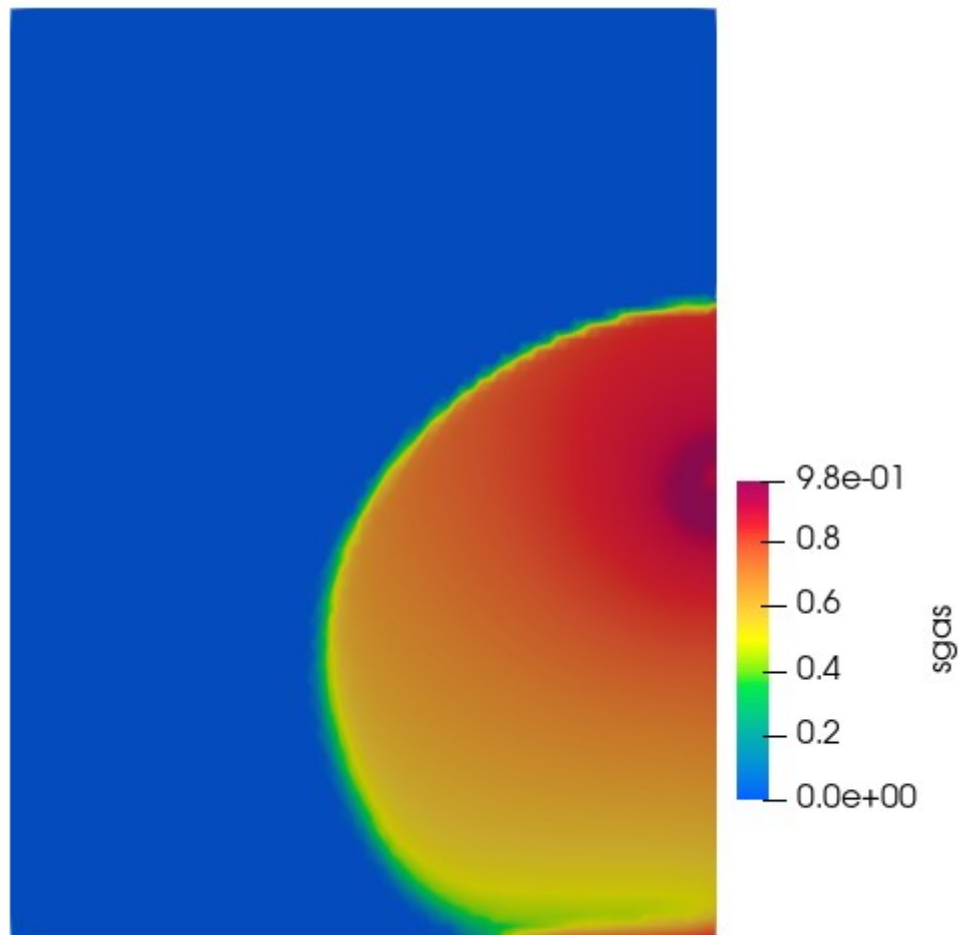


Figure 14 CO₂ injection for 30 years at $k=5\text{mD}$ and constant temperature at $T=773.15\text{K}$

Table 8 Density of water and CO₂ [kg/m³], CO₂ viscosity [Pa·s] and gravity number for case above

x-coordinate	y-coordinate	Density CO ₂	Density Water	Viscosity CO ₂	Gravity Nr.
705.38	521.96	201.63	122.95	3.76E-05	0.92
748.27	421.23	201.64	121.95	3.78E-05	0.51
749.81	621.59	197.92	117.60	3.78E-05	0.49

Figure 14 includes a case not previously analyzed by Probst. The additional case at a permeability of 5 mD was chosen to provide more comparative results and closely examine the distinctive permeability-based differences between 10 mD and 1 mD. As expected for a lower permeability value at the constant temperature, there is still a clear sinking tendency visible,

although the injected CO₂ takes more of a bulb shape. This is confirmed by the gravity numbers, all indicating a more viscous based pattern opposed to the case with 10 mD permeability.

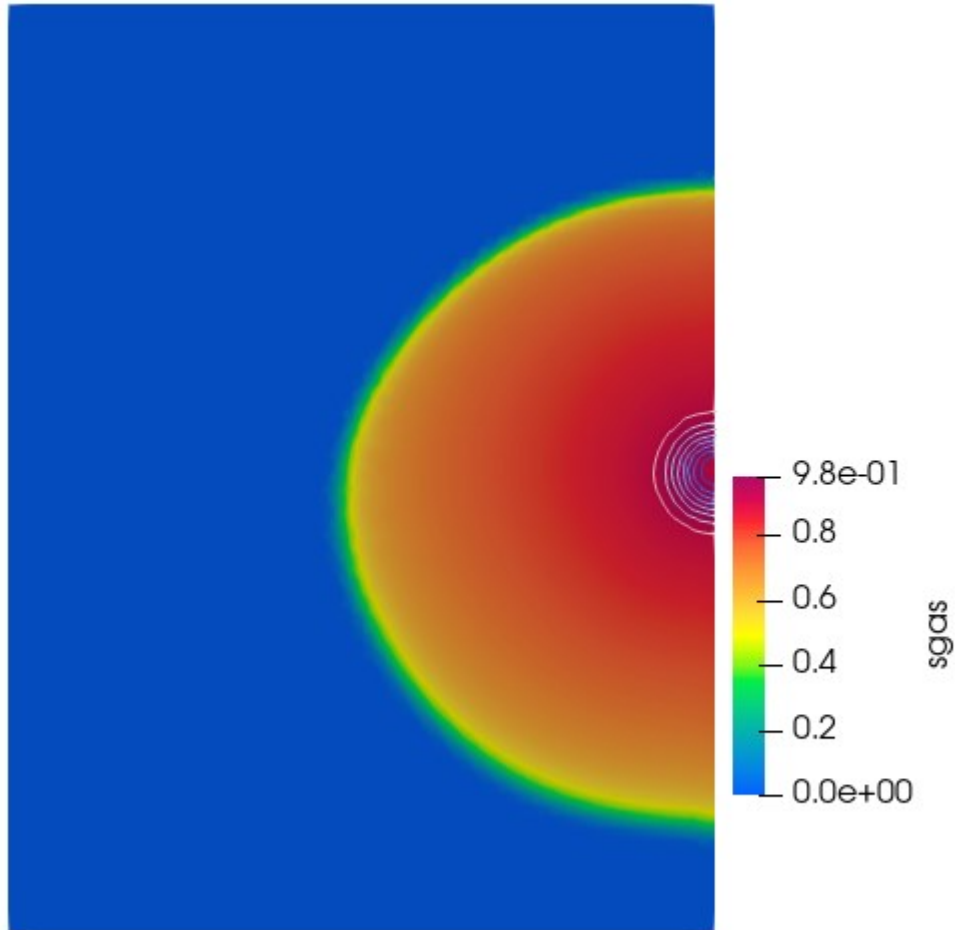


Figure 15 CO₂ injection for 30 years at $k=1\text{mD}$ and constant temperature at $T=773.15\text{ K}$

Table 9 Density of water and CO₂ [kg/m³], CO₂ viscosity [Pa·s] and gravity number for case above

x-coordinate	y-coordinate	Density CO ₂	Density Water	Viscosity CO ₂	Gravity Nr.
705.38	521.96	215.51	137.49	3.81E-05	0.19
748.27	421.23	213.84	133.29	3.83E-05	0.11
749.81	621.59	211.44	130.90	3.82E-05	0.10

Figure 15 confirms the result from Probst (2023), resulting in more of a uniform shape, exhibiting a sinking tendency but migrating further towards the reservoir top. Compared to the result in Figure 13, one can observe that the cooling effect of the cold CO₂ injection is only marginally smaller than in the high permeability case. The calculated gravity numbers are even

smaller than in the previous case, resulting in the more uniform shape observed due to the horizontal, viscous-dominated movement of the plume.

3.3 CO₂ Injection on the left side at 10 mD permeability

3.3.1 Injection 200 m above the bottom reservoir boundary

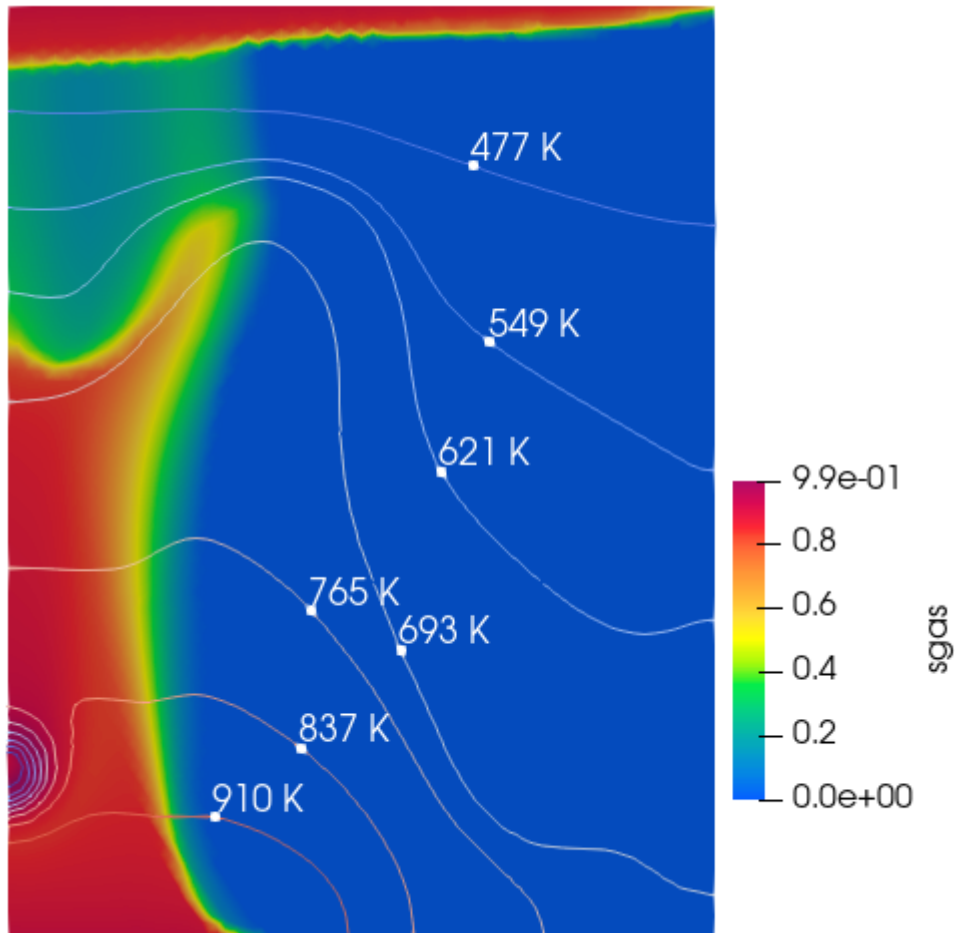


Figure 16 CO₂ injection for 30 years at $k=10\text{mD}$ and 200 m above the reservoir boundary

Table 10 Density of water and CO₂ [kg/m^3], CO₂ viscosity [$\text{Pa}\cdot\text{s}$] and gravity number for case above

x-coordinate	y-coordinate	Density CO ₂	Density Water	Viscosity CO ₂	Gravity Nr.
105.65	198.63	178.12	92.22	4.04E-05	2.47
52.90	96.04	167.12	82.86	4.20E-05	1.09
56.83	297.03	188.33	102.96	3.91E-05	1.44

Figure 16 details the first instance in this analysis of CO₂ injection into a reservoir with the distributed temperature profile described in Chapter 3.1. In this case the injection point is at the lowest point analyzed in this thesis at 200 m above the magma source, at point (0, 200). The permeability in this case was 10 mD at an even higher temperature than the constant temperature case, which exhibited a clear sinking tendency. This led to the belief that CO₂

would act in a similar manner than what was previously observed. The gravity numbers do indeed confirm a gravity dominated behavior, although unexpectedly there seems to be a higher tendency for upward migration of the CO₂ plume than for downward movement.

3.3.2 Injection 400 m above the bottom reservoir boundary

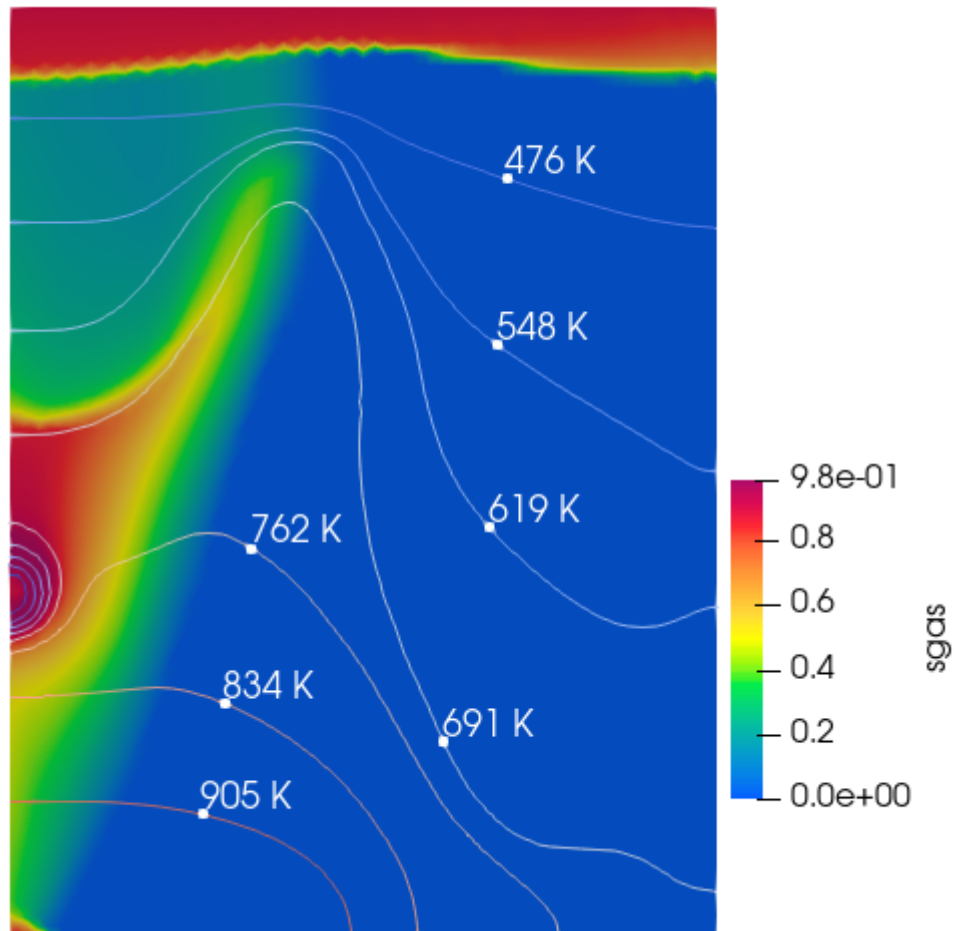


Figure 17 CO₂ injection for 30 years at $k=10$ mD and 400 m above the reservoir boundary

Table 11 Density of water and CO₂ [kg/m³], CO₂ viscosity [Pa·s] and gravity number for case above

x-coordinate	y-coordinate	Density CO ₂	Density Water	Viscosity CO ₂	Gravity Nr.
95.86	395.38	202.83	123.85	3.77E-05	2.51
50.96	297.55	190.09	104.86	3.90E-05	1.30
50.59	503.16	215.92	158.71	3.66E-05	1.05

Figure 17 details the CO₂ behavior for a permeability of 10 mD at 400 m above the magma source. The gravity numbers closely resemble the ones from Table 10, indicating more vertical

than horizontal movement. The higher density of CO₂ compared to water, along with the gravity numbers should lead to a sinking behavior, but in reality, quite the opposite can be observed.

3.3.3 Injection 525 m above the bottom reservoir boundary

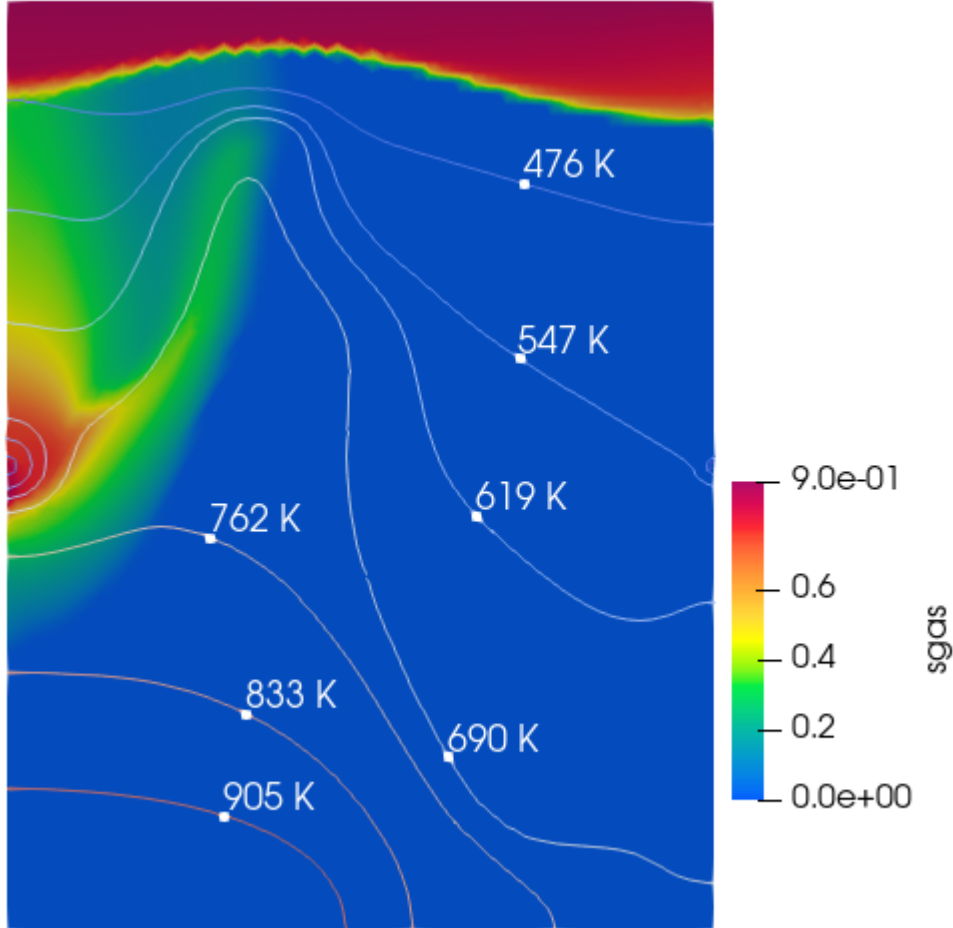


Figure 18 CO₂ injection for 30 years at $k=10\text{mD}$ and 525 m above the reservoir boundary

Table 12 Density of water and CO₂ [kg/m³], CO₂ viscosity [Pa·s] and gravity number for case above

x-coordinate	y-coordinate	Density CO ₂	Density Water	Viscosity CO ₂	Gravity Nr.
94.79	522.06	217.94	166.06	3.65E-05	1.81
51.76	421.28	203.38	124.38	3.77E-05	1.36
50.66	621.58	242.43	551.48	3.51E-05	6.67

Figure 18 depicts even less of a sinking tendency than the previous cases. The permeability has been kept constant at 10 mD and the injection depth has been moved up by 525 m, the same height as the three cases observed in Figures 13, 14 and 15. The vertical migration pattern is confirmed by the calculated gravity numbers. The third gravity number calculated is of particular interest, as the value of 6.67 is rather high, but the density of water is almost double

that of CO₂. This can be explained by the temperature at T=651.4 K at this point. The density difference caused by the lower temperature along with the high gravity number present a plausible explanation for the strong upward migration pattern which can be observed in Figure 18.

3.4 CO₂ Injection on the left side at 5 mD permeability

3.4.1 Injection 200 m above the bottom reservoir boundary

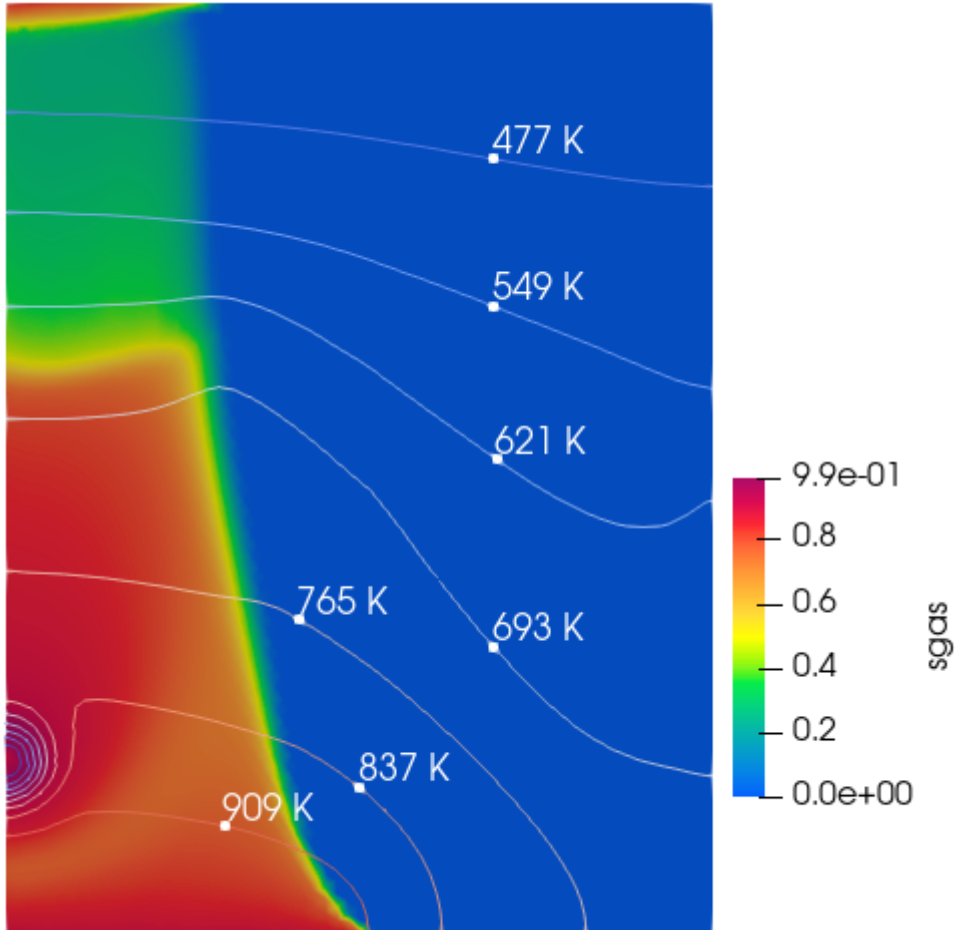


Figure 19 CO₂ injection for 30 years at $k=5\text{mD}$ and 200 m above the reservoir boundary

Table 13 Density of water and CO₂ [kg/m^3], CO₂ viscosity [$\text{Pa}\cdot\text{s}$] and gravity number for case above

x-coordinate	y-coordinate	Density CO ₂	Density Water	Viscosity CO ₂	Gravity Nr.
105.65	198.63	179.99	93.66	4.04E-05	0.94
52.90	96.04	167.97	83.35	4.20E-05	0.41
56.83	297.03	190.35	104.77	3.91E-05	0.55

Figure 19 is the first result of injection on the left side of the reservoir, 200 m above the magma source, with a permeability of 5 mD. The profile resembles the result from Figure 16, although the migration pattern shows more horizontal movement. This is confirmed by the calculated gravity numbers, supporting a more horizontal movement pattern. Another distinctive

difference compared to the high permeability cases is the isotherms showing fewer distortions caused by viscous flow channels. The distortion of the isotherms will be analyzed more closely in the Discussion section of the thesis.

3.4.2 Injection 400 m above the bottom reservoir boundary

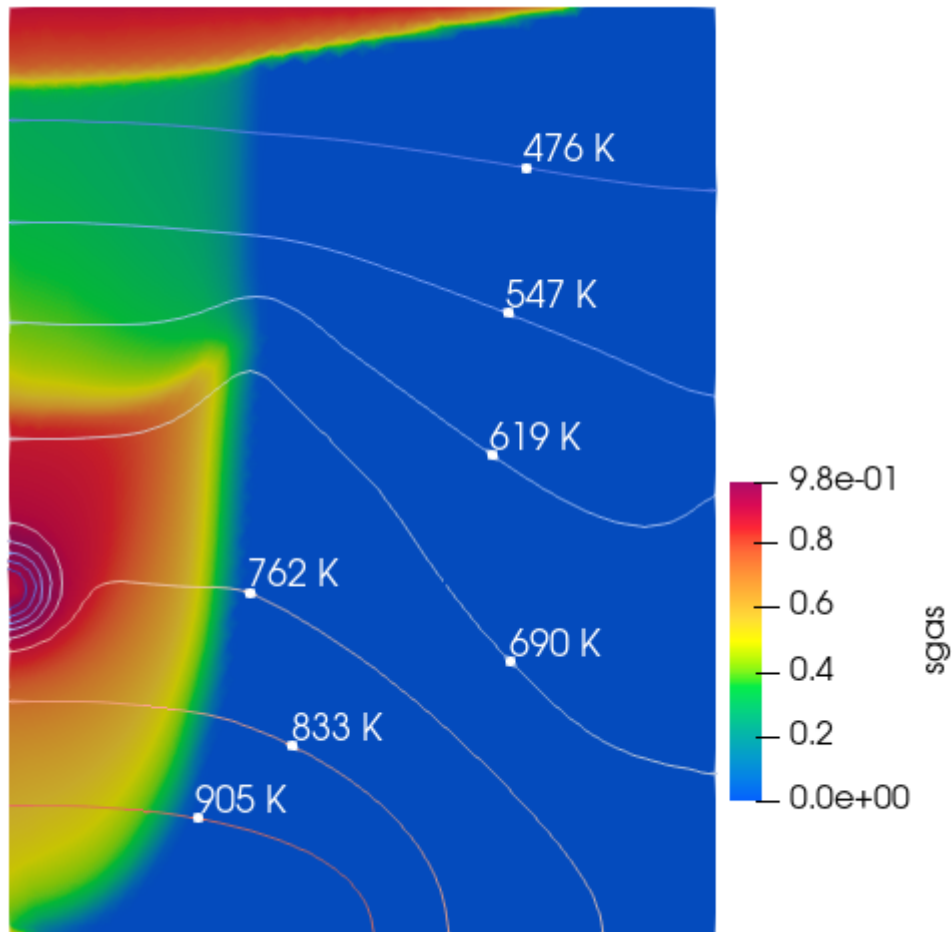


Figure 20 CO₂ injection for 30 years at $k=5$ mD and 400 m above the reservoir boundary

Table 14 Density of water and CO₂ [kg/m³], CO₂ viscosity [Pa·s] and gravity number for case above

x-coordinate	y-coordinate	Density CO ₂	Density Water	Viscosity CO ₂	Gravity Nr.
95.86	395.38	206.25	129.05	3.76E-05	0.94
50.96	297.55	192.04	106.75	3.90E-05	0.50
50.59	503.16	218.44	165.31	3.65E-05	0.37

Figure 20 yields the results for the injection on the left, 400 m above the magma source at 5 mD permeability. Opposed the injection at 10 mD at the same point, but in accordance with the previous case with 5 mD permeability, all the gravity numbers at the corresponding points are

smaller than 1, indicating more viscous forces and, therefore, horizontal displacement of the plume. As expected, due to a lower temperature, this case displays less sinking tendency than injection at the lower points in the reservoir.

3.4.3 Injection 525 m above the bottom reservoir boundary

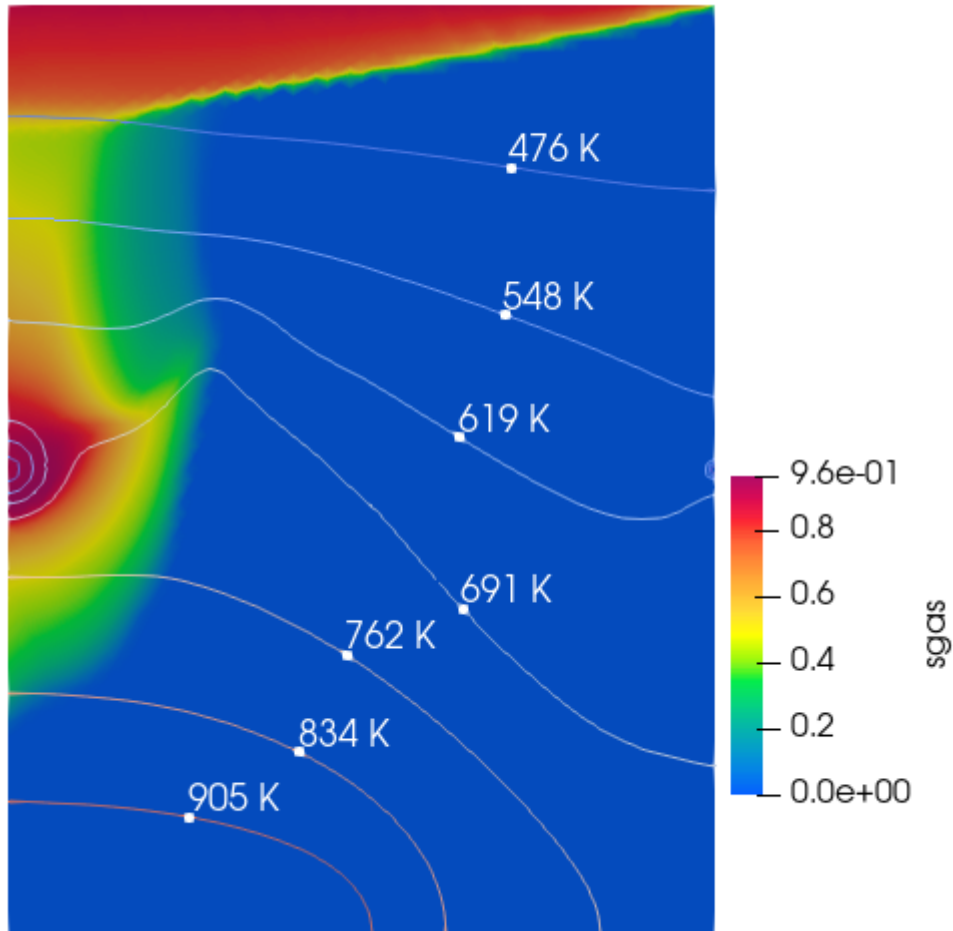


Figure 21 CO₂ injection for 30 years at $k=5$ mD and 525 m above the reservoir boundary

Table 15 Density of water and CO₂ [kg/m³], CO₂ viscosity [Pa·s] and gravity number for case above

x-coordinate	y-coordinate	Density CO ₂	Density Water	Viscosity CO ₂	Gravity Nr.
94.79	522.06	225.10	193.48	3.64E-05	0.43
51.76	421.28	209.47	133.90	3.75E-05	0.50
50.66	621.58	242.58	525.86	3.53E-05	2.28

Figure 21 shows the injection at 525 m and 5 mD permeability. There is a strong correlation with the case observed in Figure 3-8 and Table 12, exhibiting a significantly higher gravity

number for the point above the injection, along with water having a higher density than CO₂. This indicates consistency in the results and again serves to explain the upward movement of the CO₂ plume for the cases at this injection depth.

3.5 CO₂ Injection on the left side at 1 mD permeability

3.5.1 Injection 200 m above the bottom reservoir boundary

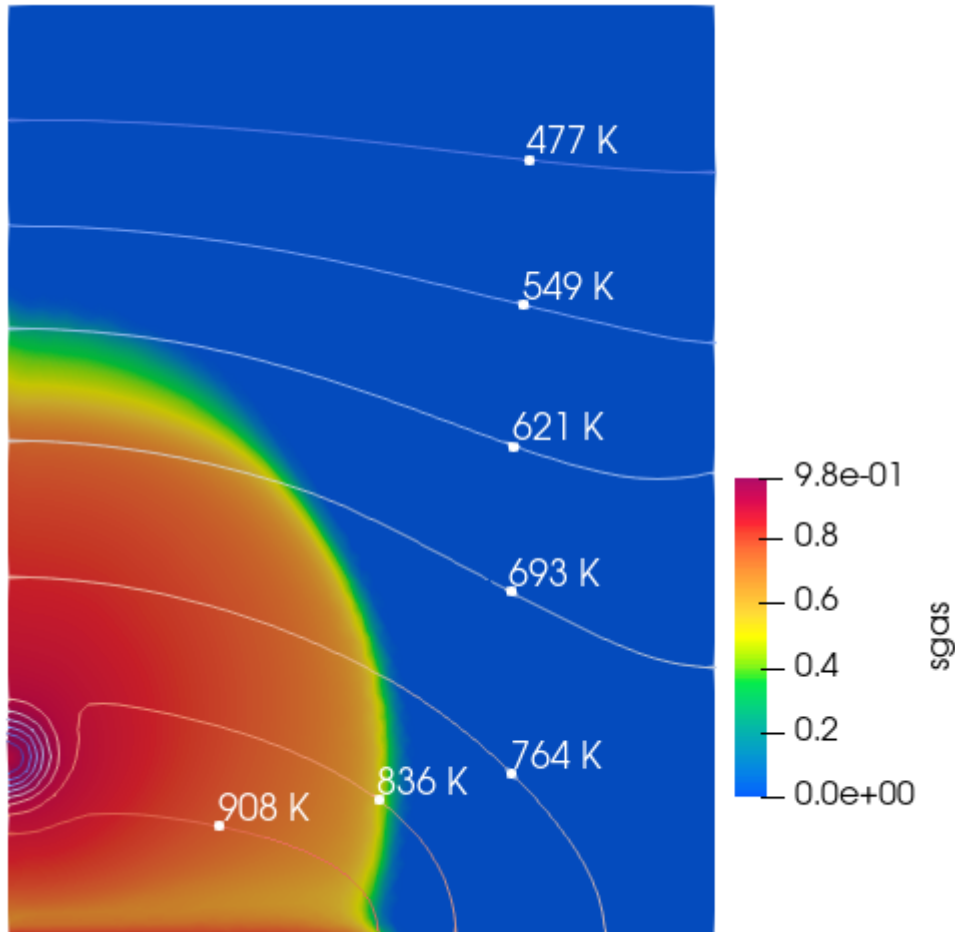


Figure 22 CO₂ injection for 30 years at $k=1$ mD and 200 m above the reservoir boundary

Table 16 Density of water and CO₂ [kg/m³], CO₂ viscosity [Pa·s] and gravity number for case above

x-coordinate	y-coordinate	Density CO ₂	Density Water	Viscosity CO ₂	Gravity Nr.
105.65	198.63	191.65	101.86	4.07E-05	0.21
52.90	96.04	178.64	89.93	4.23E-05	0.09
56.83	297.03	202.29	114.38	3.94E-05	0.12

Figure 22 is the first instance of injection on the left side with the lowest examined permeability at 1 mD and 200 m above the magma source. This result, confirmed by the calculated gravity numbers, shows a strong horizontal expansion of the plume. Another consistency observed by

decreasing the permeability is minimal displacement of the isotherms caused by viscous flow channels, as such small permeabilities do not promote channels to develop.

3.5.2 Injection 400 m above the bottom reservoir boundary

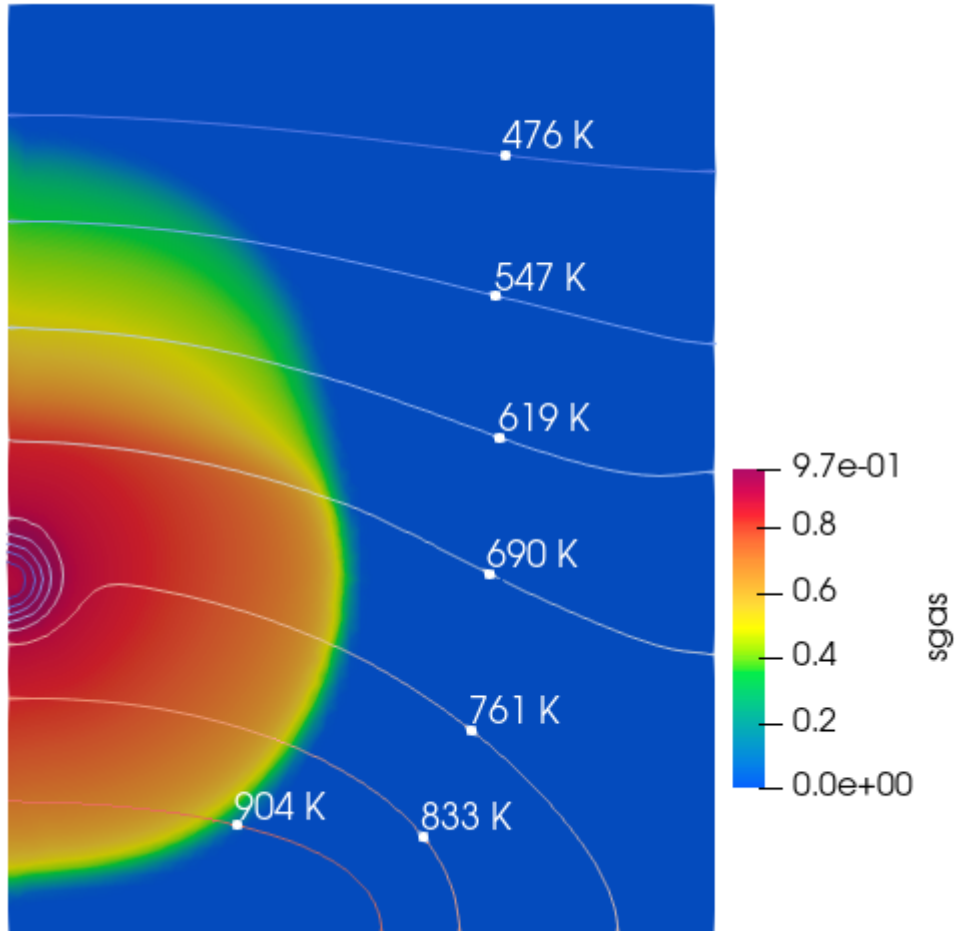


Figure 23 CO₂ injection for 30 years at $k=1$ mD and 400 m above the reservoir boundary

Table 17 Density of water and CO₂ [kg/m³], CO₂ viscosity [Pa·s] and gravity number for case above

x-coordinate	y-coordinate	Density CO ₂	Density Water	Viscosity CO ₂	Gravity Nr.
96.36	395.64	222.64	148.83	3.80E-05	0.19
49.99	295.92	205.77	117.89	3.94E-05	0.11
51.54	497.13	234.59	195.72	3.71E-05	0.06

Figure 23 confirms previous assumptions of the behavior to be expected by changing the permeability and depth of injection. Depicted is the injection at 1 mD, 400 m above the magma source. The low gravity numbers support the observed shape of the plume, consistent with the

constant temperature cases. In addition to the shape, the decreasing density difference at higher injection points can also be observed in the data in Table 17.

3.5.3 Injection 525 m above the bottom reservoir boundary

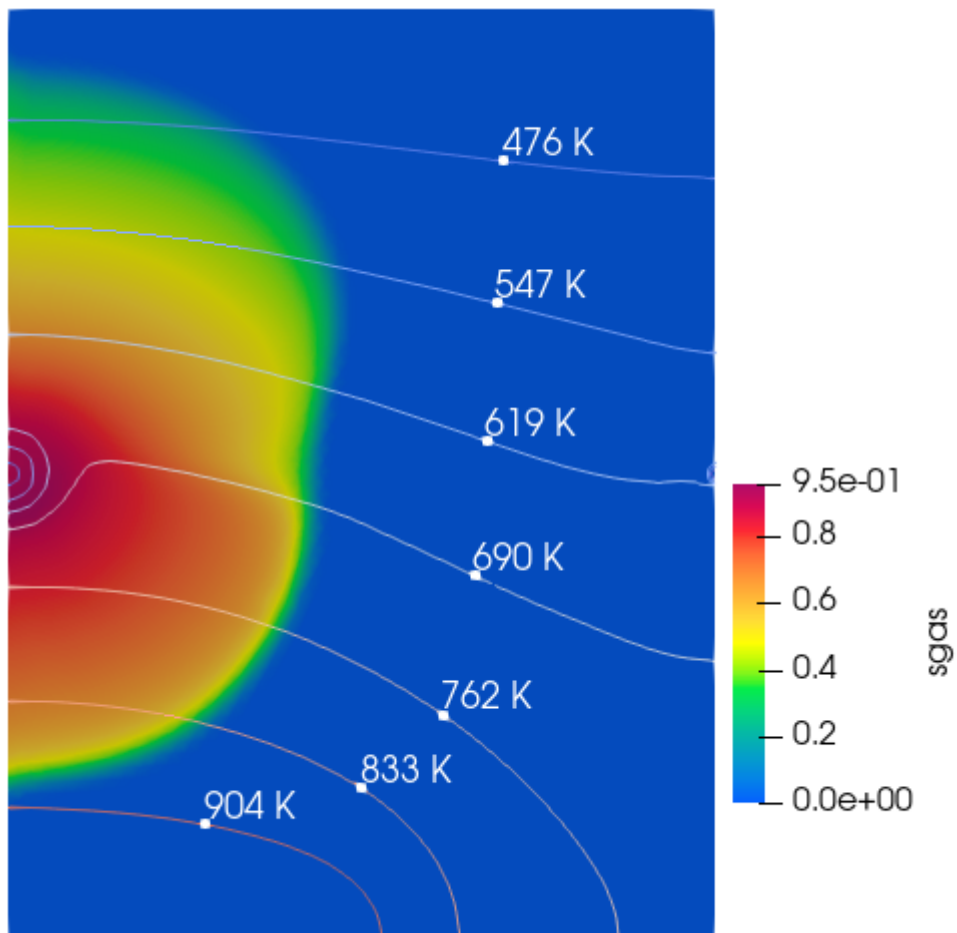


Figure 24 CO₂ injection for 30 years at $k=1$ mD and 525 m above the reservoir boundary

Table 18 Density of water and CO₂ [kg/m³], CO₂ viscosity [Pa·s] and gravity number for case above

x-coordinate	y-coordinate	Density CO ₂	Density Water	Viscosity CO ₂	Gravity Nr.
94.79	522.06	253.96	308.48	3.72E-05	0.16
51.76	421.28	234.57	166.94	3.83E-05	0.10
50.66	621.58	272.65	572.59	3.64E-05	0.53

Figure 24 and Table 18 present the last case of injection on the left side. As the previous examples have led one to predict, the injected CO₂ takes a bulb like shape, confirmed by the low gravity numbers. And as with the higher permeability cases, the gravity number is highest

for the point above the injection, as well as the density of water being roughly two times larger than that of CO₂.

3.6 CO₂ Injection on the right side at 10 mD permeability

3.6.1 Injection 200 m above the bottom reservoir boundary

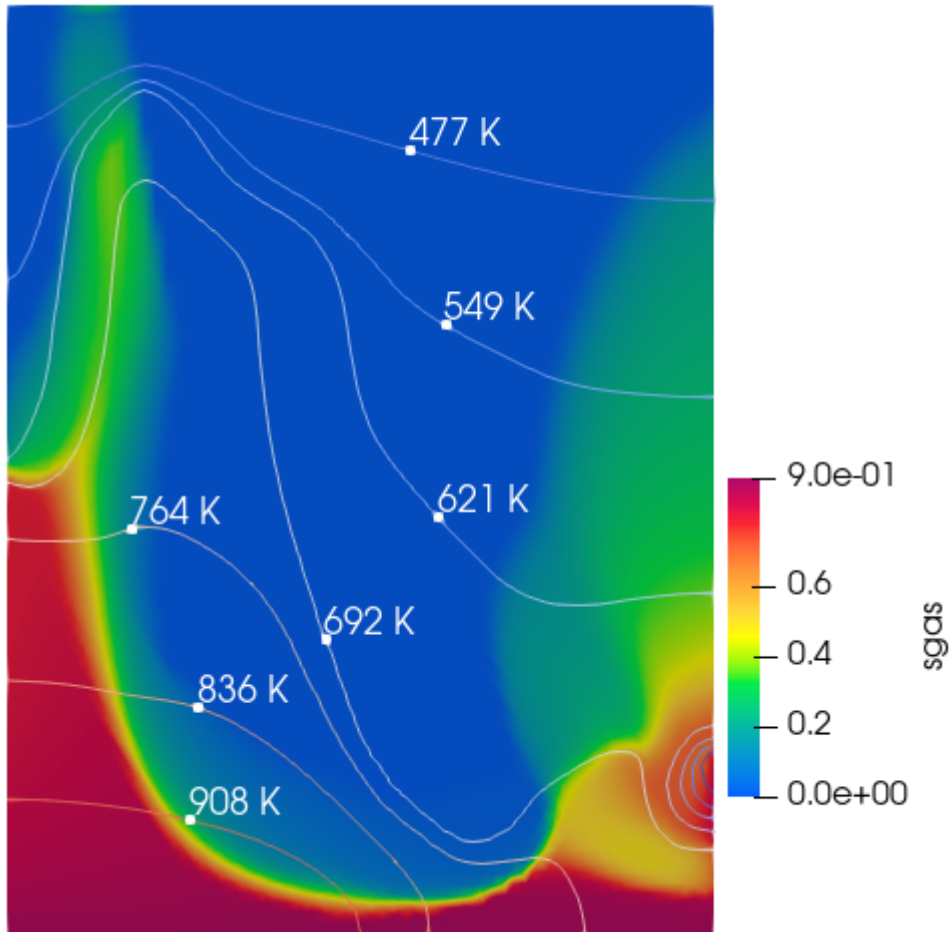


Figure 25 CO₂ injection on the right for 30 years at $k=10$ mD and 200 m above the reservoir boundary

Table 19 Density of water and CO₂ [kg/m³], CO₂ viscosity [Pa·s] and gravity number for case above

x-coordinate	y-coordinate	Density CO ₂	Density Water	Viscosity CO ₂	Gravity Nr.
704.93	201.82	236.77	253.98	3.65E-05	0.65
749.01	100.97	235.63	247.25	3.67E-05	0.23
748.29	302.13	254.84	570.34	3.55E-05	7.22

Figure 25 and Table 19 contain the first case of non-constant temperature CO₂ injection on the right side of the reservoir. As evidenced by the temperature profile in Figure 12, one may be expected to predict a different behavior of the injected CO₂. At a permeability of 10 mD and injection height of 200 m, the CO₂ shows a strong horizontal migration tendency, moving to

the magma source and migrating upward from there. Above the injection point, part of the injected CO₂ also migrates upwards. These observations are supported by the calculated gravity numbers, with the points to the left and below the injection being smaller than 1 and thus promoting horizontal movement, with the point above the injection having a value larger than 1 and exhibiting vertical migration. The isotherms also support the observation of the densities at the point above the injection. These suggest the temperature at this point to be between 621 K and 691 K, below the density difference transition zone documented by Parisio and Vilarrasa (2020). A clear difference compared to the cases with injection on the left side is the switching of the densities closer to the bottom reservoir boundary, at 300 m.

3.6.2 Injection 400 m above the bottom reservoir boundary

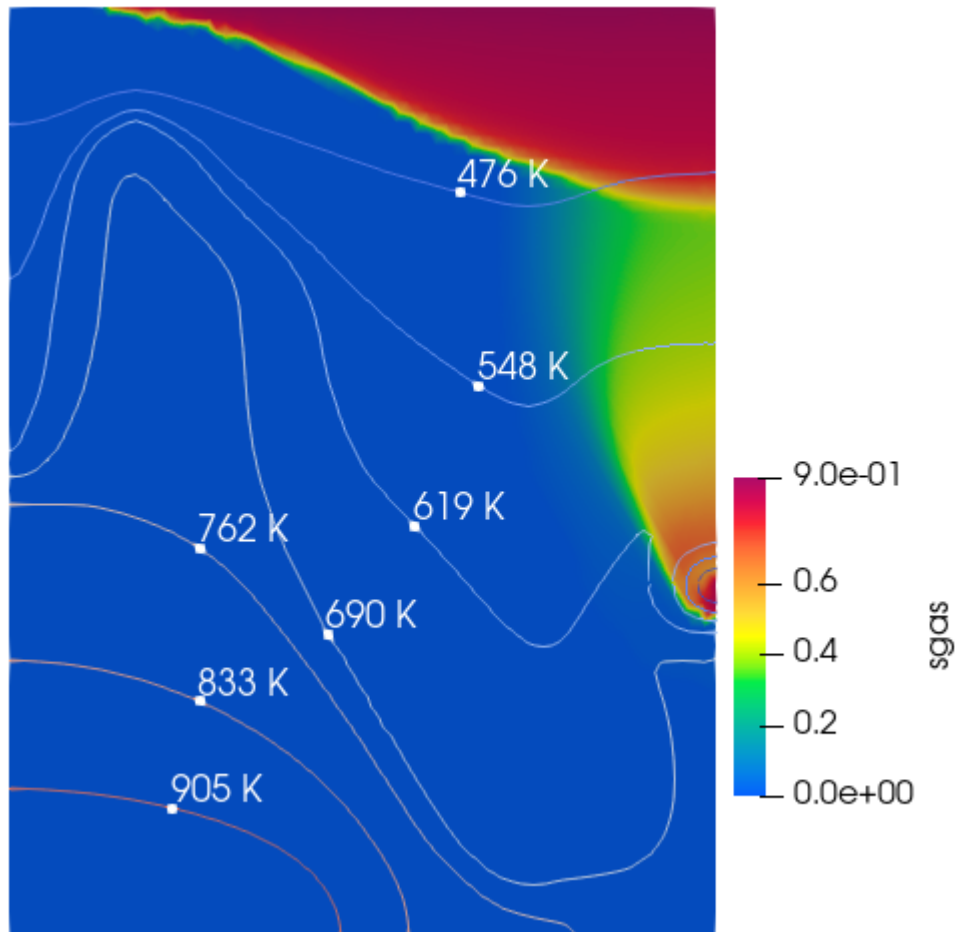


Figure 26 CO₂ injection on the right for 30 years at $k=10$ mD and 400 m above the reservoir boundary

Table 20 Density of water and CO₂ [kg/m³], CO₂ viscosity [Pa·s] and gravity number for case above

x-coordinate	y-coordinate	Density CO ₂	Density Water	Viscosity CO ₂	Gravity Nr.
703.70	395.72	258.33	633.86	3.49E-05	16.50
748.41	301.57	232.04	241.23	3.62E-05	0.19
748.67	497.06	263.24	675.34	3.45E-05	9.96

Figure 26 and Table 20 present the case of injection on the right side at 400 m and a permeability of 10 mD. There is a strong upward trend of the injected CO₂, supported by the densities and calculated gravity numbers in Table 20. Both points to the left of the injection and above the injection are high, in accordance with the witnessed behavior of the plume shape. The point below the injection exhibits a low gravity number and density difference, but there is very little CO₂ at this point. This is also the first case in which the density of water is higher than CO₂ at all analyzed points.

3.6.3 Injection 525 m above the bottom reservoir boundary

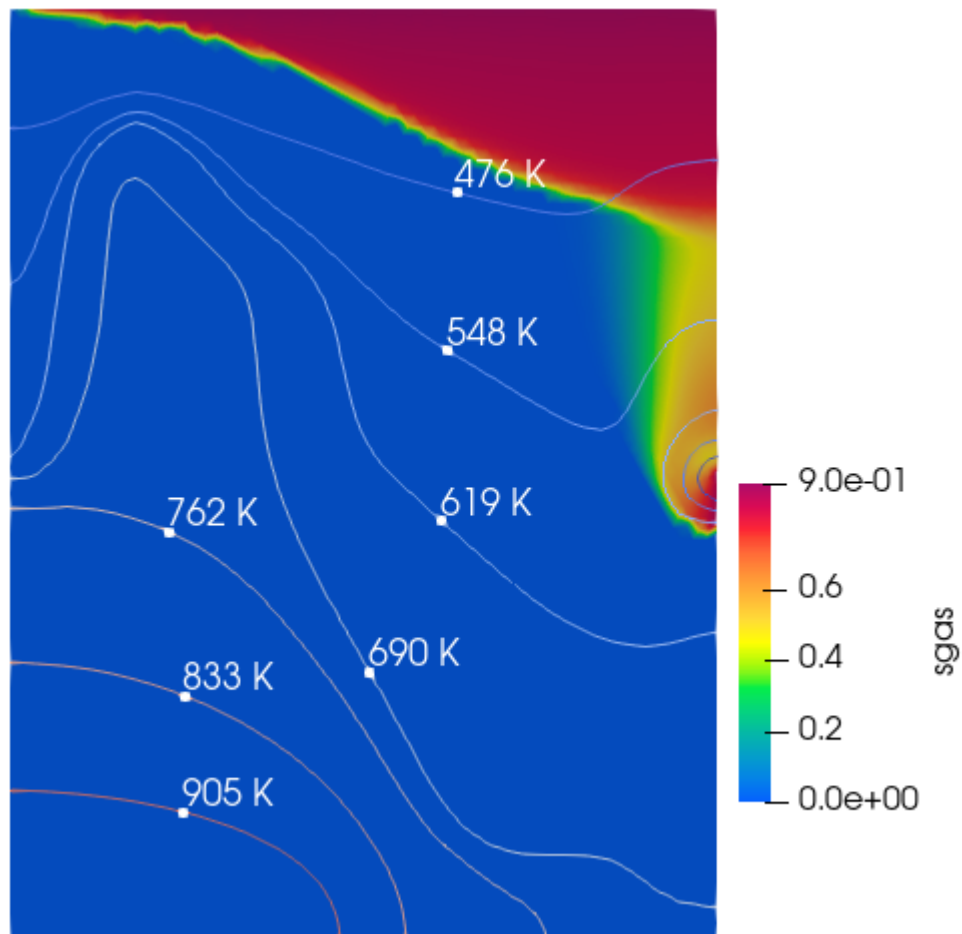


Figure 27 CO₂ injection on the right for 30 years at $k=10$ mD and 525 m above the reservoir boundary

Table 21 Density of water and CO₂ [kg/m³], CO₂ viscosity [Pa·s] and gravity number for case above

x-coordinate	y-coordinate	Density CO ₂	Density Water	Viscosity CO ₂	Gravity Nr.
705.38	521.96	293.12	767.26	3.40E-05	23.87
748.27	421.23	278.71	719.68	3.44E-05	11.40
749.81	621.59	288.03	766.94	3.37E-05	12.66

Figure 27 reaffirms the trends witnessed in the previous examples of amplification of the previous behavior when either the permeability or the injection depth is changed. In this case there is a very clear upward trend, confirmed by the calculated gravity numbers and densities. Opposed to Table 20, in which the density and gravity number of the sample point below the injection was an outlier, here uniformity confirming the witnessed trend is readily apparent.

3.7 CO₂ Injection on the right side at 5 mD permeability

3.7.1 Injection 200 m above the bottom reservoir boundary

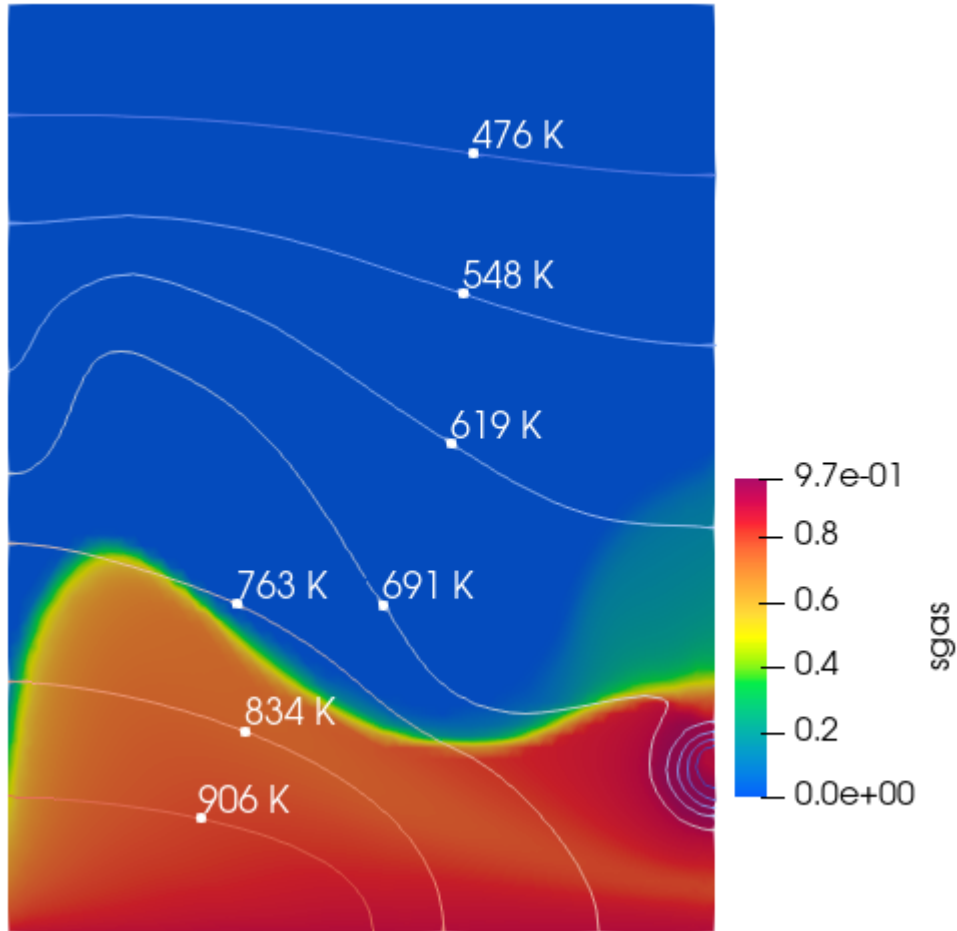


Figure 28 CO₂ injection on the right for 30 years at $k=5$ mD and 200 m above the reservoir boundary

Table 22 Density of water and CO₂ [kg/m^3], CO₂ viscosity [$\text{Pa}\cdot\text{s}$] and gravity number for case above

x-coordinate	y-coordinate	Density CO ₂	Density Water	Viscosity CO ₂	Gravity Nr.
704.93	201.82	225.64	180.21	3.68E-05	0.61
749.01	100.97	219.56	153.48	3.73E-05	0.46
748.29	302.13	239.43	377.75	3.59E-05	1.10

Figure 28 shows the result of injection on the right side, 200 m above the bottom reservoir boundary at a permeability of 5 mD. The result resembles a less amplified version of those witnessed in Figure 25 at 10 mD, and the gravity numbers calculated in Table 22 resemble the pattern observed in Table 19. The gravity numbers to the left and below the injection promote

horizontal movement and the one above vertical movement. This vertical movement is less amplified than in the higher permeability scenario since the density difference is smaller.

3.7.2 Injection 400 m above the bottom reservoir boundary

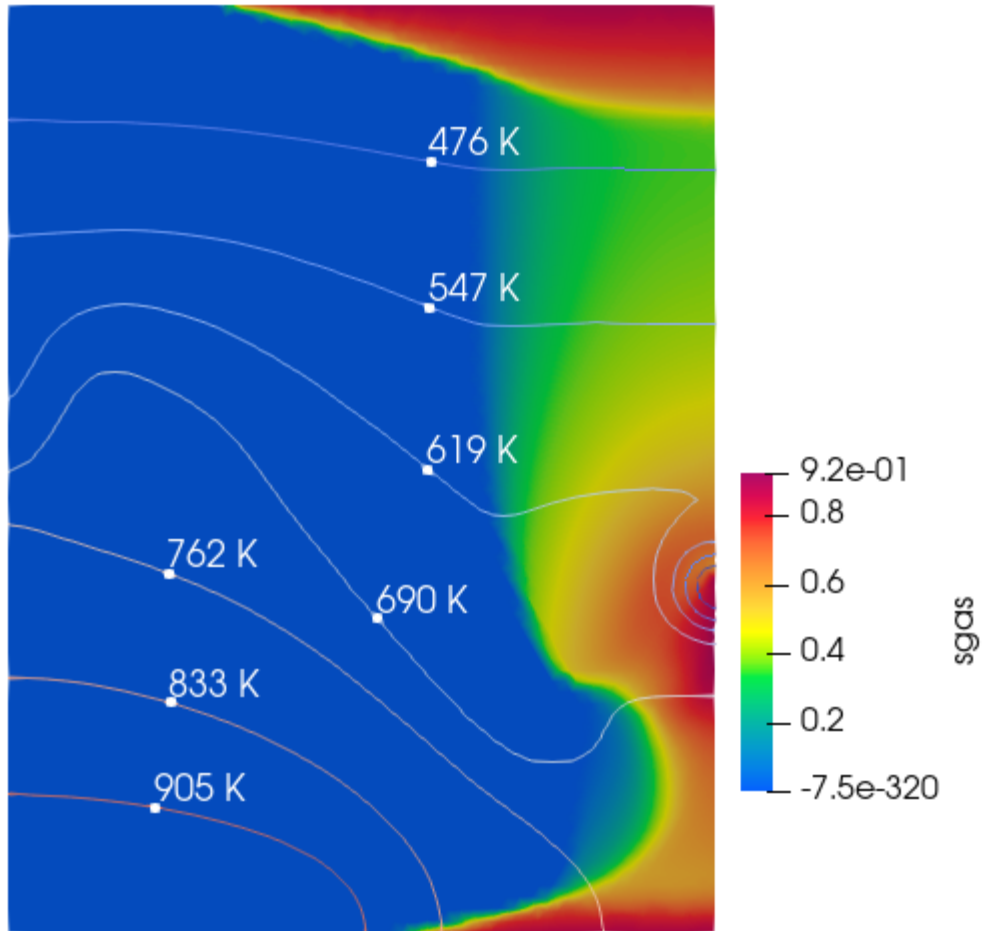


Figure 29 CO₂ injection on the right for 30 years at $k=5$ mD and 400 m above the reservoir boundary

Table 23 Density of water and CO₂ [kg/m³], CO₂ viscosity [Pa·s] and gravity number for case above

x-coordinate	y-coordinate	Density CO ₂	Density Water	Viscosity CO ₂	Gravity Nr.
703.70	395.72	251.63	575.12	3.53E-05	5.13
748.41	301.57	240.02	382.26	3.59E-05	1.13
748.67	497.06	262.08	655.67	3.48E-05	3.52

Figure 29 details the injection on the right side, at 5 mD and 400 m above the bottom reservoir boundary. Table 23 shows, as with the 10 mD case, the water density to be higher at all three selected points and the gravity numbers support more horizontal movement of the injected CO₂,

as is also evidenced by Figure 29. Compared to the 10 mD case however, this case also supports some sinking of the CO₂.

3.7.3 Injection 525 m above the bottom reservoir boundary

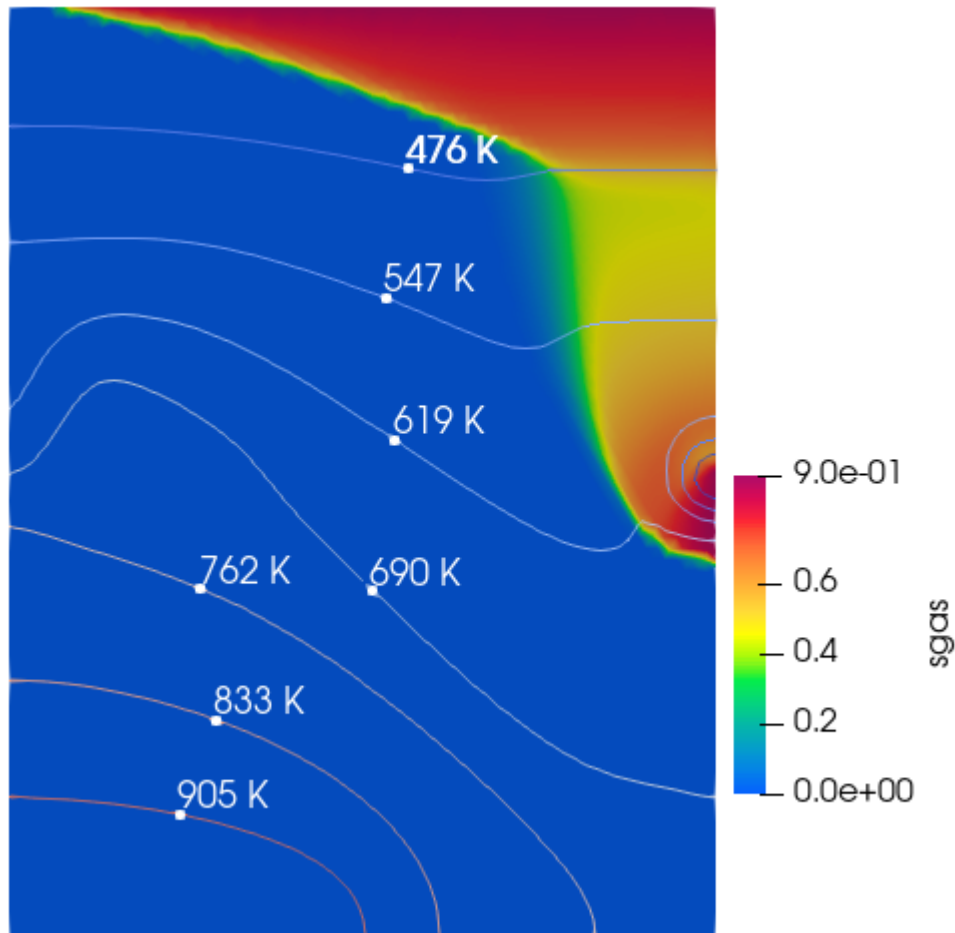


Figure 30 CO₂ injection on the right for 30 years at $k=5$ mD and 525 m above the reservoir boundary

Table 24 Density of water and CO₂ [kg/m³], CO₂ viscosity [Pa·s] and gravity number for case above

x-coordinate	y-coordinate	Density CO ₂	Density Water	Viscosity CO ₂	Gravity Nr.
705.38	521.96	269.51	695.09	3.44E-05	7.29
748.27	421.23	255.26	615.25	3.50E-05	3.14
749.81	621.59	283.45	748.26	3.39E-05	4.50

Figure 30 shows the injection at 5 mD and 525 m above the bottom of the reservoir. The figure shows exclusively an upward migration of the injected CO₂. This observed behavior is confirmed in Table 24 by the densities of water, being more than twice as large as those of CO₂

in all three selected points, as well as all the calculated gravity numbers promoting vertical movement.

3.8 CO₂ Injection on the right side at 1 mD permeability

3.8.1 Injection 200 m above the bottom reservoir boundary

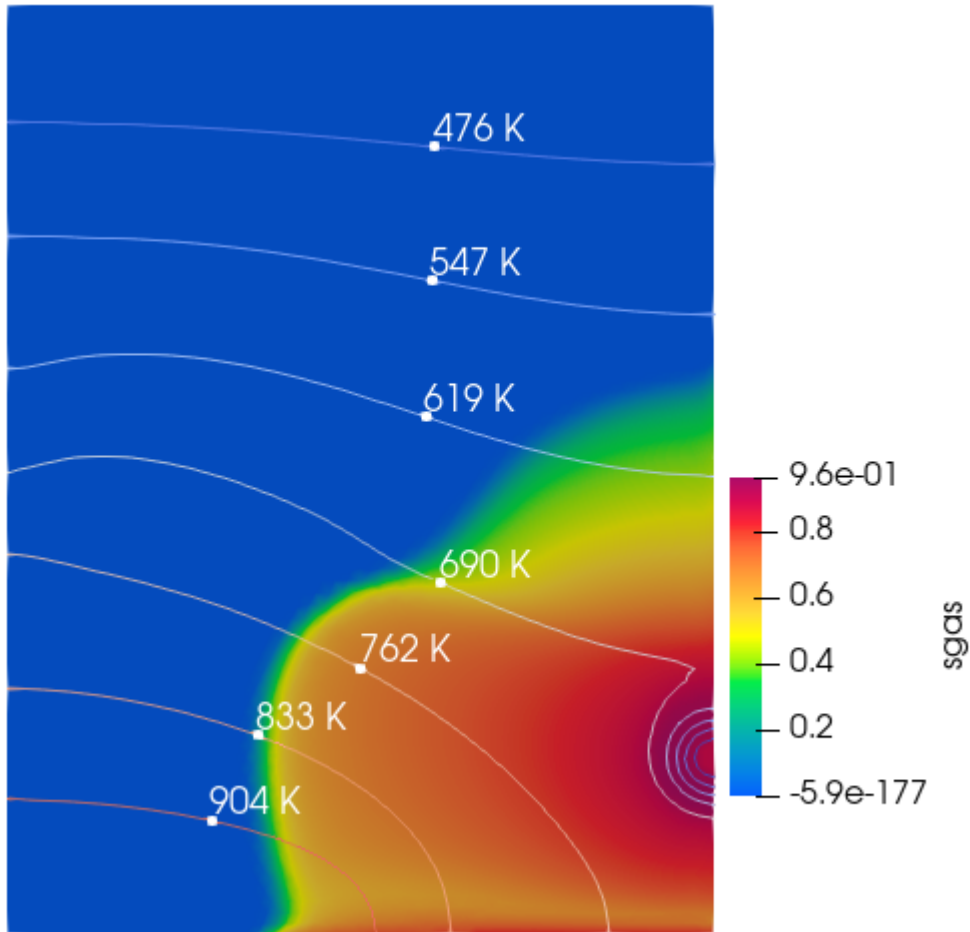


Figure 31 CO₂ injection on the right for 30 years at $k=1$ mD and 200 m above the reservoir boundary

Table 25 Density of water and CO₂ [kg/m³], CO₂ viscosity [Pa·s] and gravity number for case above

x-coordinate	y-coordinate	Density CO ₂	Density Water	Viscosity CO ₂	Gravity Nr.
704.93	201.82	239.51	206.24	3.74E-05	0.09
749.01	100.97	231.96	166.91	3.79E-05	0.09
748.29	302.13	247.35	299.76	3.68E-05	0.08

Figure 31 describes the injection at 1 mD, the lowest examined permeability, 200 m above the bottom reservoir boundary. As with previous cases at this permeability, the injected CO₂ takes a bulb-like shape, confirmed by the calculated gravity numbers in Table 25. All gravity numbers are well below 1, confirming the viscous dominated behavior. As with the 5 mD case and

injection on the right side, the density of water is smaller than that of CO₂ in the points to the left and below the injection and larger above the injection. But due to the low permeability and gravity numbers, the buoyancy effects are less severe.

3.8.2 Injection 400 m above the bottom reservoir boundary

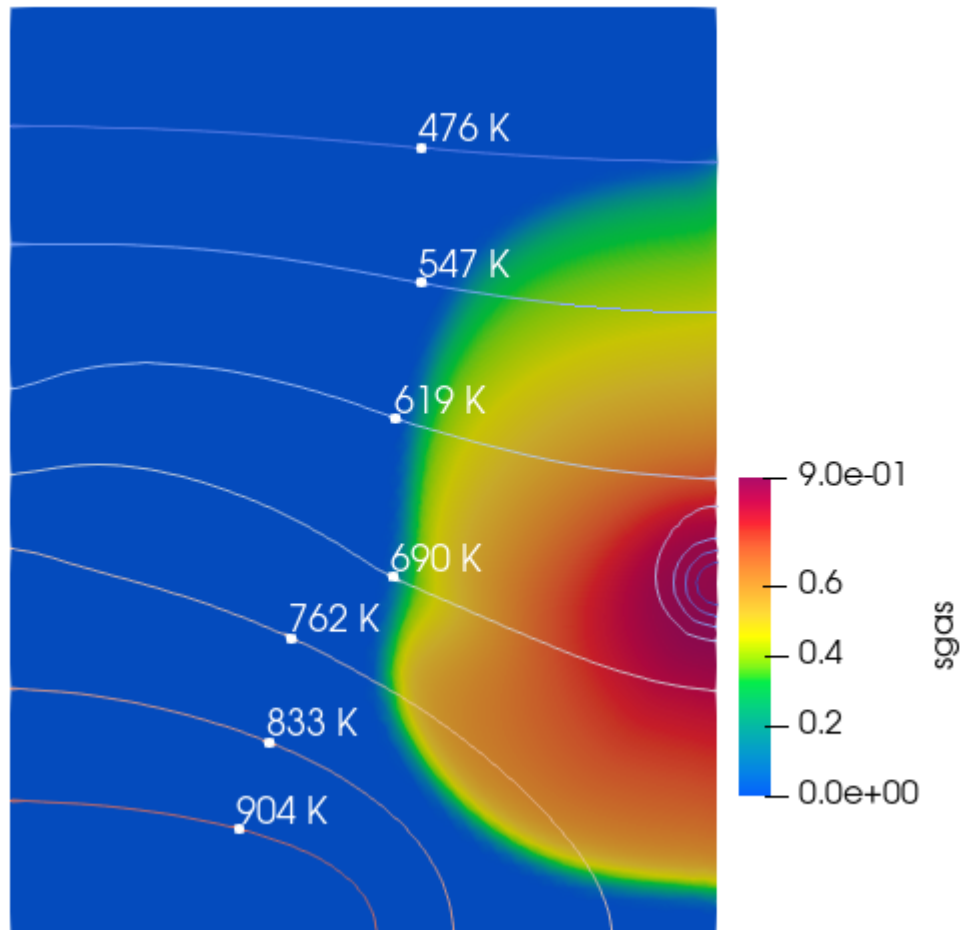


Figure 32 CO₂ injection on the right for 30 years at $k=1$ mD and 400 m above the reservoir boundary

Table 26 Density of water and CO₂ [kg/m³], CO₂ viscosity [Pa·s] and gravity number for case above

x-coordinate	y-coordinate	Density CO ₂	Density Water	Viscosity CO ₂	Gravity Nr.
703.70	395.72	266.91	561.32	3.62E-05	0.97
748.41	301.57	254.23	386.48	3.67E-05	0.22
748.67	497.06	279.68	650.44	3.57E-05	0.69

Figure 32 describes the injection 400 m above the bottom reservoir boundary at 1 mD. As with previous low permeability cases, the horizontal movement of the injected CO₂ dominates,

confirmed by the gravity numbers in Table 26. The density of water is higher than the density of CO₂ in all three selected points.

3.8.3 Injection 525 m above the bottom reservoir boundary

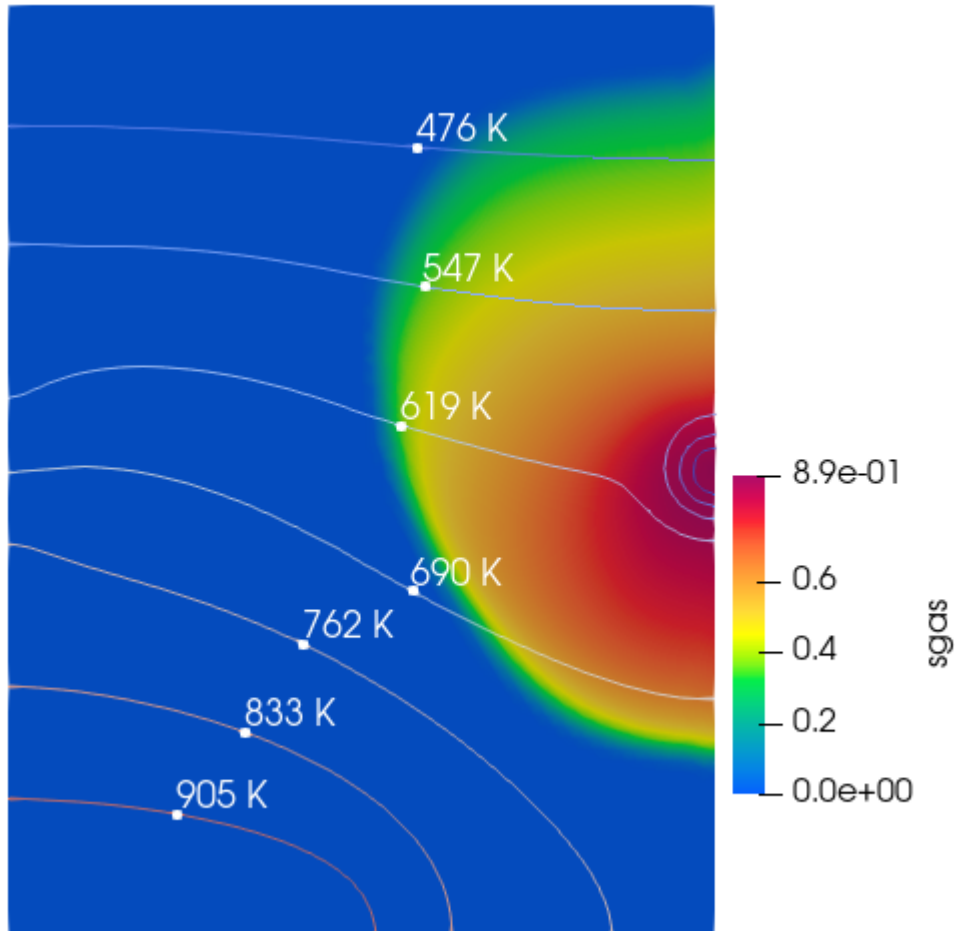


Figure 33 CO₂ injection on the right for 30 years at $k=1$ mD and 525 m above the reservoir boundary

Table 27 Density of water and CO₂ [kg/m³], CO₂ viscosity [Pa·s] and gravity number for case above

x-coordinate	y-coordinate	Density CO ₂	Density Water	Viscosity CO ₂	Gravity Nr.
705.38	521.96	293.75	690.29	3.57E-05	1.43
748.27	421.23	274.12	595.32	3.62E-05	0.58
749.81	621.59	311.46	747.40	3.54E-05	0.89

Figure 33 describes the last case of CO₂ injection analyzed in this thesis, at 1 mD and 525 m above the bottom reservoir boundary. The results are consistent with what was observed in the previous cases, the only exception being the gravity number of the point to the left of the

injection in Table 27, suggesting more vertical movement of the CO₂ plume. Nonetheless, the results of Figure 33 still support the results and expectations from the previous analysis.

3.9 Pressure Profiles at the Injection Point

3.9.1 Injection Depth of 200 m

Along with the CO₂ saturation profiles, the pressures at the injection points are also of interest due to concerns about the formation integrity.

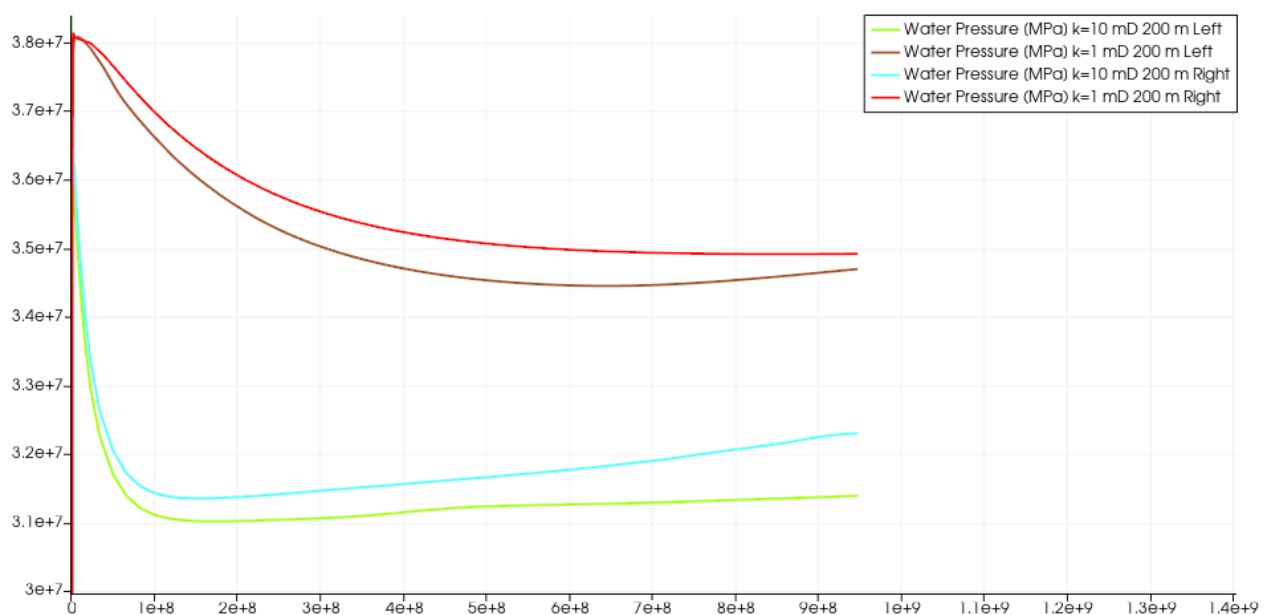


Figure 34 Pressure profiles [MPa] over 30 years at injection points 200 m above the bottom reservoir boundary for 1 mD and 10 mD permeability

Figure 34 shows the pressure profiles of four selected injection points at 200 m above the bottom of the reservoir for both left and right injection at 1 mD and 10 mD permeability.

When injection starts, the pressure rises to around 38 MPa in both 1 mD cases, before slowly plateauing to a pressure of around 35 MPa. After 30 years, the left injection has a pressure of 34.7 MPa and the right injection has a pressure of 34.9 MPa. The profile for the injection on the left and right side is very similar, with the right side showing a slightly higher final pressure. In contrast to the right side, the left side has the lowest pressure at about 20 years and then rises again very slowly.

As expected, the 10 mD cases have a lower pressure than the low permeability cases. After the first injection, the pressure increases to about 36 MPa, 2 MPa lower than the 1 mD cases. The subsequent pressure drop is much faster before the plateau is reached. Contrary to the low permeability case, here the injection on the right side shows a higher pressure increase throughout the plateauing phase. However, as in the low permeability case, the injection on the right has the higher final pressure of 32.3 MPa compared to 31.4 MPa on the left.

3.9.2 Injection Depth of 525 m

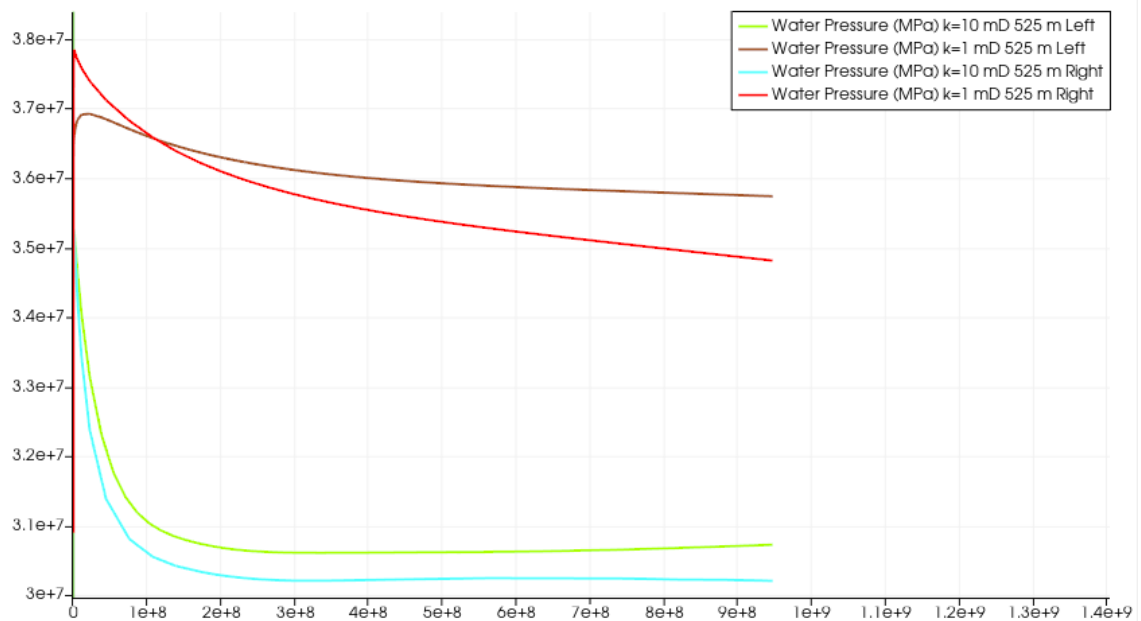


Figure 35 Pressure profiles [MPa] over 30 years at injection points 525 m above the bottom reservoir boundary for 1 mD and 10 mD permeability

Figure 35 shows the pressure profiles of four selected injection points at 525 m above the bottom of the reservoir for both left and right injection at 1 mD and 10 mD permeability.

In the 1 mD cases the pressure initially rises to slightly lower values than for the injection points at 200 m, about 37 MPa for the left side and about 37.5 MPa for the right side. In contrast to the cases shown in Figure 3-24, the pressure profiles cross after 3 years of injection, and the final pressure of the injection on the right is lower at 34.8 MPa and also declining, than the final pressure of 35.7 MPa for the injection on the left, which shows a more plateau-like behavior.

The 10 mD cases reach a pressure of 35 MPa before plateauing after 6 years of injection. As with the lower injection cases, the initial pressure drops very quickly and the left- and right-side profiles look almost identical. After 30 years, the left injection point has a pressure of 30.7 MPa and the right injection point has a pressure of 30.2 MPa. As with the low permeability cases at this depth, but in contrast to the lower injection point, the final pressure of the right side is higher.

Chapter 4

Discussion

4.1 CO₂ Plume Behavior

The results of the thesis show a somewhat consistent behavior of the injected CO₂ into the different reservoir configurations. The results of injection into a constant temperature reservoir in Figures 13, 14 and 15 confirm previous assumptions of Parisio and Vilarrasa (2020) and Probst (2023) that CO₂ does indeed sink towards the bottom of the reservoir at high enough temperature. These results also confirm the strong influence of permeability on the shape of the plume and the sinking behavior, confirmed by the calculated gravity numbers.

Injections into distributed temperature reservoirs, the main focus of this thesis, produced less consistent results. One consistency in these cases is the increase of the viscous dominated behavior at lower permeabilities, with the CO₂ moving more horizontally and taking more of a uniform bell shape. This behavior is observed in the cases with 5 mD permeability and amplified in the 1 mD permeability cases. As previously demonstrated by Parisio and Vilarrasa (2020) and Probst (2023) the gravity numbers work well for injections into constant temperature reservoirs. This study demonstrates that the gravity numbers in terms of sinking potential in reservoirs with temperature gradients are less reliable, although there are some correlations in terms of more vertical or horizontal movement. Of the 21 gravity numbers calculated for the 1 mD case, 20 were below 1, thus indicating more viscous dominated horizontal migration. Of the 21 gravity numbers calculated for the 5mD cases, 13 were below 1 and 8 above 1, indicating more of a balance, but with a higher tendency of viscous dominated behavior. And the high permeability, 10 mD, cases, exhibited a clear tendency of buoyancy dominated behavior. Of the 21 gravity numbers, 18 are higher than 1 and 3 are lower than one, confirming the witnessed vertical, buoyancy dominated behavior of the corresponding figures.

Although the gravity numbers and the vertical or horizontal movement of the injected CO₂ are consistent with what was expected from previous analysis, the sinking tendencies observed do not match the expectations for all cases.

To compare and understand some of this unexpected behavior, the bulk movement in some cases of interest will be examined.

The first two cases compared are the injection at 10 mD, 200 m above the reservoir boundary at the left and the right side, as those exhibited vastly different behaviors. The investigated timesteps will be at one year, 15 years and 30 years, to see where differences might arise.

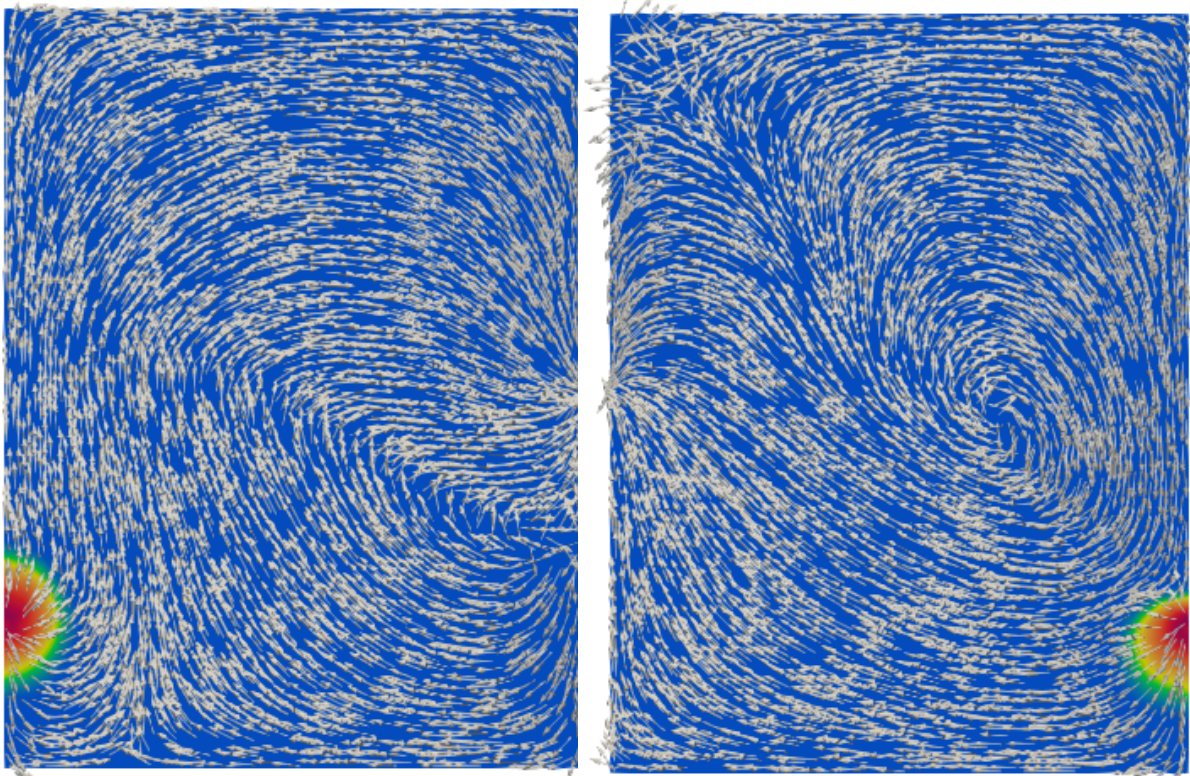


Figure 36 Injection on the left at 10 mD after 1 year *Figure 37 Injection on the right at 10 mD after 1 year*

Figure 36 details the bulk velocity for injection at 10 mD, 200 m above the bottom reservoir boundary on the left side after 1 year, and Figure 37 details the same for injection on the right side.

After one year in Figure 36, there is bulk movement in all directions from the injection point, but a clear upward trend can be witnessed outside of the formed CO₂ plume. This movement appears to converge towards the production well on the far right of the reservoir. Although the Dirichlet Boundary Condition simulating the magma source has been deactivated in the CO₂ injection cases, the upwards bulk movement seems to emanate from the center of the heat source.

In Figure 37 there is also bulk movement in all directions emanating from the injection point, although this trend quickly changes to movement downwards and to the left, which is in accordance to the witnessed behavior of the CO₂ plume. Rather unexpectedly, there is no distinct upward movement witnessed above the center of the heat source, as was the case with the injection on the left side.

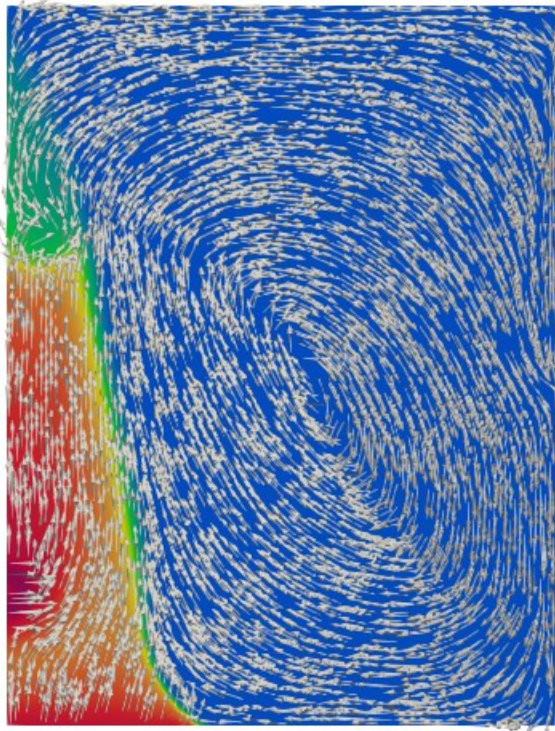


Figure 38 Injection on the left at 10 mD after 15 years

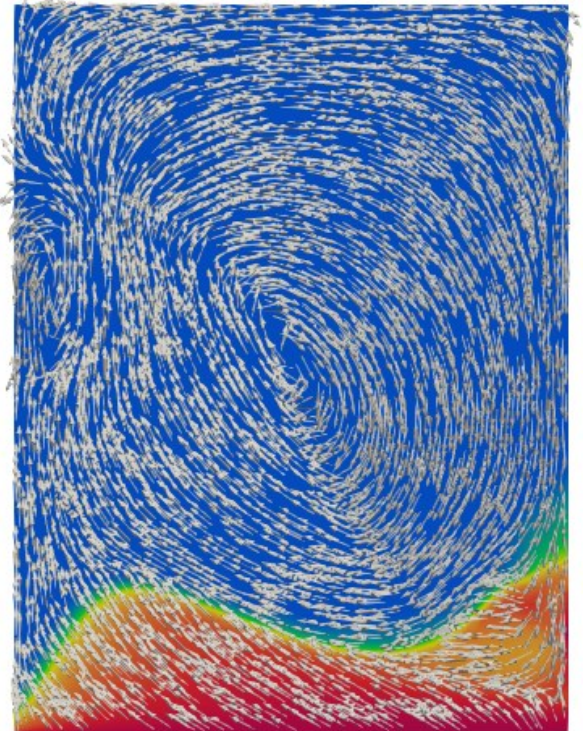


Figure 39 Injection on the right at 10 mD after 15 years

Figure 38 and Figure 39 show the evolution described in Figures 36 and 37 after 15 years of CO₂ injection. In Figure 38 the very clear upward trend continues, leading to a column of CO₂ being formed. Although some of the injected CO₂ has migrated to the bottom of the reservoir, the movement in the entire column is pointed upwards. The bulk movement towards the top of the reservoir emanating from the middle of the heat source is less visible in this case, as the entire column of CO₂ exhibits this behavior. In the middle of the reservoir, movement resembling that of a convection cell has started to form.

Figure 39 shows a continuation of the previously analyzed behavior of sinking and migration towards the left reservoir boundary. The CO₂ which has reached the bottom of the boundary experiences movement upwards and to the left, this is consistent with the behavior of a no-flow boundary. As with Figure 38, bulk movement resembling a convection cell has formed in the middle of the reservoir.

The witnessed behavior of the injected CO₂ is consistent with the bulk movement observed in both cases.

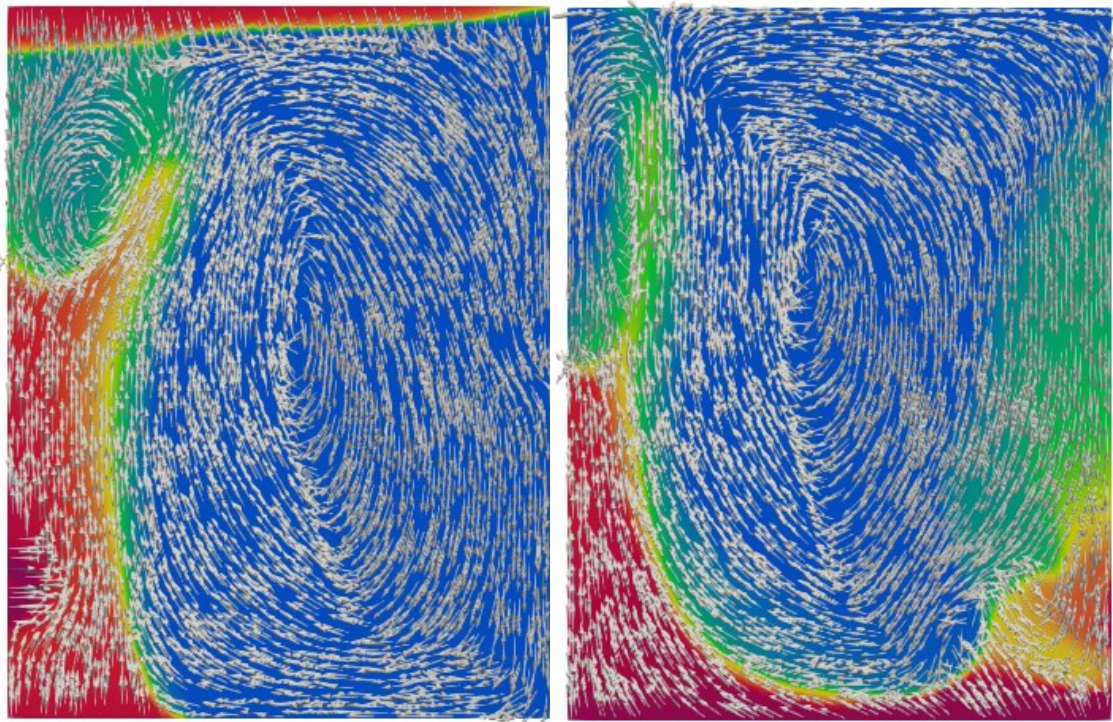


Figure 40 Injection on the left at 10 mD after 30 years *Figure 41 Injection on the right at 10 mD after 30 years*

Figures 40 and 41 depict the last timestep of the previously examined cases.

In Figure 40 the previously observed behavior continues, along with the horizontal movement in the near wellbore region. This is consistent with the observation from Parisio and Vilarrasa (2020) of viscous dominated behavior in the near wellbore region. The injected CO₂ has migrated to the top of the reservoir, where downward movement, caused by the no-flow boundary condition occurs. At the top of the CO₂ column a flow channel has formed on the right side, roughly aligned with the center of the magma source observed in Figure 36. To the left of this flow channel another convection like cell has formed.

Figure 41 details the shape of the CO₂ plume and the bulk movement for injection on the right. As with the injection on the left, once the injected CO₂ reaches the left boundary it starts to form a column, with a flow channel to the top right, with a similar convection like cell forming to the left of the channel.

These results and comparisons lead to the hypothesis that the temperature introduced by the magma source causes the injected CO₂ to migrate towards the top boundary of the reservoir. To examine this hypothesis, the temperature and viscosity profiles will be investigated.

The temperature profile at time zero is the same for both cases and has been presented in Chapter 3.2, and the viscosity profile at time zero is also the same for both cases and will be presented here.

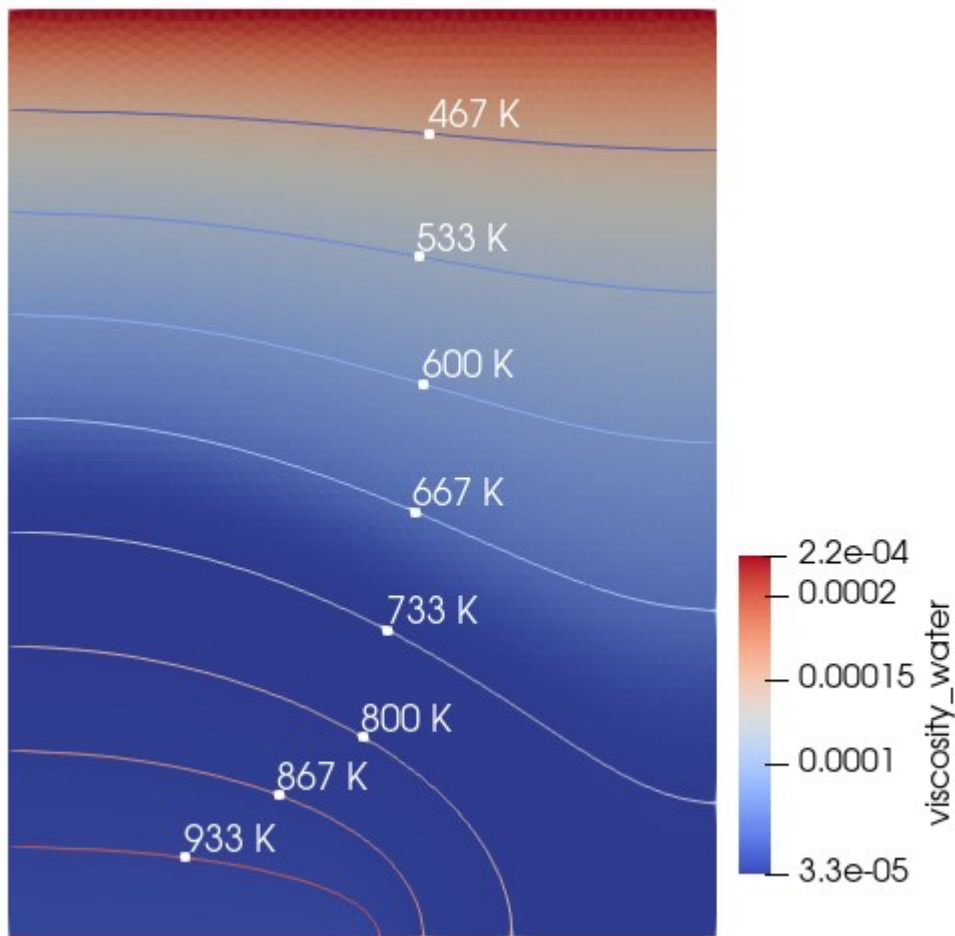


Figure 42 Water viscosity profile [Pa·s] at time zero

Figure 42 details the viscosity of the water in Pa·s at timestep zero. As expected, the viscosity follows the temperature profile, exhibiting the lowest values of 3.3×10^{-5} Pa·s in the hottest regions and the highest viscosities of 2.2×10^{-4} Pa·s in the coldest region of the reservoir. The temperature influence on the viscosity is strong, and analysis by Liu et al. (2012) on the temperature and pressure influence on supercritical fluids confirm that the pressure effect on the viscosity for the pressure variations in the examined cases can be neglected.

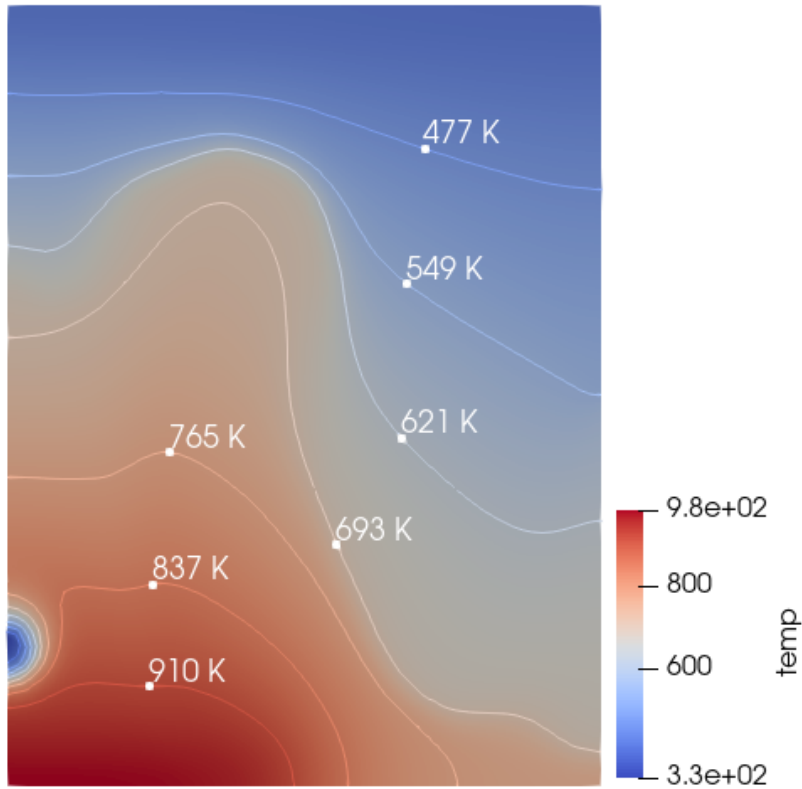


Figure 43 Temperature profile [K] of injection on the left side at 10 mD after 30 years

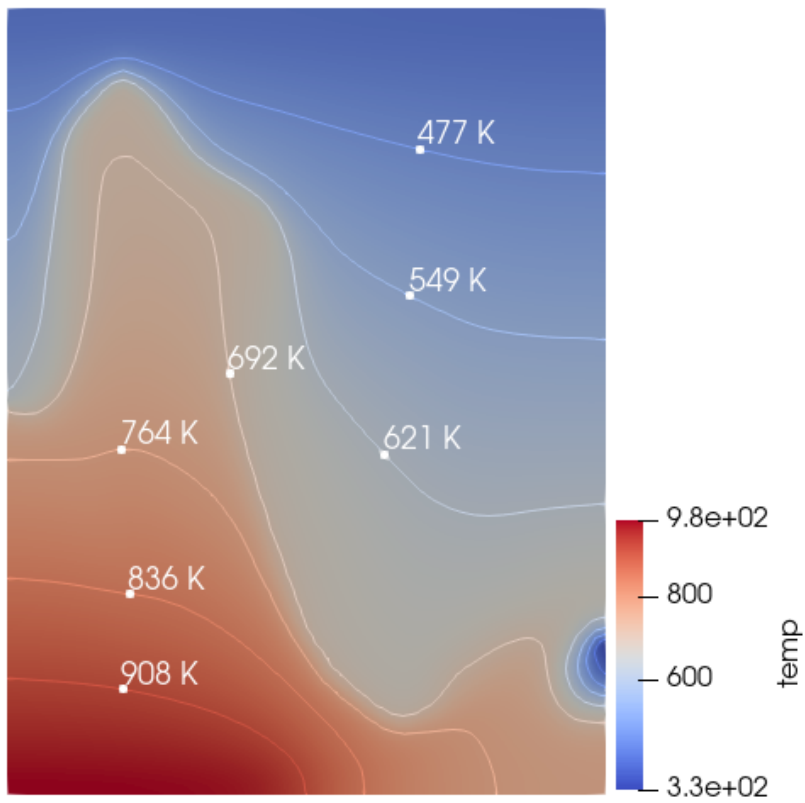


Figure 44 Temperature profile [K] of injection on the right side at 10 mD after 30 years

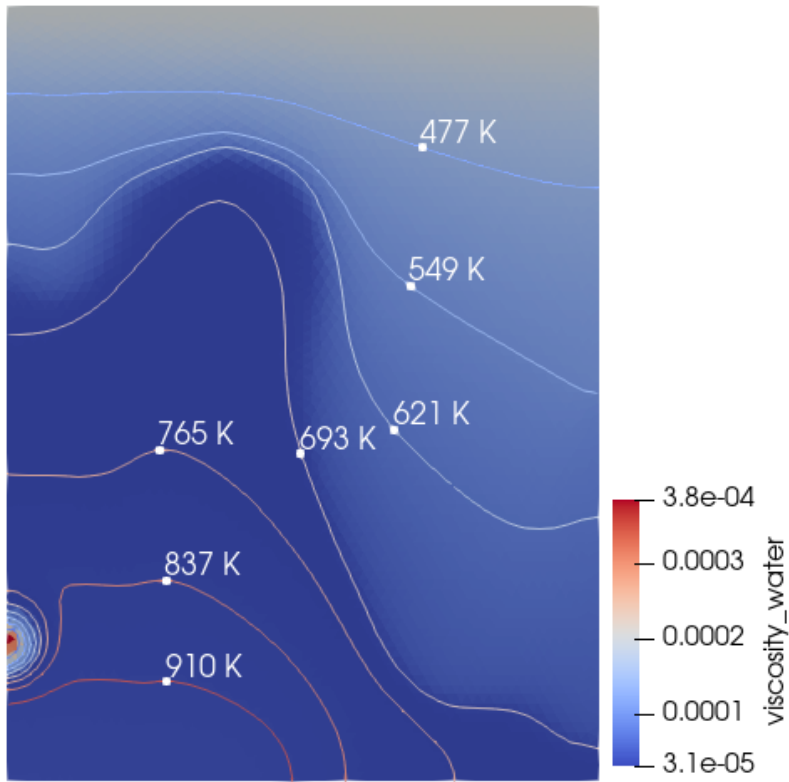


Figure 45 Viscosity profile [Pa·s] of injection on the left side at 10 mD after 30 years

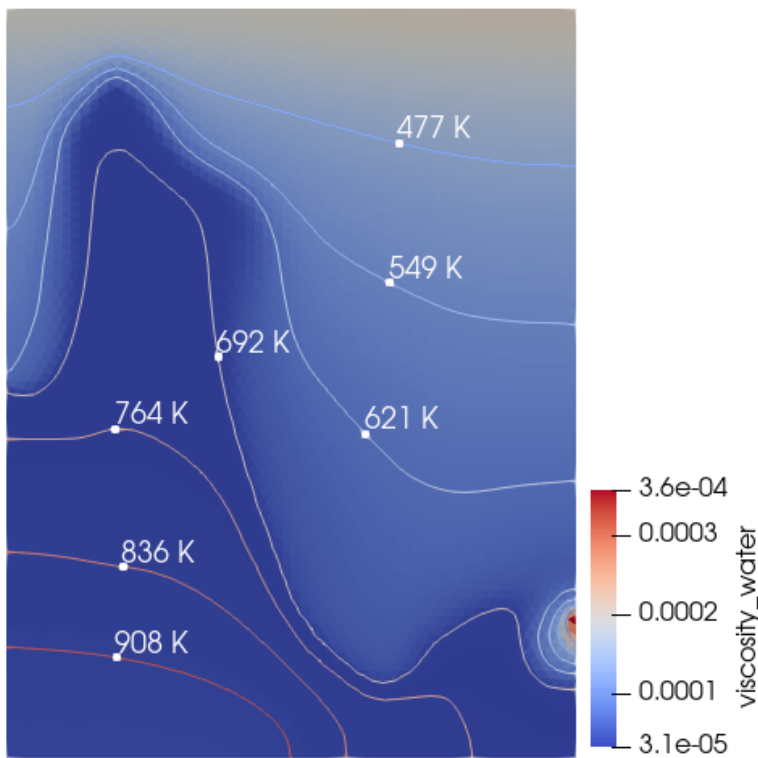


Figure 46 Viscosity profile [Pa·s] of injection on the right side at 10 mD after 30 years

The temperature and viscosity profiles presented in Figures 43 to 46 show a clear correlation between the temperature and viscosity. There is also a clear correlation in the witnessed low viscosity zones caused by the temperature and the pattern of CO₂ migration. The injected CO₂ follows the low viscosity pattern, caused by the temperature profile which resulted from the introduced flow from the injection and production. These observations offer a plausible explanation as to why CO₂ injected on the left side, or which has migrated to the left reservoir boundary, tends to float for high permeabilities, even though the density and gravity numbers should promote sinking behavior.

For a comparison of these witnessed effects, the case for the lowest examined permeability at 1 mD, with injection on the left side 200 m above the reservoir bottom will be reviewed.

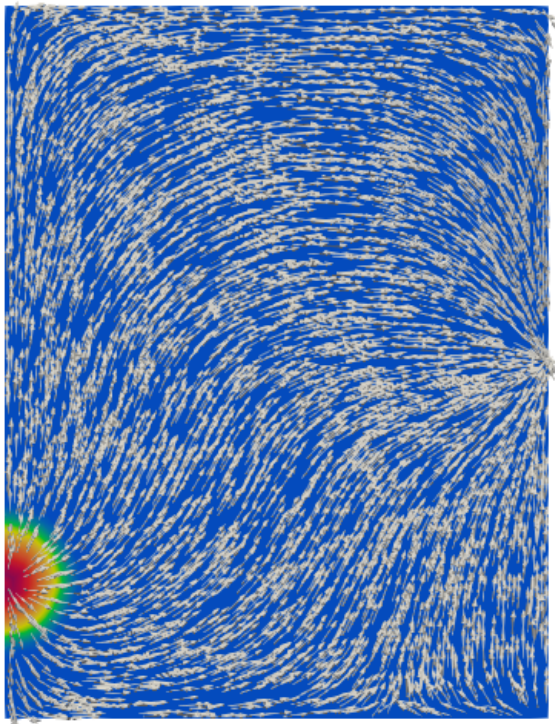


Figure 47 Bulk movement and CO₂ concentration in a 1 mD reservoir after 1 year of injection

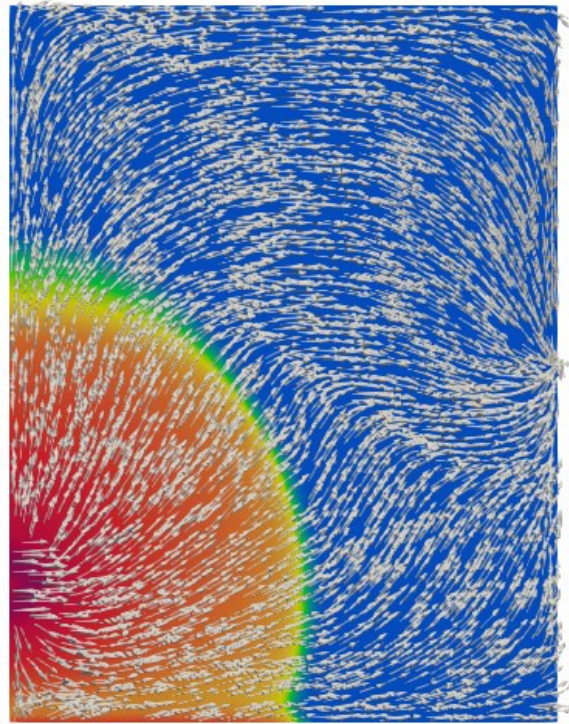


Figure 48 Bulk movement and CO₂ concentration in a 1 mD reservoir after 30 years of injection

Figures 47 and 48 show the CO₂ concentration and bulk movement for the 1 mD case after 1 year and after 30 years. Along with the shape of the CO₂ plume observed in the Results section, the bulk movement presents stark differences compared to the 10 mD cases. For one, there is no discernible upward movement emanating from the magma source visible and the movement goes from the injection to the production point, with no convection cells being formed. The bulk movement from the injection point is isotropic, leading to the observed bell shape of the plume.

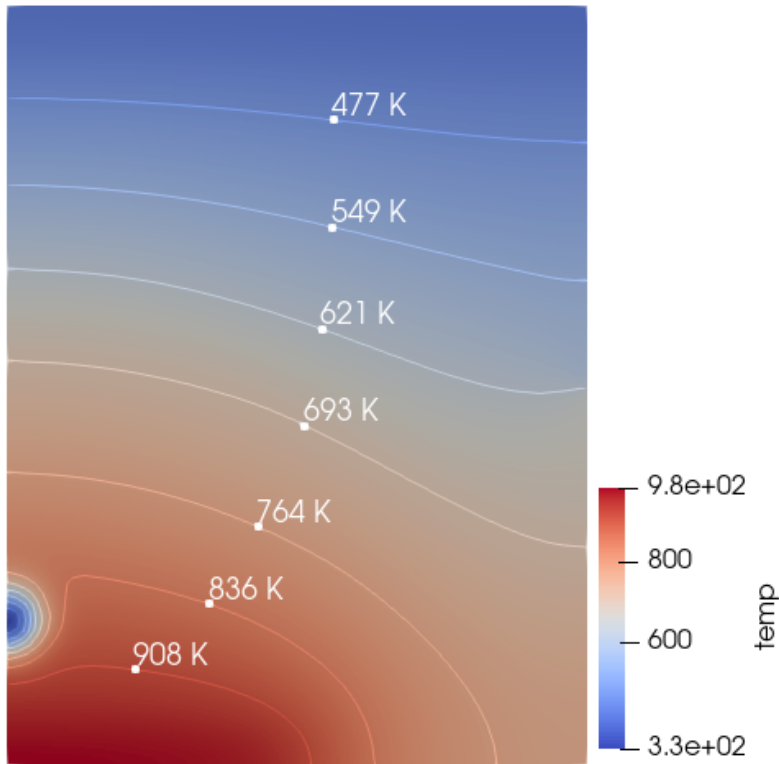


Figure 49 Temperature profile [K] of injection on the left side at 1 mD after 30 years

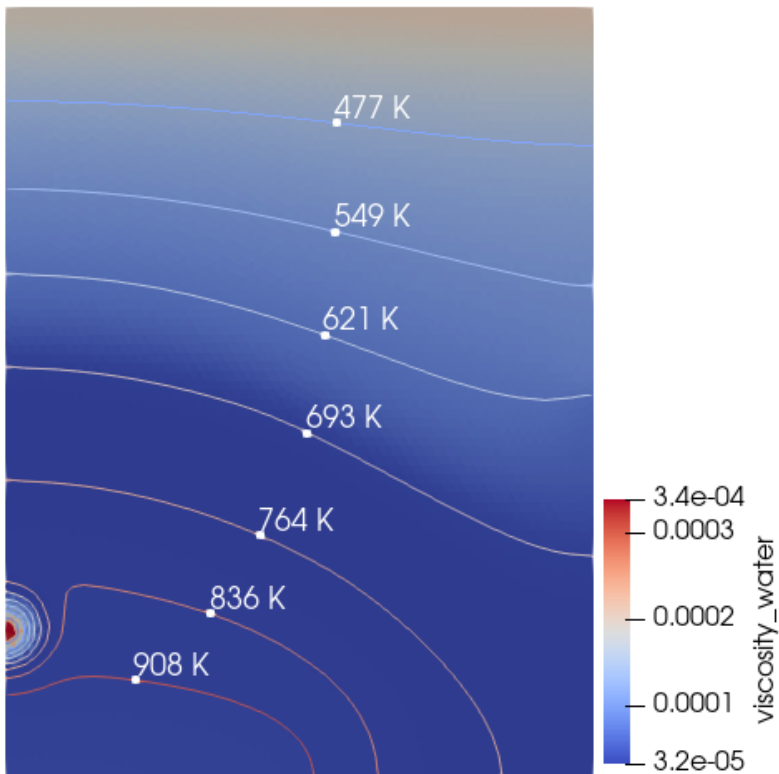


Figure 50 Viscosity profile [Pa·s] of injection on the left side at 1 mD after 30 years

The observed temperature profile in Figure 49 and the viscosity profile in Figure 50 are consistent with the observed CO₂ plume and bulk movement.

In the authors opinion, these demonstrations offer a plausible explanation as to why CO₂ injected on the left side at high permeabilities migrates towards the top of the reservoir, as well as the upward trend of CO₂ injected on the right side when reaching the left boundary in the high permeability cases.

The results confirm that the variation in permeability has arguably the biggest influence on the behavior of the injected CO₂.

One of the best results in terms of potentially safe storage has been observed in the case with 1 mD permeability and injection on the right side 200 m above the bottom reservoir boundary.

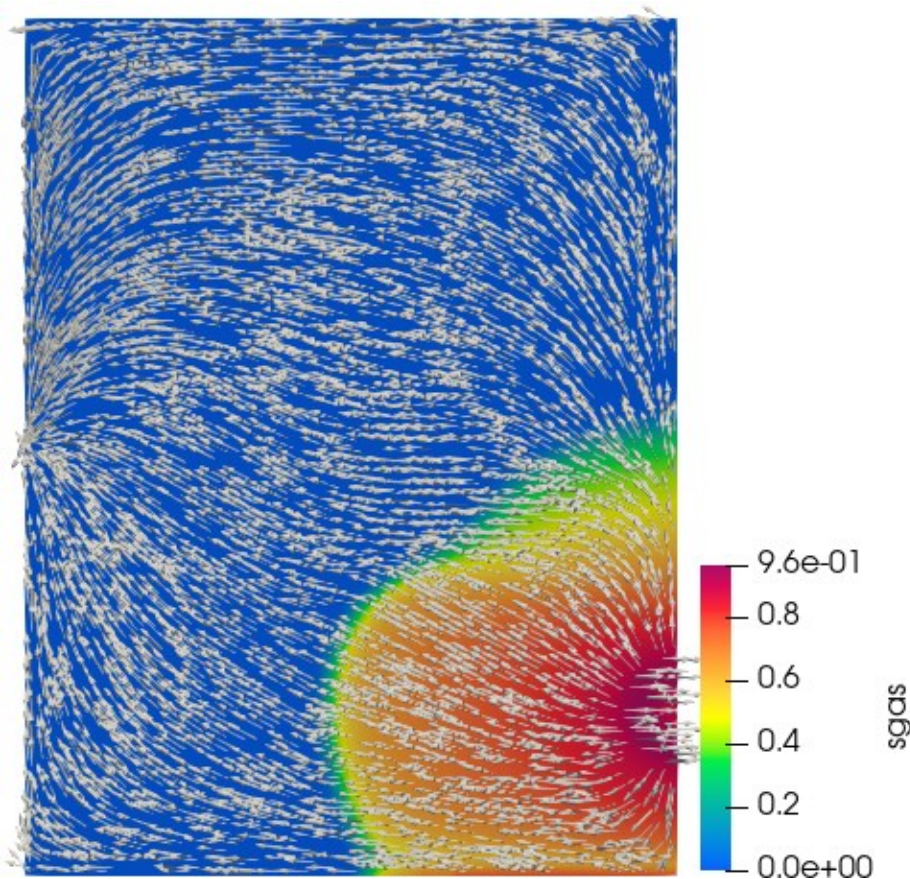


Figure 51 Injection 200 m above the bottom reservoir boundary at 1 mD after 30 years

Figure 51 details the bulk movement of fluid after 30 years of injection 200 m above the bottom reservoir boundary on the right side at 1 mD permeability. The calculated gravity numbers in Table 25, as well as the bulk movement and migration pattern of the CO₂ plume support more horizontal, viscous dominated behavior, exhibiting a slight sinking tendency. This slight sinking tendency is aided by the density profiles of water and CO₂, which exhibit a larger

density of CO₂ around the injection point, support by the values in Table 25 and Figures 52 and 53.

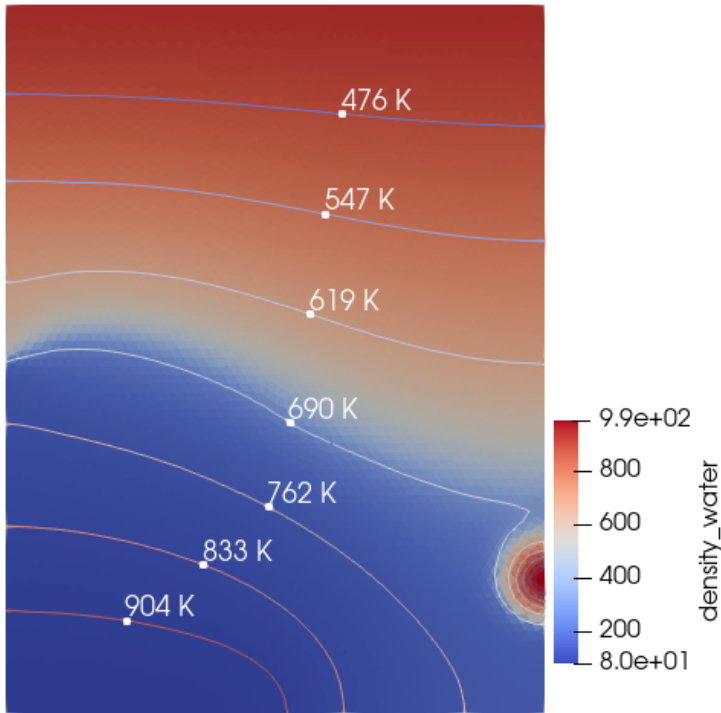


Figure 52 Density profile of water [kg/m³] after 30 years of injection at 1 mD 200 m above the bottom reservoir boundary on the right side

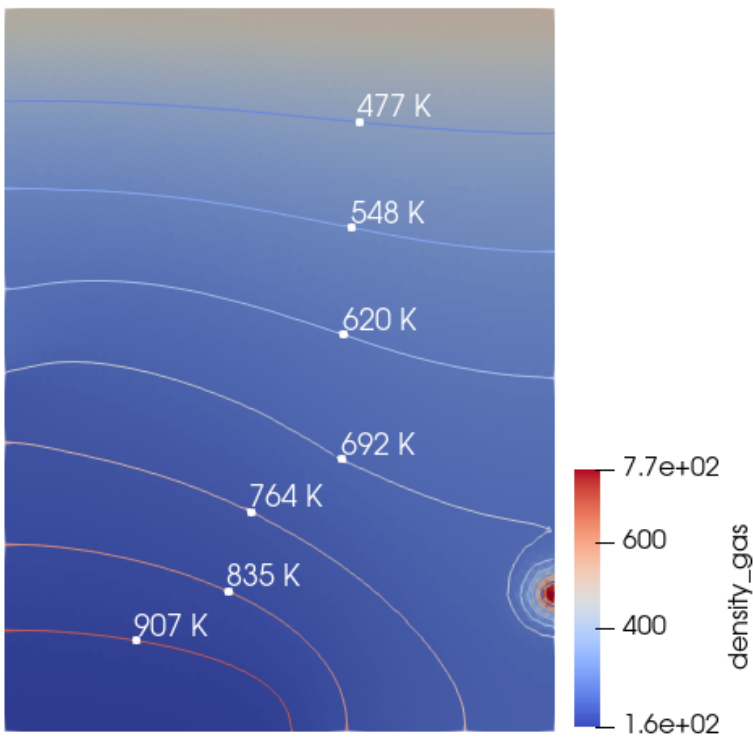


Figure 53 Density profile of CO₂ [kg/m³] after 30 years of injection at 1 mD 200 m above the bottom reservoir boundary on the right side

These findings underscore the strong influence of permeability and temperature distribution on CO₂ migration within reservoir configurations and suggest important considerations for CO₂ storage design and selection. The results also suggest that low permeabilities are favorable for the storage of CO₂ in reservoirs with temperature gradients, in contrast to the findings of Probst (2023) for constant temperature reservoirs, in which the high permeability cases performed the best.

The temperature distribution modifies the permeability effects, particularly in high-permeability cases. In configurations with temperature gradients, the injected CO₂ tends to migrate upwards along low-viscosity zones associated with the hotter regions, counter to the expected sinking behavior based purely on the density difference.

In a broader context, these results suggest that permeability and temperature variations within a reservoir will have a significant impact on CO₂ plume shape, migration, and long-term stability, indicating that CO₂ storage models should account for both factors to predict plume movement accurately. While low-permeability environments may ensure more controlled, lateral spread due to viscous forces, higher permeability with temperature gradients can introduce vertical, convective flows that may result in less predictable migration patterns. This understanding provides a critical foundation for designing CO₂ injection strategies that optimize storage security considering permeability and temperature interactions to minimize the risk of CO₂ leakage. The insights into the formation of convection cells and the bulk movement trends observed in higher-permeability cases further highlight the necessity of adapting injection strategies based on specific reservoir characteristics, supporting CO₂ sequestration methods that align with long-term storage and environmental safety objectives.

4.2 Pressure Profiles at the Injection Points

The observed pressure profiles across the examined injection depths and permeabilities considered in Chapter 3.9 can be explained by the fundamental relationship of fluid flow and rock permeability. In the low permeability cases, the fluid movement is restricted, causing higher pressures to build up more quickly. In contrast, at the higher permeabilities, the reservoir rock allows the injected CO₂ and resident water to disperse more freely. This results in a lower initial pressure and faster pressure decline (Birkholzer and Zhou, 2009). This knowledge helps to explain the lower initial pressure and faster decline observed in the 10 mD cases.

These pressure profiles, in particular the maximum pressure reached shortly after the start of the injection, have a significant impact on the reservoir integrity and CO₂ storage safety. The observed pressure increase in this case should not have any negative implications on the

integrity, as a study by McGrail et al. (2014) investigated supercritical CO₂ injection at the Wallula Basalt Pilot Project with well pressures 2.8 MPa above the initial condition and no CO₂ leakage was detected.

Overall, understanding the relationship between permeability and pressure is crucial for assessing CO₂ storage, as the lower permeability cases lead to higher pressure build-up, while providing favorable characteristics of the CO₂ plume.

Chapter 5

Conclusion

5.1 Summary

This work has investigated the behavior of CO₂ injection in different reservoir configurations, focusing on the influence of permeability and temperature distribution. The results confirm that permeability plays a dominant role in determining the migration pattern and shape of the CO₂ plume, with low-permeability reservoirs exhibiting primarily viscous-dominated horizontal migration and high-permeability reservoirs allowing gravity-dominated vertical migration. These results reinforce the relationship between the gravity number and migration behavior, showing a clear trend towards horizontal spreading at low permeabilities, while high permeabilities promote vertical movement strongly influenced by buoyancy.

Temperature gradients within the reservoir add further complexity to these permeability driven behaviors, as shown in high permeability scenarios, where temperature induced viscosity changes lead to unexpected upward migration. The results of the temperature and viscosity profiles show that CO₂ follows low-viscosity pathways created by the temperature gradients, often counteracting gravitational forces. This behavior highlights the importance of considering temperature distribution, particularly in reservoirs where thermal anomalies, such as those introduced by a magma source, can drive CO₂ movement away from its expected density-driven path.

These observations have important implications for the design of CO₂ storage facilities. They highlight that permeability and temperature distributions within a reservoir must be carefully considered to ensure safe and stable storage.

5.2 Future Work

Future work should explore these interactions further, examining a wider range of permeability and temperature scenarios, to deepen our understanding of CO₂ migration in complex subsurface environments and improve the predictability of long-term storage behavior. There are several parameters which may be modified in future research, such as the reservoir size, a model in 3D, different permeability ranges, including anisotropic permeabilities and different injection rates.

Additional studies should investigate the effects of more complex, heterogeneous reservoir configurations. Real-world reservoirs often contain zones of varying permeability and temperatures, which could lead to mixed migration behaviors within the same injection area. Modeling the impact of such heterogeneous zones could provide a more realistic basis for predicting CO₂ plume movement in naturally occurring reservoirs.

Given the observations of convection cell formation in high-permeability, temperature-distributed reservoirs, future work could also involve a more detailed study on convection patterns over longer time scales. Understanding how these convection cells evolve and interact with the CO₂ plume over longer time periods could be essential for predicting long-term storage stability. Additionally, examining the impact of varying injection rates and depths on convection patterns could yield valuable data on how to control or utilize these natural flows to enhance storage security.

Finally, experimental studies or field trials in controlled reservoir models could provide empirical validation of the model's predictions.

In summary, advancing our understanding of the interactions between permeability, temperature and CO₂ behavior through a larger variety of models will be crucial for developing safe CO₂ storages that are stable for extended periods and adaptable to changing geological factors.

References

- Al-Shafi, M.; Massarweh, O.; Abushaikha, A. S.; Bicer, Y. (2023): A review on underground gas storage systems: Natural gas, hydrogen and carbon sequestration. In *Energy Reports* 9, pp. 6251–6266. DOI: 10.1016/j.egy.2023.05.236.
- Birkholzer, J. T.; Zhou, Q. (2009): Basin-scale hydrogeologic impacts of CO₂ storage: Capacity and regulatory implications. In *International Journal of Greenhouse Gas Control* 3 (6), pp. 745–756. DOI: 10.1016/j.ijggc.2009.07.002.
- Blazek, J. (Ed.) (2005): *Computational Fluid Dynamics: Principles and Applications* (Second Edition). Oxford: Elsevier Science.
- Brenner, S. C.; Scott, L. R. (Eds.) (2008): *The Mathematical Theory of Finite Element Methods*. New York, NY: Springer New York.
- Chen, R.; Xu, W.; Chen, Y.; Hu, Y.; Li, J.; Zhuang, D.; Bate, B. (2023): Modeling pore-scale CO₂ plume migration with a hypergravity model. In *Geoenergy Science and Engineering* 231, Article 212294. DOI: 10.1016/j.geoen.2023.212294.
- Eichelberger, J. (2020): Distribution and Transport of Thermal Energy within Magma–Hydrothermal Systems. In *Geosciences* 10 (6). DOI: 10.3390/geosciences10060212.
- Fenghour, A.; Wakeham, W. A.; Vesovic, V. (1998): The Viscosity of Carbon Dioxide. In *Journal of Physical and Chemical Reference Data* 27 (1), pp. 31–44. DOI: 10.1063/1.556013.
- Fournier, R. O. (1999): Hydrothermal processes related to movement of fluid from plastic into brittle rock in the magmatic-epithermal environment. In *Economic Geology* 94 (8), pp. 1193–1211. DOI: 10.2113/gsecongeo.94.8.1193.
- Ghysels, P.; Synk, R. (2022): High performance sparse multifrontal solvers on modern GPUs. In *Parallel Computing* 110, Article 102897. DOI: 10.1016/j.parco.2022.102897.

- Giudicelli, G.; Lindsay, A.; Harbour, L.; Icenhour, C.; Li, M.; Hansel, J. E. et al. (2024): 3.0 - MOOSE: Enabling massively parallel multiphysics simulations. In *SoftwareX* 26, Article 101690. DOI: 10.1016/j.softx.2024.101690.
- Gogoleva, S. Y. (2018): Preconditioning Based on LU Factorization in Iterative Method for Solving Systems of Linear Algebraic Equations with Sparse Matrices. In *J. Phys.: Conf. Ser.* 1096, Article 012165. DOI: 10.1088/1742-6596/1096/1/012165.
- Gudmundur, O.; Friðleifsson, G.; Albertsson, A.; Stefansson, B.; Gunnlaugsson, E.; Adalsteinsson, H. (2007): Deep Unconventional Geothermal Resources: a major opportunity to harness new sources of sustainable energy. Available online at <https://api.semanticscholar.org/CorpusID:56215406>.
- Hillel, D. (Ed.) (2005): *Encyclopedia of Soils in the Environment*. Oxford: Elsevier.
- Hurwitz, S.; Christiansen, L. B.; Hsieh, P. A. (2007): Hydrothermal fluid flow and deformation in large calderas: Inferences from numerical simulations. In *J. Geophys. Res.* 112 (B2), Article 2006JB004689. DOI: 10.1029/2006JB004689.
- Ide, T. S.; Jessen, K.; Orr, F. M. (2007): Storage of CO₂ in saline aquifers: Effects of gravity, viscous, and capillary forces on amount and timing of trapping. In *International Journal of Greenhouse Gas Control* 1 (4), pp. 481–491. DOI: 10.1016/S1750-5836(07)00091-6.
- Karakas, O.; Degruyter, W.; Bachmann, O.; Dufek, J. (2017): Lifetime and size of shallow magma bodies controlled by crustal-scale magmatism. In *Nature Geosci* 10 (6), pp. 446–450. DOI: 10.1038/NGEO2959.
- Lanzi, C.; Drouin, V.; Sigmundsson, F.; Geirsson, H.; Hersir, G. P.; Ágústsson, K. et al. (2023): Pressure increase at the magma-hydrothermal interface at Krafla caldera, North-Iceland, 2018–2020: Magmatic processes or hydrothermal changes? In *Journal of Volcanology and Geothermal Research* 440, Article 107849. DOI: 10.1016/j.jvolgeores.2023.107849.
- Liu, X. Y.; He, M. G.; Zhang, Y. (2012): Viscosity of water in the region around the critical point. In *The Journal of Supercritical Fluids* 63, pp. 150–154. DOI: 10.1016/j.supflu.2011.11.021.
- McGrail, B. P.; Spane, F. A.; Amonette, J. E.; Thompson, C. R.; Brown, C. F. (2014): Injection and Monitoring at the Wallula Basalt Pilot Project. In *Energy Procedia* 63, pp. 2939–2948. DOI: 10.1016/j.egypro.2014.11.316.
- Miocic, J. M.; Gilfillan, S. M.; Roberts, J. J.; Edlmann, K.; McDermott, C. I.; Haszeldine, R. S. (2016): Controls on CO₂ storage security in natural reservoirs and implications for CO₂

- storage site selection. In *International Journal of Greenhouse Gas Control* 51, pp. 118–125. DOI: 10.1016/j.ijggc.2016.05.019.
- Montanari, D.; Bonini, M.; Corti, G.; Agostini, A.; Del Ventisette, C. (2017): Forced folding above shallow magma intrusions: Insights on supercritical fluid flow from analogue modelling. In *Journal of Volcanology and Geothermal Research* 345, pp. 67–80. DOI: 10.1016/j.jvolgeores.2017.07.022.
- Nath, A.; Patel, M.; Mohanta, B. (2024): A REVIEW Geo thermal energy -Clean, safe and renewable -A review study. In *INTERNATIONAL JOURNAL OF AGRICULTURAL SCIENCES* 20, pp. 306–309. DOI: 10.15740/HAS/IJAS/20.1/306-309.
- Parekh, A.; Chaturvedi, G.; Dutta, A. (2023): Sustainability analyses of CO₂ sequestration and CO₂ utilization as competing options for mitigating CO₂ emissions. In *Sustainable Energy Technologies and Assessments* 55. DOI: 10.1016/j.seta.2022.102942.
- Parisio, F.; Vilarrasa, V. (2020): Sinking CO₂ in Supercritical Reservoirs. In *Geophysical research letters* 47 (23), Article e2020GL090456. DOI: 10.1029/2020GL090456.
- Probst, F. S. (2023): CO₂ Flow in Supercritical Geothermal Systems. Master's Thesis. Montanuniversität Leoben.
- Pudyastuti, K.; Harmen, H.; Djumantara, M.; Fadhlurrahman, S. (Eds.) (2019): Thermal characteristics of the X geothermal resources, and a recommendation on utilization possibility. *Journal of Physics: Conference Series* (1402). Available online at <https://www.scopus.com/inward/record.uri?eid=2-s2.0-85078259872&doi=10.1088%2f1742-6596%2f1402%2f2%2f022057&partnerID=40&md5=bd80cee964fd39ebf22b32daa0dc732c>.
- Reinsch, T.; Dobson, P.; Asanuma, H.; Huenges, E.; Poletto, F.; Sanjuan, B. (2017): Utilizing supercritical geothermal systems: a review of past ventures and ongoing research activities. In *Geotherm Energy* 5 (1). DOI: 10.1186/s40517-017-0075-y.
- Rodrigo-Naharro, J.; Aracil, E.; Del Pérez Villar, L. (2018): Geophysical investigations in the Gañuelas-Mazarrón Tertiary basin (SE Spain): A natural analogue of a geological CO₂ storage affected by anthropogenic leakages. In *Journal of Applied Geophysics* 155, pp. 187–198. DOI: 10.1016/j.jappgeo.2018.06.006.
- Rubin, E. S.; Davison, J. E.; Herzog, H. J. (2015): The cost of CO₂ capture and storage. In *International Journal of Greenhouse Gas Control* 40, pp. 378–400. DOI: 10.1016/j.ijggc.2015.05.018.

- Samara, H.; Ostrowski, T. v.; Jaeger, P. (2024): Interfacial and transport properties of supercritical hydrogen and carbon dioxide in unconventional formations. In *The Journal of Supercritical Fluids* 205, Article 106124. DOI: 10.1016/j.supflu.2023.106124.
- Scalabrin, G.; Marchi, P.; Finezzo, F.; Span, R. (2006): A Reference Multiparameter Thermal Conductivity Equation for Carbon Dioxide with an Optimized Functional Form. In *Journal of Physical and Chemical Reference Data* 35 (4), pp. 1549–1575. DOI: 10.1063/1.2213631.
- Scott, S.; Driesner, T.; Weis, P. (2015): Geologic controls on supercritical geothermal resources above magmatic intrusions. In *Nature communications* 6, Article 7837. DOI: 10.1038/ncomms8837.
- Scott, S.; Driesner, T.; Weis, P. (2017): Boiling and condensation of saline geothermal fluids above magmatic intrusions. In *Geophysical research letters* 44 (4), pp. 1696–1705. DOI: 10.1002/2016GL071891.
- Statista Research Department: CO₂-Ausstoß weltweit. Available online at <https://de.statista.com/statistik/daten/studie/37187/umfrage/der-weltweite-co2-ausstoss-seit-1751/>, checked on 6/26/2024.
- Stefánsson, A.; Friðleifsson, G. Ó.; Sigurðsson, Ó.; Gíslason, Þ. (2021): The IDDP-2 DEEPEGS Drilling Experience and Lesson Learned.
- Tester, J. W.; Anderson, B. J.; Batchelor, A. S.; Blackwell, D. D.; DiPippo, R.; Drake, E. M. et al. (2006): The future of geothermal energy. Impact of enhanced geothermal systems (EGS) on the United States in the 21st century. Idaho Falls, Idaho: Idaho National Laboratory.
- Wagner, W.; Cooper, J. R.; Dittmann, A.; Kijima, J.; Kretzschmar, H.-J.; Kruse, A. et al. (2000): The IAPWS Industrial Formulation 1997 for the Thermodynamic Properties of Water and Steam. In *Journal of Engineering for Gas Turbines and Power* 122 (1), pp. 150–184. DOI: 10.1115/1.483186.
- Waples, D. W.; Waples, J. S. (2004): A Review and Evaluation of Specific Heat Capacities of Rocks, Minerals, and Subsurface Fluids. Part 1: Minerals and Nonporous Rocks. In *Natural Resources Research* 13 (2), pp. 97–122. DOI: 10.1023/B:NARR.0000032647.41046.e7.
- Weis, P. (2015): The dynamic interplay between saline fluid flow and rock permeability in magmatic-hydrothermal systems. In *Geofluids* 15 (1-2), pp. 350–371. DOI: 10.1111/gfl.12100.
- Yang, T.-H. J.; Chambefort, I.; Rowe, M.; Mazot, A.; Seward, A.; Werner, C. et al. (2024): Variability in surface CO₂ flux: Implication for monitoring surface emission from geothermal fields. In *Geothermics* 120, Article 102981. DOI: 10.1016/j.geothermics.2024.102981.

Yapparova, A.; Lamy-Chappuis, B.; Scott, S. W.; Gunnarsson, G.; Driesner, T. (2023): Cold water injection near the magmatic heat source can enhance production from high-enthalpy geothermal fields. In *Geothermics* 112, Article 102744. DOI: 10.1016/j.geothermics.2023.102744.

Zarrouk, S. J.; McLean, K. (2019): Chapter 2 - Geothermal systems. In Sadiq J. Zarrouk, Katie McLean (Eds.): *Geothermal Well Test Analysis*: Academic Press, pp. 13–38. Available online at <https://www.sciencedirect.com/science/article/pii/B9780128149461000025>.

Zarrouk, S. J.; McLean, K. (Eds.) (2019): *Geothermal Well Test Analysis*: Academic Press.

Appendix A

Simulation Files

The link below contains the input files used for the simulations analyzed in the thesis. The file “CO2_2A.i” is used for injection into temperature distributed reservoirs, “CO2_highT_const.i” was used for injection into the constant temperature reservoir. The equilibrium files “Equi2.i” and “Equi2_constT” simulate the distributed temperature conditions and constant conditions respectively.

To obtain all of the analyzed results, the user has to modify the mesh files, the coordinate files for the boreholes, the equilibrium files and the CO₂ files to the corresponding injection and production points, as well as the desired permeability.

GitHub link:

<https://github.com/UebelleitnerJan/Sinking-CO2-Uebelleitner.git>

List of Figures

Figure 1 A Fluid pressure and specific enthalpy graph with isotherms showing the different fluid phase areas encountered during the drilling of IDDP-1, highlighting the two phase, single phase and supercritical regions, Scott et al., 2015	14
Figure 2 Graph detailing the density difference of water and CO ₂ at pressures ranging from 20 MPa to 60 MPa and temperature ranging from 0°C to 800°C, Parisio and Vilarrasa, 2020	16
Figure 3 Architecture of the MOOSE framework illustrating the interaction between physics modules, the underlying libMesh library for finite element analysis and solver interfaces, Giudicelli et al., 2024	20
Figure 4 Specific heat of different rock types plotted against temperature ranging from 0°C to 1200°C, Waples and Waples, 2006.....	25
Figure 5 Illustration of the mesh used for further analysis, along with coordinates which will be referred to in analysis	27
Figure 6 This illustration details the behavior of the injected CO ₂ plume along with the gravity numbers, showing the viscous dominated behavior in the near wellbore region and the gravity numbers in the lower part of the plume which are greater than 1, indicating sinking behaviour due to the higher density of CO ₂ , Parisio and Vilarrasa, 2020.....	33
Figure 7 Example of the position of points for Ngv calculation for an injection depth of 400 m	34
Figure 8 Example of the position of points for Ngv calculation for an injection depth of 200 m	34
Figure 9 Position of Ngv calculation points at 200m on the right side.....	34
Figure 10 Position of Ngv calculation points at 400m on the right side.....	34
Figure 11 Pressure profile of the equilibrium file at a constant temperature of T =773.15 K	36
Figure 12 Temperature distribution of the equilibrium case with a 1000 K magma source	37
Figure 13 CO ₂ injection for 30 years at k= 10 mD and constant temperature at T=773.15 K.....	38
Figure 14 CO ₂ injection for 30 years at k= 5mD and constant temperature at T=773.15 K.....	39
Figure 15 CO ₂ injection for 30 years at k= 1mD and constant temperature at T=773.15 K.....	40
Figure 16 CO ₂ injection for 30 years at k= 10mD and 200 m above the reservoir boundary.....	42
Figure 17 CO ₂ injection for 30 years at k=10 mD and 400 m above the reservoir boundary	43
Figure 18 CO ₂ injection for 30 years at k= 10mD and 525 m above the reservoir boundary	44
Figure 19 CO ₂ injection for 30 years at k= 5mD and 200 m above the reservoir boundary.....	46
Figure 20 CO ₂ injection for 30 years at k=5 mD and 400 m above the reservoir boundary.....	47
Figure 21 CO ₂ injection for 30 years at k=5 mD and 525 m above the reservoir boundary	48
Figure 22 CO ₂ injection for 30 years at k=1 mD and 200 m above the reservoir boundary.....	50
Figure 23 CO ₂ injection for 30 years at k=1 mD and 400 m above the reservoir boundary	51
Figure 24 CO ₂ injection for 30 years at k=1 mD and 525 m above the reservoir boundary	52
Figure 25 CO ₂ injection on the right for 30 years at k=10 mD and 200 m above the reservoir boundary	54
Figure 26 CO ₂ injection on the right for 30 years at k=10 mD and 400 m above the reservoir boundary	56
Figure 27 CO ₂ injection on the right for 30 years at k=10 mD and 525 m above the reservoir boundary	57
Figure 28 CO ₂ injection on the right for 30 years at k=5 mD and 200 m above the reservoir boundary	58
Figure 29 CO ₂ injection on the right for 30 years at k=5 mD and 400 m above the reservoir boundary	59
Figure 30 CO ₂ injection on the right for 30 years at k=5 mD and 525 m above the reservoir boundary	60
Figure 31 CO ₂ injection on the right for 30 years at k=1 mD and 200 m above the reservoir boundary	62
Figure 32 CO ₂ injection on the right for 30 years at k=1 mD and 400 m above the reservoir boundary	63

Figure 33 CO ₂ injection on the right for 30 years at k=1 mD and 525 m above the reservoir boundary	64
Figure 34 Pressure profiles [MPa] over 30 years at injection points 200 m above the bottom reservoir boundary for 1 mD and 10 mD permeability	66
Figure 35 Pressure profiles [MPa] over 30 years at injection points 525 m above the bottom reservoir boundary for 1 mD and 10 mD permeability	67
Figure 36 Injection on the left at 10 mD after 1 year.....	70
Figure 37 Injection on the right at 10 mD after 1 year.....	70
Figure 38 Injection on the left at 10 mD after 15 years	71
Figure 39 Injection on the right at 10 mD after 15 years	71
Figure 40 Injection on the left at 10 mD after 30 years	72
Figure 41 Injection on the right at 10 mD after 30 years	72
Figure 42 Water viscosity profile [Pa·s] at time zero	73
Figure 43 Temperature profile [K] of injection on the left side at 10 mD after 30 years	74
Figure 44 Temperature profile [K] of injection on the right side at 10 mD after 30 years	74
Figure 45 Viscosity profile [Pa·s] of injection on the left side at 10 mD after 30 years.....	75
Figure 46 Viscosity profile [Pa·s] of injection on the right side at 10 mD after 30 years	75
Figure 47 Bulk movement and CO ₂ concentration in a 1 mD reservoir after 1 year of injection.....	76
Figure 48 Bulk movement and CO ₂ concentration in a 1 mD reservoir after 30 years of injection	76
Figure 49 Temperature profile [K] of injection on the left side at 1 mD after 30 years	77
Figure 50 Viscosity profile [Pa·s] of injection on the left side at 1 mD after 30 years.....	77
Figure 51 Injection 200 m above the bottom reservoir boundary at 1 mD after 30 years	78
Figure 52 Density profile of water [kg/m ³] after 30 years of injection at 1 mD 200 m above the bottom reservoir boundary on the right side	79
Figure 53 Density profile of CO ₂ [kg/m ³] after 30 years of injection at 1 mD 200 m above the bottom reservoir boundary on the right side	79

List of Tables

Table 1 Reservoir rock parameters selected for the simulations.....	26
Table 2 Boundary conditions for the equilibrium file with the active magma source	28
Table 3 Boundary conditions of the constant temperature case, in accordance to the simulations by Probst (2023).....	28
Table 4 Boundary conditions for the CO ₂ injection cases	28
Table 5 Cases for equilibrium.....	29
Table 6 Description of parameters for the 21 cases of CO ₂ injection.....	30
Table 7 Density of water and CO ₂ [kg/m ³], CO ₂ viscosity [Pa·s] and gravity number for case above	38
Table 8 Density of water and CO ₂ [kg/m ³], CO ₂ viscosity [Pa·s] and gravity number for case above	39
<i>Table 9 Density of water and CO₂ [kg/m³], CO₂ viscosity [Pa·s] and gravity number for case above</i>	<i>40</i>
<i>Table 10 Density of water and CO₂ [kg/m³], CO₂ viscosity [Pa·s] and gravity number for case above</i>	<i>42</i>
Table 11 Density of water and CO ₂ [kg/m ³], CO ₂ viscosity [Pa·s] and gravity number for case above	43
Table 12 Density of water and CO ₂ [kg/m ³], CO ₂ viscosity [Pa·s] and gravity number for case above	44
Table 13 Density of water and CO ₂ [kg/m ³], CO ₂ viscosity [Pa·s] and gravity number for case above	46
Table 14 Density of water and CO ₂ [kg/m ³], CO ₂ viscosity [Pa·s] and gravity number for case above	47
Table 15 Density of water and CO ₂ [kg/m ³], CO ₂ viscosity [Pa·s] and gravity number for case above	48
Table 16 Density of water and CO ₂ [kg/m ³], CO ₂ viscosity [Pa·s] and gravity number for case above	50
Table 17 Density of water and CO ₂ [kg/m ³], CO ₂ viscosity [Pa·s] and gravity number for case above	51
Table 18 Density of water and CO ₂ [kg/m ³], CO ₂ viscosity [Pa·s] and gravity number for case above	52
Table 19 Density of water and CO ₂ [kg/m ³], CO ₂ viscosity [Pa·s] and gravity number for case above	54
Table 20 Density of water and CO ₂ [kg/m ³], CO ₂ viscosity [Pa·s] and gravity number for case above	56
Table 21 Density of water and CO ₂ [kg/m ³], CO ₂ viscosity [Pa·s] and gravity number for case above	57
Table 22 Density of water and CO ₂ [kg/m ³], CO ₂ viscosity [Pa·s] and gravity number for case above	58
Table 23 Density of water and CO ₂ [kg/m ³], CO ₂ viscosity [Pa·s] and gravity number for case above	59
Table 24 Density of water and CO ₂ [kg/m ³], CO ₂ viscosity [Pa·s] and gravity number for case above	60
Table 25 Density of water and CO ₂ [kg/m ³], CO ₂ viscosity [Pa·s] and gravity number for case above	62
Table 26 Density of water and CO ₂ [kg/m ³], CO ₂ viscosity [Pa·s] and gravity number for case above	63
Table 27 Density of water and CO ₂ [kg/m ³], CO ₂ viscosity [Pa·s] and gravity number for case above	64

Abbreviations

ASM	additive Schwarz method
CCS	Carbon Capture and Storage
CCU	Carbon Capture and Utilization
CCUS	Carbon Capture, Utilization and Storage
CO ₂	Carbon Dioxide
EGS	Enhanced Geothermal System
FE	Finite Element
GPa	gigapascal
GPU	graphics processing unit
Gt	Giga Ton
IAPWS	International Association for the Properties of Water and Steam
IDDP	Icelandic Deep Drilling Project
kg	kilogram
kJ	kilojoules
km	kilometer
m	meters
mD	millidarcy
MJ	megajoule
MOOSE	Multiphysics Object Oriented Simulation Environment
MPa	megapascal
MUMPS	MUltifrontal Massively Parallel Sparse direct Solver
MW	megawatts
Pa·s	pascal seconds
PDE	Partial Differential Equation
PETCs	Portable, Extensible Toolkit for Scientific Computation